

TECHNISCHE UNIVERSITÄT MÜNCHEN

Lehrstuhl für Neuronale Kontrolle des Metabolismus

The Role of the Endosomal System on Glucose Metabolism and Diabetes

Susanne Seitz

Vollständiger Abdruck der von der Fakultät Wissenschaftszentrum Weihenstephan für Ernährung, Landnutzung und Umwelt der Technischen Universität München zur Erlangung des akademischen Grades eines

Doktors der Naturwissenschaften

genehmigten Dissertation.

Vorsitzender:	Prof. Dr. Johann J. Hauner
Prüfer der Dissertation:	1. Prof. Dr. Ilona Grunwald Kadow
	2. Prof. Dr. Stephan Herzig
	3. Prof. Dr. Matthias Blüher

Die Dissertation wurde am 29.05.2019 bei der Technischen Universität München eingereicht und durch die Fakultät Wissenschaftszentrum Weihenstephan für Ernährung, Landnutzung und Umwelt am 25.09.2019 angenommen.

Table of contents

I. Summary.....	1
II. Zusammenfassung.....	2
1. Introduction.....	3
1.1. Type-2-Diabetes.....	3
1.2. Liver morphology and function.....	5
1.3. Blood glucose regulation.....	7
1.4. Mitochondrial dynamics.....	9
1.5. Autophagy.....	11
1.6. The Rab family.....	13
1.7. Endocytosis.....	15
1.8. The trafficking system in metabolic diseases.....	16
1.9. Screen for new trafficking candidates with a role in metabolism.....	17
1.10. Candidates.....	17
1.11. Objective.....	19
2. Results.....	21
2.1. <i>SGIP1</i> expression is upregulated in human patients with NASH.....	21
2.2. <i>CHMP4C</i> expression is upregulated in human NASH patients and regulates G6PASE expression <i>in vitro</i>	21
2.3. <i>Rab3ip</i> is differentially expressed in <i>db/db</i> and HFD mice.....	23
2.4. <i>RAB24</i> expression is highly increased in patients with fatty liver disease.....	25
2.5. RAB24 KD improves glucose clearance and serum lipids.....	27
2.6. RAB24 KD causes an increase in mitochondrial proteins.....	34
2.7. Reduction of RAB24 leads to an increase in mitochondrial mass and activity.....	36
2.8. RAB24 KD leads to increased glycolysis.....	38

2.9.	RAB24 KD causes an increase in autophagic flux and a reduction in mitophagy.....	40
2.10.	RAB24 KD causes an increase in mitochondrial connectivity by reducing mitochondrial fission	46
2.11.	Reduction of RAB24 ameliorate the metabolic phenotype caused by HFD	56
2.12.	KD of RAB24 in a NASH mouse model improves liver steatosis and inflammation	61
3.	Discussion	64
3.1.	The elevated <i>SGIP1</i> expression might originate from a different cell type other than hepatocytes	64
3.2.	Diverging effects of <i>in vitro</i> and <i>in vivo</i> experiments in CHMP4C KD.....	65
3.3.	Inconsistency of blood glucose levels upon the <i>in vivo</i> KD of RAB3IP.....	66
3.4.	From mitochondria to whole body glucose homeostasis.....	66
3.5.	The role of RAB24 in NASH	67
3.6.	RAB24 in hepatocellular carcinoma.....	68
3.7.	Regulation of endocytosis and metabolism is reciprocal.....	69
3.8.	Future perspectives.....	70
4.	Material and Methods	72
4.1.	Material	72
4.2.	Methods	81
5.	Appendix.....	99
6.	References	101
III.	Tables and Figures	117
IV.	Abbreviations.....	119
V.	Acknowledgements	123

I. Summary

Obesity is on the rise worldwide and with it metabolic diseases like type-2-diabetes (T2DM) and non-alcoholic fatty liver disease (NAFLD). So far, no treatments are available, due to the unclear mechanistic basis of NAFLD. This is also paving the way to more severe damage of the liver that can lead to cirrhosis and hepatocellular carcinoma. Novel evidence has put the cellular trafficking system in connection with metabolism. This thesis further shows the importance of the endosomal system in the regulation of metabolism by investigating the function of several components of endocytosis.

This thesis presents a novel function for an intracellular trafficking regulator RAB24, a small GTPase, in mitochondrial plasticity and turnover with impact on systemic and hepatic glucose and lipid homeostasis. Strikingly, the expression of *RAB24* was highly upregulated in the liver of obese patients and patients with NAFLD and was also positively correlated with increased body fat. The liver specific knock-down of RAB24 led to an increase in mitochondrial mass and function *in vitro*, in primary mouse hepatocytes, and to an improvement in serum cholesterol levels, as well as glucose clearance *in vivo*. Finally, the inhibition of RAB24 led to improvements of glucose and lipid parameters in mice on a HFD and a diet causing NAFLD (MCD diet) suggesting trafficking regulators, like RAB24, as therapeutic targets for metabolic diseases and highlighting the connection of intracellular transport and systemic metabolic regulation.

II. Zusammenfassung

Die Prävalenzrate für Übergewicht und damit verbundene Stoffwechselerkrankungen wie Typ-2-Diabetes (T2DM) und nicht-alkoholischen Fettlebererkrankung (NAFLD) steigt weltweit. Bisher sind durch die unbekannt zugrundeliegenden Mechanismen keine Behandlungsmöglichkeiten für NAFLD verfügbar, was langfristig zu schweren Leberschäden wie Zirrhose und Leberkrebs führen kann. Neue Studien zeigen eine bisher unbekannt Rolle für Moleküle des zellulären Transportsystems in der Regulation von Stoffwechselfvorgängen. Diese Arbeit zeigt die Bedeutung des endosomal Systems in der Stoffwechselregulation durch die funktionale Untersuchung verschiedener Komponenten der Endozytose.

In diesem Zusammenhang haben wir eine unerwartete Funktion für RAB24, eine kleine Rab GTPase, in der Aktivierung von Mitochondrien und Mitophagy-basierten Umsatz entdeckt, mit direktem Einfluss auf leber- und ganz-körper bezogenen Zucker und Fettstoffwechsel in NAFLD. Interessanterweise fanden wir erhöhte *RAB24* Expression in den Lebern von Übergewichtigen und NAFLD Patienten und eine positive Korrelation mit erhöhtem Körperfett in denselben Patienten. Die über Nanopartikel vermittelte, leberspezifische Inhibition von RAB24 führte zu einem Anstieg der mitochondrialen Masse und Funktion in primären Maushepatozyten *in vitro* und verbesserte Glukosetoleranz und verminderte Cholesterinlevels *in vivo*. Die Inhibition von RAB24 führte in Mäusen, die mit einer fettreichen Diät behandelt wurden, zu einer Verbesserung von Serumfetten und Zuckerstoffwechsel durch die Kontrolle von mitochondrialem Umsatz. Diese Ergebnisse heben den potentiellen therapeutischen Ansatz für Komponenten des endozytotischen Signalwegs hervor, wie beispielsweise RAB24, zur Behandlung von NAFLD vor und etablieren ein funktionales Konzept zwischen intrazellulärem Transport und systemischer Stoffwechselfdysfunktion.

1. Introduction

1.1. Type-2-Diabetes

The occurrence of type-2 diabetes (T2DM) has been increasing over the past decades and has reached an epidemic stage, however, effective treatments are still lacking. Commonly used medications for T2DM, like Metformin, often come with severe side effects such as stomach pain and nausea¹. The prevalence of diabetes has risen from 4.7% in 1980 to 8.5% in 2017 when it was affecting 425 million people and is estimated to reach 629 million people by 2045 (**Fig. 1**)^{2,3}. Risk factors include genetic dispositions, lifestyle, age and ethnicity⁴. T2DM is often accompanied by complications like kidney failure, blindness, limb amputations and heart attacks². Additionally T2DM is a major risk factor for developing cardiovascular diseases which are the leading cause of death worldwide⁵.

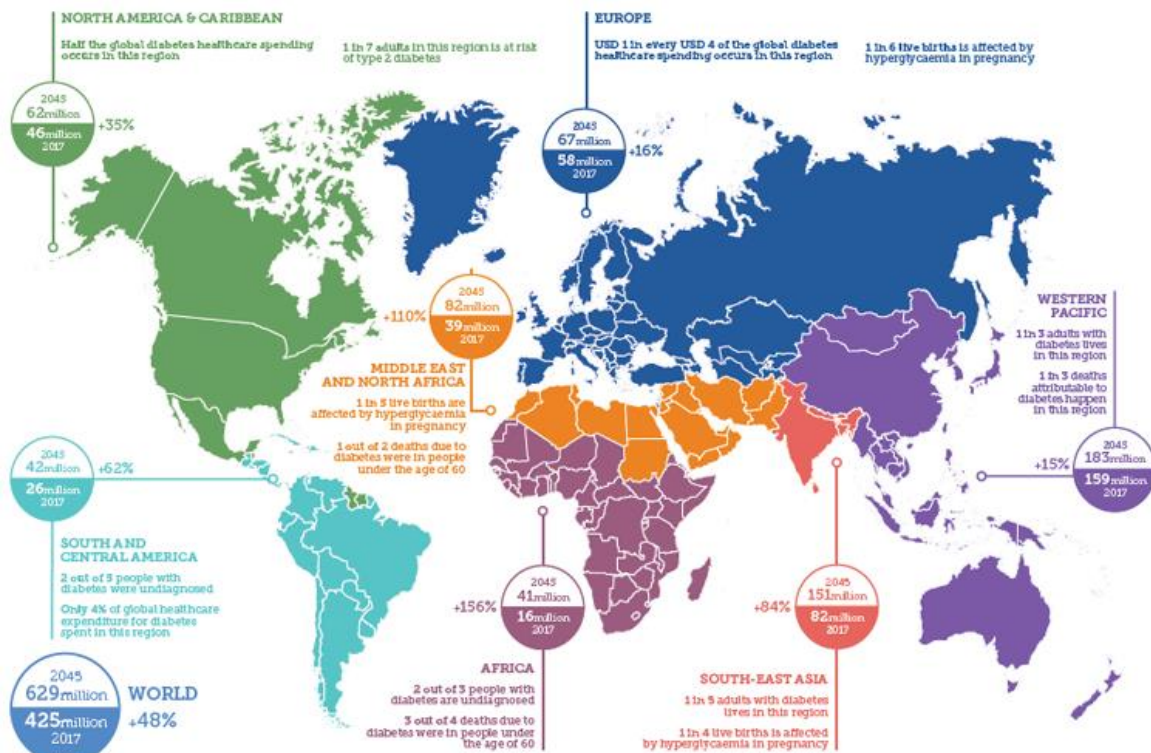


Figure 1: Global prevalence of diabetes.

Worldwide distribution of diabetes, showing for each continent the total number (in millions of people) of adults suffering from T2DM in 2017 and the predicted numbers for 2045. Adapted from³

T2DM is characterized by hyperglycemia and impaired glucose and protein metabolism. Hyperglycemia is caused by reduced insulin secretion due to dysfunctional β -cells or insulin resistance in insulin target organs like adipose tissue, muscle or liver. Insulin resistance is manifested by the inefficient execution of insulin induced signal transduction in the cell, causing an elevated glucose production in the liver and decreased glucose uptake into tissues, leading to hyperglycemia and impaired lipid metabolism^{6,7}. Hepatic glucose production is one of the main physiological processes that is altered in the course of the disease⁸ and hepatic insulin resistance was shown to be the primary event in the development of whole-body insulin resistance⁹, highlighting the important role of the liver regarding the various organs participating in the progression of T2DM.

Moreover, the prevalence of non-alcoholic fatty liver disease (NAFLD) is 59.67% in T2DM patients¹⁰ and another study could even show a prevalence of 74%¹¹. NAFLD is characterized by the accumulation of triglycerides within hepatocytes with minor or no inflammation. The relation of T2DM and NAFLD occurs through the joint delivery of insulin and glucagon through the portal vein to the liver where a large amount of the glucose is absorbed at the first pass. Obesity in NAFLD patients correlates with malfunction of the adipose tissue, leading to lipotoxicity that in turn further increases insulin resistance and β -cell dysfunction⁷. The disease can progress to the so-called non-alcoholic steatohepatitis (NASH) where inflammation increases and fibrosis (scarring of liver tissue) can occur¹². Patients with NAFLD and NASH are at an increased risk of developing liver cirrhosis and eventually liver cancer (HCC)¹³ (**Fig. 2**). These data draw attention to the importance of the liver in metabolic diseases and to its potential role in targeting those.

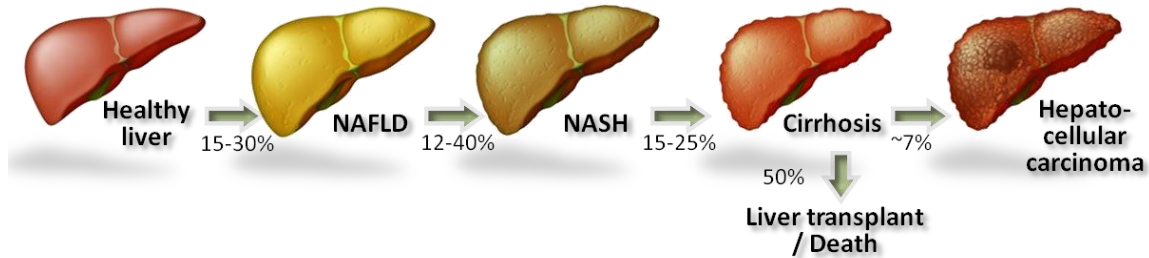


Figure 2: Progression of liver disease.

Healthy liver on the left, followed by NAFLD and NASH, progressing to liver cirrhosis and hepatocellular carcinoma. Adapted from¹⁴.

1.2. Liver morphology and function

The liver is an essential organ that is required for many different processes such as: protein synthesis, drug metabolism, detoxification, bile acid production, as well as glucose and lipid metabolism. Some key proteins that are secreted by the liver are albumin, a carrier protein for hormones, vitamins and enzymes; transferrin, that is responsible for iron binding and transport; C-reactive protein, an acute phase reactant, that is increased in response to inflammation and various coagulation factors. Bile acids are crucial for the digestion and adsorption of dietary fats and fat-soluble vitamins, removal of cholesterol and xenobiotics (exogenous biological substances) from the body as well as aiding in the regulation of bacteria in the small intestine and biliary tract¹⁵. For executing its crucial functions the liver has developed an elaborate morphology.

The liver is connected to two large blood vessels: the hepatic artery and the portal vein. The liver consists of four lobes that are made up of hepatic lobules that in turn consist of hepatocytes radiating from a vein and are organized in a structure called portal triad. A portal triad consists of a branch of each the hepatic artery, the hepatic portal vein, the vagus nerve and the bile duct as well as lymphatic vessels. Liver sinusoids are located between the hepatocytes and transport blood from the hepatic portal vein and hepatic artery to the central vein (**Fig. 3**)¹⁶.

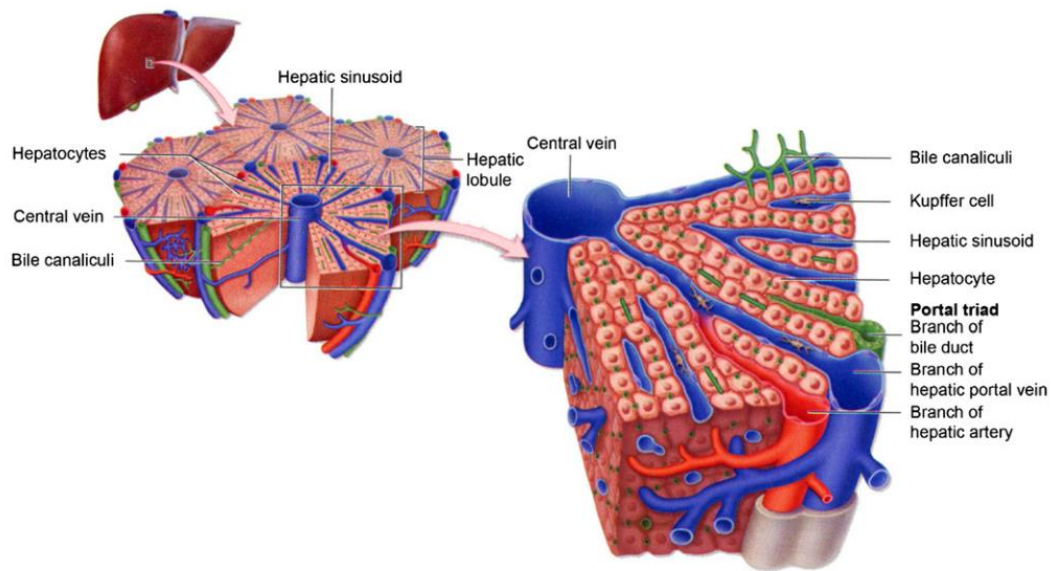


Figure 3: Liver morphology.

Outline of the liver at the organ level (left), microstructure of a liver lobule (middle) and a detailed structure of a functional division, portal triad (right). Adapted from¹⁷.

There are two major cell types in the liver: parenchymal and non-parenchymal cells. Although non-parenchymal cells constitute 40% of the total cell number in the liver, they only account for about 7% of the volume. Non-parenchymal cells are the star shaped Kupffer cells, which are specialized macrophages and therefore part of the immune system; stellate cells, responsible for vitamin A storage and fibrosis during liver damage; and sinusoidal endothelial cells that have extended pores, which allow nutrient flow from the vessels. About 80% of the liver volume is occupied by hepatocytes, thus constituting the major cell type¹⁸. Hepatocytes are highly polarized cells that have a basal and an apical surface. The basal surface is in contact with the blood system and provides the cell with nutrients, signaling molecules and metabolites. The apical side on the other hand is connected to the bile canaliculus network, where the hepatocytes secrete their metabolized products.

One of the major metabolites processed by hepatocytes is cholesterol. Cholesterol is an essential structural component of cell membranes and is important for the synthesis of bile acids, steroid hormones and vitamin D. As it is only slightly soluble in water, it is transported in lipoproteins. Lipoproteins are characterized by their protein/lipid ratio, which constitutes their density. The most widely known are high-density lipoprotein (HDL) and low-density lipoprotein (LDL). HDLs transport endogenous cholesterol from tissues to liver while in return LDLs transport endogenous fats and cholesterol from liver to tissues. Low levels of HDL have been associated with increased risk of T2DM¹⁹. In contrast, patients with T2DM usually display normal levels of LDL, but the plasma residence time of LDL is increased due to decrease of catabolism, which likely promotes cholesterol deposition in arteries that increases the risk of cardiovascular diseases²⁰. In addition to cholesterol levels, dysregulated glucose pathways play a major role in the progression of T2DM.

1.3. Blood glucose regulation

In a healthy organism blood glucose levels are regulated by the hormones insulin and glucagon that act contrary to each other. During prolonged fasting glucose levels fall, which leads to a drop in insulin levels. Concomitantly, glucagon is released by α -cells and binds to the glucagon receptor²¹. This leads to the activation of adenylate cyclase, subsequent increase of cyclic adenosine monophosphate (cAMP) levels and the activation of protein kinase A (PKA), resulting in the inhibition of glycolysis and the activation of gluconeogenesis²². During gluconeogenesis, substrates such as free fatty acids, glycerol and amino acids are utilized to produce glucose that is then released by the liver. Glucose-6-phosphatase (G6PASE) and Phosphoenolpyruvate carboxykinase (PCK1) are two of the rate limiting enzymes controlling this process²³. In a healthy liver, insulin inhibits glycogenolysis and gluconeogenesis, whereas this inhibition is lost during hepatic insulin resistance that leads to increased hepatic glucose output and therefore a worsening of hyperglycemia²⁴.

Postprandially, glucose levels rise and glucose transporters (GLUT1 in humans and GLUT2 in rodents)²⁵ allow the entry of glucose into the β -cells of the pancreas. Via glycolysis, glucose is turned into pyruvate that in turn enters the mitochondria. There, it gets processed in the tricarboxylic acid cycle (TCA) that switches on oxidative phosphorylation within the lumen of mitochondria, which results in the generation of ATP²⁶. The ATP/ADP ratio increases in the cytosol, causing ATP sensitive potassium channels to close^{27,28}, which leads to a depolarization of the cell membrane²⁹ and an action potential that causes voltage-gated calcium channels to open. Insulin vesicles adhere to the membrane and secrete insulin. The secreted insulin mainly acts on fat, liver and muscle tissue where it initiates the uptake, usage and storage of glucose.

In muscle and adipose tissue, insulin stimulates glucose uptake³⁰. These tissues contain glucose transporters type 4 (GLUT4), that are inserted in the membrane upon insulin binding to insulin receptor (INSR)³¹, through large stimulation of GLUT4 exocytosis and small inhibition of endocytosis. In the liver, after binding to INSR and initiating the phosphatidylinositol 3-kinase (PI3K)–AKT pathway³², AKT gets phosphorylated and in turn phosphorylates forkhead box O1 (FOXO1). The latter is then excluded from the nucleus where it usually, together with transcriptional coactivator peroxisome proliferator-activated receptor γ coactivator-1 α (PGC-1 α), acts as promoter of *G6Pase* and *Pck1* to stimulate gluconeogenesis^{33,34,35}. In addition to the inhibition of gluconeogenesis, insulin promotes glycogen synthesis through de-phosphorylation of glycogen synthase kinase 3 (GSK3) and thereby the activation of glycogen synthase³⁶. In the state of insulin resistance, the activation of this pathway is distorted, leading to excess glucose secretion while the uptake of glucose is inhibited, thus further increasing the severity of the disease.

Glucose can either be stored in hepatocytes or it enters the glycolytic pathways and is converted into pyruvate. Subsequently, pyruvate is either metabolized to lactate under anaerobic conditions (glycolysis) or enters the TCA cycle in mitochondria to produce energy precursors for oxidative phosphorylation where ADP is converted to ATP, the usable form of energy for the cell. Throughout the TCA cycle, carbon atoms are added and removed and energy can be captured as several of these steps are energet-

ically favorable. This energy is captured by reducing nicotinamide adenine dinucleotide NAD^+ to NADH and flavin adenine dinucleotide FAD to FADH_2 . During oxidative phosphorylation NADH and FADH_2 are oxidized stepwise in the so-called *electron transport chain* where each electron donor passes electrons to a more electronegative acceptor. This passage of electrons is used to pump protons into the intermembrane space of mitochondria and so generating a proton gradient. The protons flow back, following the gradient through an enzyme called ATP synthase, which uses the energy to transform ADP to ATP. As a great part of ATP production takes place inside mitochondria, a functional network of mitochondria is a crucial factor for energy homeostasis.

1.4. Mitochondrial dynamics

Mitochondria are highly regulated and dynamic organelles. To ensure quality and to respond to metabolic cues, mitochondrial mass is adjusted accordingly. In response to greater energy expenditure, cells increase their mitochondrial mass by initiating mitochondrial biogenesis, that is controlled by $\text{PGC1}\alpha$, $\text{PGC1}\beta$, Nuclear respiratory factor 1 (NRF1) and NRF2 ^{37,38}. Upon sensing an energy deficiency, AMP-activated kinase (AMPK) activates $\text{PGC1}\alpha$ via phosphorylation³⁹. Interestingly, the degradation of mitochondria, called mitophagy, is induced postprandially and is inhibited during fasting^{40,41}. This ensures that the energy, that is provided from autophagic substrates, is used properly during nutrient starvation⁴². Damaged mitochondria are segregated and later degraded. Upon mitochondrial depolarization, PTEN-induced kinase 1 (PINK1) becomes stabilized on the outer mitochondrial membrane⁴³. PINK1 recruits PARKIN to mitochondria and promotes its ligase activity by phosphorylation and therefore enables PARKIN to ubiquitinate mitochondrial proteins⁴⁴. This allows the assembly of ubiquitin-binding autophagy receptors that recruit the ATG8-positive phagophore, which engulfs the damaged mitochondria, initiating the fusion with lysosomes⁴⁵.

Not only mitochondrial mass is changed in different metabolic stages, also the connectivity of the mitochondrial network is adjusted via mitochondrial fusion and fission. Mitochondrial fusion is regulated by Optic Atrophy 1 (OPA1), MFN1 and MFN2 .

MFN1 and MFN2 are responsible for the fusion of the outer membranes while OPA1 is needed for the fusion of the inner membranes⁴⁶. Mitochondrial fission is mediated by dynamin-related protein 1 (DRP1) that controls the final fission step. DRP1 has been shown to interact with several proteins: mitochondria fission factor (MFF) binds DRP1 to promote fission⁴⁷, Fission 1 protein (FIS1) might be responsible for the recruitment of DRP1 to mitochondria, mitochondrial dynamics protein of 49 kDa (MID49) and MID51 are able to recruit DRP1 in the absence of FIS1⁴⁸. In the stage of metabolic oversupply, the mitochondrial network is more fragmented, which decreases overall mitochondrial activity in the cell and promotes nutrient storage. If the cell is nutrient deficient, the mitochondrial network is more connected, which leads to overall increase of mitochondrial activity in the cell to maintain the energy levels (**Fig. 4**)⁴⁹.

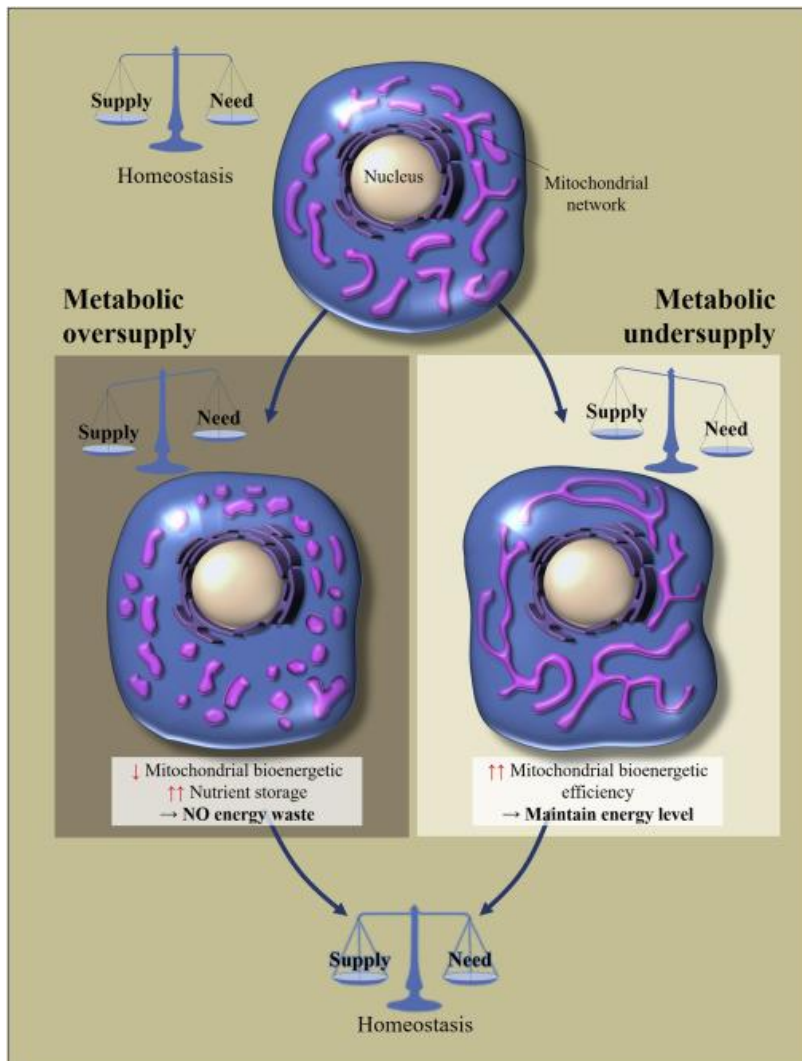


Figure 4: Mitochondrial network in metabolic over- and undersupply. Mitochondria are more fragmented in the state of metabolic oversupply and appear more connected in metabolic undersupply. Adapted from⁴⁹

Mitochondria dynamics are highly disturbed in metabolic diseases. It has been shown that mitochondrial function is upregulated in obese humans with and without NAFLD but strikingly, mitochondrial capacity is impaired in obese patients with NASH⁵⁰. Moreover, oxidative phosphorylation capacity and mitochondrial content in skeletal muscle is decreased in T2DM patients^{51,52}. This suggests that mitochondrial dynamics seem to change over the progression of the diseases. Interestingly, mitochondria are more fragmented in T2DM, indicating a disruption of the mitochondrial fusion/fission machinery. A connection of the fusion machinery and metabolism has already been demonstrated, as the depletion of Mitofusin 2 (MFN2) causes a decrease of mitochondrial activity that causes an increase of glucose uptake and a decrease in glycogen synthesis to compensate for the reduced activity⁴⁹.

Taken together, the regulation of mitochondrial dynamics is crucial for the maintenance of cellular homeostasis. Its deregulation can result in the disruption of metabolic health. One essential cellular mechanism involved in mitochondrial dynamics is autophagy, being responsible for the degradation of mitochondria.

1.5. Autophagy

Despite the degradation of organelles, like in mitophagy, autophagy is an essential cellular mechanism, responsible for the clearance of damaged cellular material like proteins but also metabolites, such as glycogen or lipids⁵³⁻⁵⁵. This regulated turnover and recycling process maintains a positive energetic balance upon starvation. Autophagy is highly conserved from yeast to human and ubiquitous in all eukaryotic cells. The three major forms of autophagy are macroautophagy, microautophagy and chaperone-mediated autophagy (CMA). Microautophagy occurs by the formation of vesicles that form at the lysosomal membrane and invaginate into the lysosomal lumen while engulfing its cargo⁵⁶. However, the molecular mechanism and relevance of microautophagy in the liver remains mostly unknown⁵⁷. All substrates in CMA contain a pentapeptide motif (KFERQ-like) that is recognized by cytosolic chaperone HSC70 to form a complex⁵⁸. At the lysosomal membrane this complex binds to the CMA receptor LAMP2A. The sub-

strate is then unfolded and internalized for degradation⁵⁹. Macroautophagy is the most prevalent form of autophagy⁶⁰. Macroautophagy initiates the formation of the limiting membrane that can be derived from different organelles e.g. ER or golgi. Several proteins are involved in the initiation step, including ULK1 and VPS34, which in turn recruits autophagy specific proteins like Beclin1. Receptors such as P62 simultaneously bind cargo and key components of the autophagosome machinery, facilitating the engulfment of the cargo⁶¹. Elongation of the membrane requires several complexes comprising amongst others ATG5 and ATG7, that conjugates LC3-I to the lipid phosphatidylethanolamine (PE) to form LC3-II⁶². The mature autophagosome traffics via microtubules and fuses with a lysosome to form an autolysosome. This step is mediated by RAB7 and RAB24⁶³. The cargo is finally degraded by lysosomal hydrolases and released into the cytosol⁶⁴.

Interestingly, autophagy seems to have a dual role in T2DM. Continuous autophagic activity can injure β -cells and furthermore cause autophagic cell death⁶⁵. However, recent data indicates, that obesity compromises hepatic autophagy and therefore contributes to hepatic insulin resistance⁶⁶. Furthermore, enhanced autophagy can protect β -cells from oxidative stress⁶⁷ and P62 deficient mice suffer from obesity and impaired glucose and insulin tolerance⁶⁸. Moreover, expression levels of Autophagy-related protein 7 (*Atg7*) are severely reduced in the livers of mice on a HFD and *db/db* mice. Restoration of hepatic ATG7 expression resulted in enhanced insulin action and systemic glucose control in *ob/ob* mice⁶⁹. Additionally, disruption of autophagy via knockdown of ATG5 and ATG7 caused increased triglyceride levels⁵⁵.

Like most intracellular trafficking processes, autophagy involves multiple membrane fusion events. These include for example the elongation process to engulf the cargo and also the fusion of autophagosomes with lysosomes. Membrane fusions usually include SNARE proteins, tethering factors and members of the Rab family⁷⁰.

1.6. The Rab family

Rab proteins are a family of small GTPases, which can switch between a membrane bound active GTP-state and a cytosolic inactive GDP-bound state. Inactive GDP-bound Rabs are activated on membrane surfaces by guanine exchange factors (GEFs). GDP is exchanged for GTP, which changes the conformation of the Rab protein and thereby makes it accessible for effector proteins. The antagonist to the GEFs are GTPase activating proteins (GAPs) that control the activity of the Rab proteins by hydrolyzing GTP to GDP and therefore inactivate the Rab⁷¹. Guanosine nucleotide dissociation inhibitors (GDI) maintain small GTP-ases in the inactive state by binding the prenylated C-terminus of the Rab, which usually keeps it anchored to the cell membrane and stabilize this cytosolic state⁷². In the active state, Rabs recruit specific effector proteins, like tethering factors, kinases, phosphatases and motors to the membranes. Those interact with the Rabs to control vesicle budding, un-coating and fusion.

Rabs are specifically associated with distinct cellular compartments (**Fig. 5**) and regulate organelle communication and cellular trafficking to sustain homeostasis. RAB32 controls the interaction of ER and mitochondria⁷³. Other examples are RAB3⁷⁴, which is associated with exocytosis⁷⁴, while RAB4 and RAB11 are related to recycling endosomes⁷⁵. RAB5 is associated to early endosomes and has been shown to be the master regulator of endosomal biogenesis and therefore a key player in endocytosis⁷⁶.

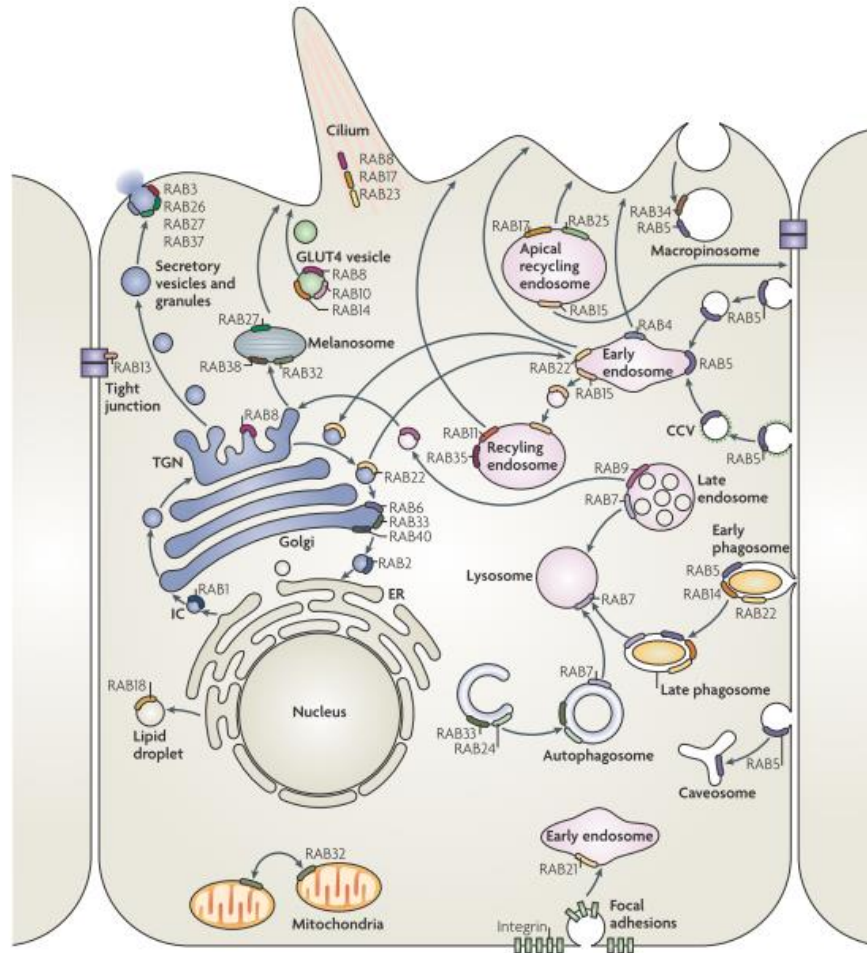


Figure 5: Localization and function of different Rabs.

RAB1 is located at the ER, RAB2 at the IC, both mediate ER- Golgi trafficking. Intra-Golgi trafficking is regulated by RAB6, RAB33 and RAB40. RAB24 and RAB33 mediate autophagosome formation. Trans-Golgi network to plasma membrane trafficking is controlled by RAB8 that also participates in GLUT4 translocation together with RAB10 and RAB14 and ciliogenesis together with RAB17 and RAB23. Exocytosis is regulated by RAB3, RAB26, RAB27 and RAB37. RAB32 participates in the fission of mitochondria. RAB5 is the master regulator of endosomal biogenesis. RAB22 mediates trans-Golgi network to endosome trafficking. RAB4, RAB11 and RAB35 control endocytic recycling. RAB15 is needed for trafficking for early endosome to recycling endosomes and recycling from apical endosomes to the basolateral plasma membrane while RAB17 and RAB25 mediate recycling from apical endosomes to the apical plasma membrane. RAB9 regulates late endosome to trans-golgi network trafficking. RAB7 mediates the maturation of late endosomes and their fusion with lysosomes. Adapted from⁷⁷

1.7. Endocytosis

Endocytosis is an essential cellular mechanism that mediates the uptake of various cargos for example activated signaling receptors like the insulin receptor, hormones or metabolites like LDL. There are several variations of endocytosis: **phagocytosis** is a process to take in relatively large particles e.g. the uptake of microorganisms in white blood cells. Upon binding of the particle to receptors on the phagocytic cell, the membrane extends in an actin-based movement resulting in pseudopodia that surround the particle. The resulting phagosome fuses with a lysosome for breakdown whereby some of the internalized proteins or nutrients can be recycled. In **receptor-mediated endocytosis** the internalized cargo first binds to a specific receptor at the cell surface that is localized in specialized regions of the plasma membrane, called clathrin-coated pits. Clathrin binding is mediated by adaptor proteins like the AP-2 complex that interacts with transmembrane proteins and is able to recruit other adaptor proteins. The clathrin pits bud from the PM and internalized cargo is transported to early endosomes for sorting and can either be degraded by late endosomes and lysosomes or recycled back to the cell surface⁷⁸. For proper execution of this process, a lot of different proteins are required. Soluble N-ethylmaleimide-sensitive-factor attachment receptor (SNAREs) for instance mediate the fusion of vesicles with their target membrane like lysosomes or the plasma membrane during exocytosis⁷⁹.

Members of the trafficking pathways have been extensively studied for their functional role in cellular trafficking but recent studies highlight their importance in the regulation of metabolism. Interestingly, trafficking components like RAB10 and RAB5 that are involved in endocytosis, were found to also take part in the control of metabolism. These findings combine two separate pathways and add a new layer of regulation to the field of metabolism.

1.8. The trafficking system in metabolic diseases

The uptake of glucose is dependent on the mechanics of trafficking. GLUT4, that is responsible for glucose uptake in muscle and adipose tissue, is regulated via a combination of exocytosis and endocytosis. Upon insulin binding GLUT4 exocytosis is stimulated. This is acquired by inactivation of AS160^{80,81}, a Rab GAP (inactivator), which subsequently causes activation of RAB2A, RAB8A, RAB14 and RAB10 function⁸². Strikingly, the loss of RAB10 (important for basolateral to common endosome transport⁸³) in adipose tissue leads to a 50% reduction in insulin-stimulated uptake of glucose in the adipose tissue due to reduction of GLUT4 translocation to the plasma membrane. Additionally, insulin induced suppression of hepatic glucose output was almost completely lost⁸⁴. Interestingly, the translocation of GLUT4 in response to insulin signaling is reduced in adipose tissue and muscle in a mouse model for T2DM and overexpression of GLUT4 could ameliorate the diabetic phenotype in *db/db* mice⁸⁵. Furthermore, it has been shown that disruption of the endosomal function by depletion of the endosomal biogenesis regulator RAB5 in mouse liver⁷⁶ leads to metabolic perturbations like hypercholesterolemia, hyperlipidemia, cholestasis, lipid and glycogen accumulation in the liver, hepatomegaly and hypoglycemia. The phenotype mimicked the Van Gierke's disease, characterized by a G6PASE deficiency. Intriguingly, the *in vivo* knock down of the endosomal system leads to improvement of the hyperglycemic phenotype of *db/db* mice⁸⁶. Additionally, the retriever-CCC-WASH complex, a protein downstream of RAB5 action that is involved in cargo sorting⁸⁷, was shown to be involved in lipid homeostasis. Moreover, the liver specific loss of COMMD1 in mice displayed increased LDL levels, accompanied by decreased LDL uptake in the liver caused by mislocalization of LDLR. Furthermore, patients with mutations in the CCC complex (CCDC22) exhibit hypercholesterolemia⁸⁸. Familial hypercholesterolemia (FH) is a genetic disorder characterized by high LDL levels, which may cause the deposition of cholesterol rich fat depots in the face or limbs and to early cardiovascular disease. The disease originates from mutations in the lipoprotein pathway that result in the insufficient clearance of LDL through endocytosis^{89,90}. These findings highlight the importance of cellular trafficking mechanisms like endocytosis for whole body metabolism and reveal a novel connection between two, largely separately studied mechanisms.

1.9. Screen for new trafficking candidates with a role in metabolism

The preceding data point out the importance of trafficking components for regulating metabolism. However, most of the known trafficking regulators with a role in metabolism were not suitable for treating metabolic diseases, e.g. the RAB5 KD led to the complete loss of the degradative pathway, leading to pleiotropic effects. To further elucidate the role of the trafficking system in glucose metabolism and to find possible treatments for metabolic diseases, a screen for new candidates of the trafficking system was performed and their potential role in metabolism and metabolic diseases investigated. Over 1200 knock-out (KO) mice previously phenotyped by the German Mouse Clinic (GMC) were screened for alterations in glucose homeostasis indicated by changes in oral glucose tolerance tests (OGTTs). Next, the candidates got sorted with > 20% deviation in OGTT from the control for function via *David pathway analysis* and picked out several that were associated with vesicular trafficking. SGIP1, RAB3IP and CHMP4C KO mice showed deteriorations, while RAB24 KO mice had an improvement in glucose clearance.

1.10. Candidates

1.10.1. SGIP1

Src homology 3-domain growth factor receptor-bound 2-like (endophilin) interacting protein 1 (SGIP1) was shown to be involved in clathrin-dependent endocytosis, where it binds to membrane phospholipids and therefore mediates membrane tubulation. Furthermore, SGIP1 interacts with the AP-2 complex that is responsible for the formation of clathrin-coated pits. The involvement of SGIP1 in clathrin-dependent endocytosis seems to be target specific, as it was shown to be needed for transferrin but not for EGF uptake⁹¹. *Sgip1* was first identified and found to be elevated in obese and obese diabetic Israeli sand rats (*Psammomys obesus*). Moreover, *Sgip1* was found to be upregulated in the hypothalamus of lethal yellow agouti (A(y)/a) mice and intracere-

broventricular infusion of antisense oligonucleotide targeting SGIP1 lead to weight loss in *P. obesus* and Sprague Dawley rats by reduction of food intake⁹². Interestingly, *SGIP1* SNPs (single-nucleotide polymorphisms) have been associated with fat mass in the Mauritius Family Study where fat mass was reduced by up to 9.4%⁹³.

1.10.2. CHMP4C

Charged Multivesicular Body Protein 4C (CHMP4C) is a subunit of the ESCRT III Complex (Endosomal Sorting Complexes Required for Transport) that is required for multivesicular body formation. Internalized cargo is sorted into a subdomain of the endosome. This subdomain then invaginates and ESCRT III proteins catalyze the scission to form a multivesicular body^{94,95}. Furthermore, CHMP4C has been shown to perform several roles during cytokinesis such as membrane remodeling, chromosome alignment and segregation⁹⁶ as well as regulation of cellular abscission⁹⁷. Moreover, CHMP4C was associated with several diseases like budding of HIV-1⁹⁸ and in a Genome wide association study (GWAS) addressing ovarian cancer⁹⁹

1.10.3. RAB3IP

RAB3A interacting protein (RAB3IP), also called RABIN3 or RABIN8 is a GEF for RAB8¹⁰⁰ and RAB3¹⁰¹. As stated earlier, Rab proteins switch between a GDP- and a GTP-bound state. GEFs stimulate the dissociation of GDP from the Rab protein which leads to GTP loading and thus a switch to the active form¹⁰². RAB3 is associated with regulated exocytosis that is among others required for food digestion, hormone secretion and glucose uptake⁷⁴ while RAB8 mediates trans-Golgi network to basolateral membrane trafficking^{103,104}. RAB3IP itself has recently been shown to be a proto-oncogene for several cancers like colorectal cancer, major salivary carcinoma and cervical cancer¹⁰⁵ and furthermore to induce an invasive phenotype in gastric cancer cells¹⁰⁶.

1.10.4. RAB24

RAB24 is a small atypical GTPase as it shows insufficient prenylation, lower GTPase activity and therefore occurs predominantly in the GTP-bound active state¹⁰⁷. It is localized at the endoplasmic reticulum/cis-Golgi region and on LE structures¹⁰⁸. Upon starvation, RAB24 co-localizes with LC3, a marker for autophagosomes, where it is required for autophagosome maturation¹⁰⁹. Recently, RAB24 has been shown to interact with RAB7 in order to enable autophagosome-lysosome fusion that is obligatory for lysosomal degradation⁶³. RAB24 has been associated with several diseases, e.g. hepatocellular carcinomas¹¹⁰, canine ataxia¹¹¹ and pediatric tuberculosis¹¹². Although RAB24 is associated with the regulation of autophagy and autophagy has been shown to be disturbed in diabetes, the role of RAB24 in metabolic diseases is still unraveled.

1.11. Objective

Metabolic diseases like T2DM and NASH are on the rise, but still, the underlying mechanisms remain mostly undiscovered and therefore the possible treatments are limited. Based on previous data highlighting the importance of endosomal transport components in energy homeostasis, the aim of this study is to elucidate the novel connection of the trafficking system and metabolism. For this purpose, trafficking components that have a regulatory role in hepatic glucose and fat metabolism were identified and their potential as a target for treating metabolic diseases exploited.

Except for the SNP found for *SGIP1*, none of the candidates have been associated with metabolism or metabolic diseases. This work reveals the molecular role of the candidates in metabolism and elucidates their impact on whole body homeostasis. Furthermore, the association of the endosomal system with metabolic diseases in human patients and mice were investigated.

To investigate the novel function of the candidates in metabolism, KD experiments were performed in primary mouse hepatocytes or mouse livers and analyzed for metabolic changes. *In vitro* functional assays were conducted to dissect the molecular

function of the proteins in metabolism. To examine mitochondrial respiration and glycolysis, seahorse assays were performed. To study gluconeogenesis, a glucose secretion assay was set up and for the interrogation of lipid metabolism cholesterol secretion and uptake were measured. To elucidate if those functions have an impact on whole body metabolism, physiological experiments like GTTs or histological analysis of organs were performed *in vivo*. Additionally, in order to reveal a role of the candidates in diseases, expression levels of the candidates were measured in mouse models of metabolic diseases like *db/db* or HFD mice and additionally in human patients with obesity, NAFLD or NASH.

2. Results

2.1. *SGIP1* expression is upregulated in human patients with NASH

To investigate the relevance of my candidates for human metabolic diseases, I examined their expression in patients with fatty liver disease with and without steatosis and NASH patients. I found *SGIP1* mRNA expression to be strongly upregulated in the livers of NASH patients (**Fig. 6a**). However, this increase cannot be attributed to hepatocytes as no *Sgip1* mRNA expression could be detected in primary mouse hepatocytes. Furthermore, mRNA expression of *Sgip1* occurs predominantly in the brain^{92,91} hence, liver specific targeting did not seem to be advantageous. Although, the question of how *SGIP1* mediates food intake needs to be further elucidated and contributes to the regulation of body fat^{92,113}, it nevertheless marks another connection of the endosomal system and energy balance and constitutes an interesting target for weight control in obesity and possibly the amelioration of NASH.

2.2. *CHMP4C* expression is upregulated in human NASH patients and regulates *G6PASE* expression *in vitro*

I found *CHMP4C* mRNA expression upregulated in the livers of NASH patients and *db/db* mice (**Fig. 6 b, c**). To obtain insight in the function of *CHMP4C*, I conducted a siRNA KD in primary mouse hepatocytes and found *G6Pase* levels upregulated in mRNA and protein levels upon the KD (**Fig. 6d-f**). As *G6PASE* is one of the rate limiting enzymes for gluconeogenesis¹¹⁴, I inquired whether loss of *CHMP4C* altered the secretion of glucose. The output of glucose was not changed in either basal conditions or after stimulation of gluconeogenesis or stimulation with insulin (**Fig. 6g**). As the *CHMP4C* KO mice from IMPC showed a decrease in whole body glucose tolerance, I investigated if this could be attributed to *CHMP4C* function in the liver and performed a liver specific knock down via Lipid Nanoparticle containing siRNA targeting *CHMP4C*. Although 60%

reduction of *Chmp4c* mRNA expression levels was obtained (**Fig. 6h**), no alterations in blood glucose levels could be observed (**Fig. 6i**), nor did changes in serum insulin, cholesterol or triglyceride levels occur. Although, CHMP4C seems to play a role in the regulation of G6PASE in hepatocytes this doesn't seem to affect whole body glucose homeostasis.

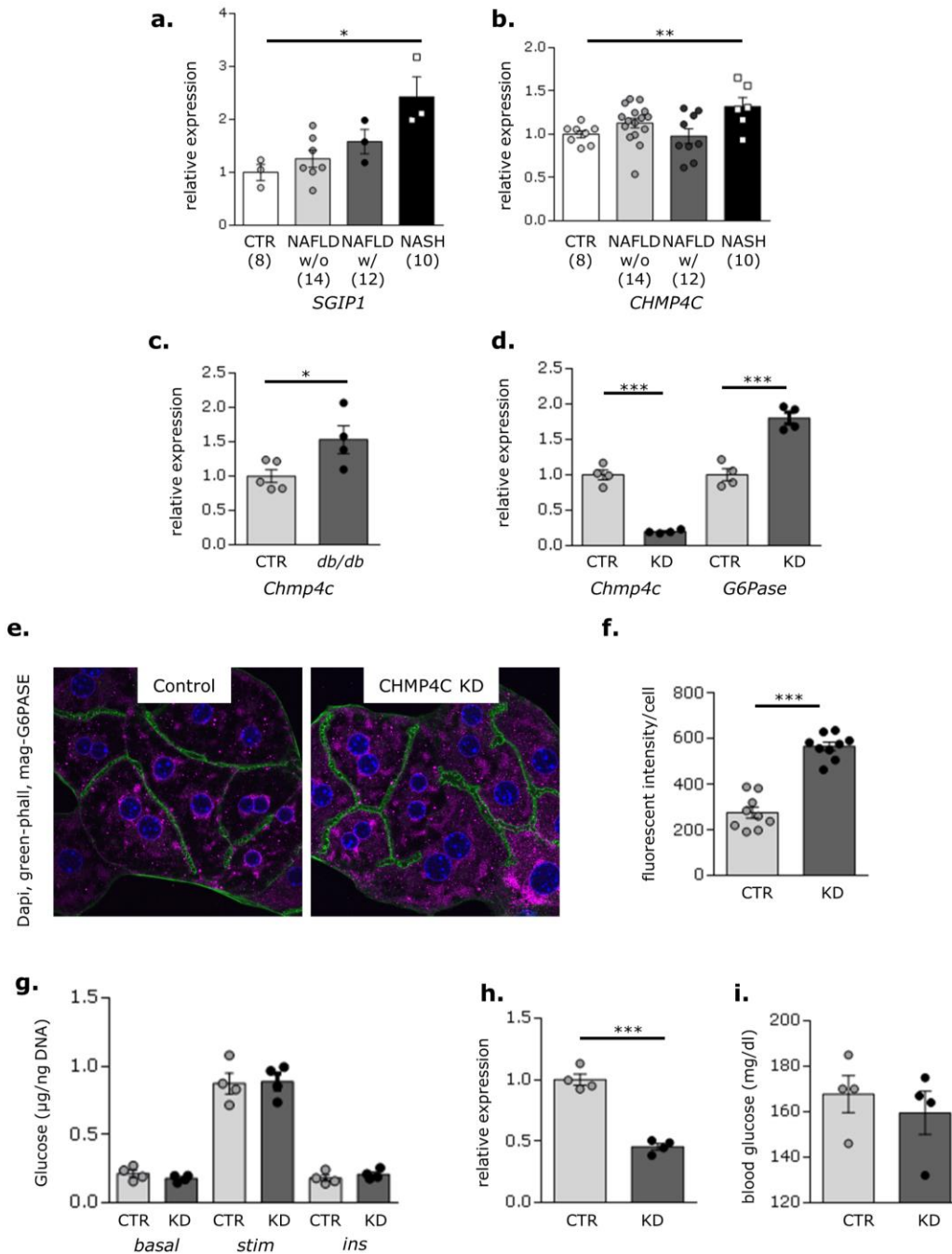


Figure 6: *SGIP1* and *CHMP4C* expression in patients with hepatic steatosis.

Expression levels of *SGIP1* (a) and *CHMP4C* (b) in patients with NALFD +/- steatosis and NASH versus healthy controls. (c) Relative expression of *Chmp4c* in *db/db* mice versus controls. (d) Relative expression of *Chmp4c* in primary hepatocytes after 3 days of RNAi treatment (40 nM). (e) Representative confocal images (maximal projections of 3-5 merged middle confocal sections) of polarized primary hepatocytes in collagen sandwich stained for dapi, phalloidin (green) and G6PASE (magenta), scale bar = 20 μ m. (f) Quantification of the mean fluorescent intensity per cell for G6PASE (e) of at least 20 cells per condition using Fiji. (g) Glucose levels after stimulation with either basal medium or stimulation medium (basal medium + 100 nM glucagon, 100 μ M forskolin and 100 nM dexamethasone) or stimulation medium supplemented with 100 nM insulin. All measured after 3 days of RNAi (40 nM) in primary hepatocytes. (h) Relative expression of *Chmp4c* in the liver after RNAi treatment. (i) Fasted blood glucose levels after 5 days of KD. All treated with control or *CHMP4C* KD siRNA (0.5 mg/kg) transfected with InvivoFectamin (N=4 animals per condition). (mean +/- SEM). P-value: two-tailed paired Student's t-test.

2.3. *Rab3ip* is differentially expressed in *db/db* and HFD mice

I found *Rab3ip* mRNA expression strongly reduced in the livers of *db/db* mice (**Fig. 7a**) but conversely upregulated in HFD mice (**Fig. 7b**). Although I did not find any changes in glucose or lipid metabolism caused by RAB3IP KD *in vitro*, I still performed the liver specific KD with LNPs as the RAB3IP KO mice in the IMPC screen showed decreased whole body glucose tolerance and less circulating insulin levels. The first KD of RAB3IP resulted in an increase of fasting blood glucose levels (**Fig. 7f**) and decreased levels of serum albumin and total protein (**Fig. 7d, e**), which can be linked to its secretory role. Inconclusively, the second KD resulted in a decrease of fasted blood glucose levels (**Fig. 7h**) without changes in serum albumin or total protein (data not shown) although the mRNA expression of *Rab3ip* was reduced to a larger extent in the second KD (**Fig. 7c, g**). Since *RAB3IP* did not show differential expression in the human NASH patients and exhibited inconclusive results upon the liver specific KD, it might not be applicable as a target for conquering metabolic diseases but nonetheless elucidates the importance of the endosomal system in metabolism.

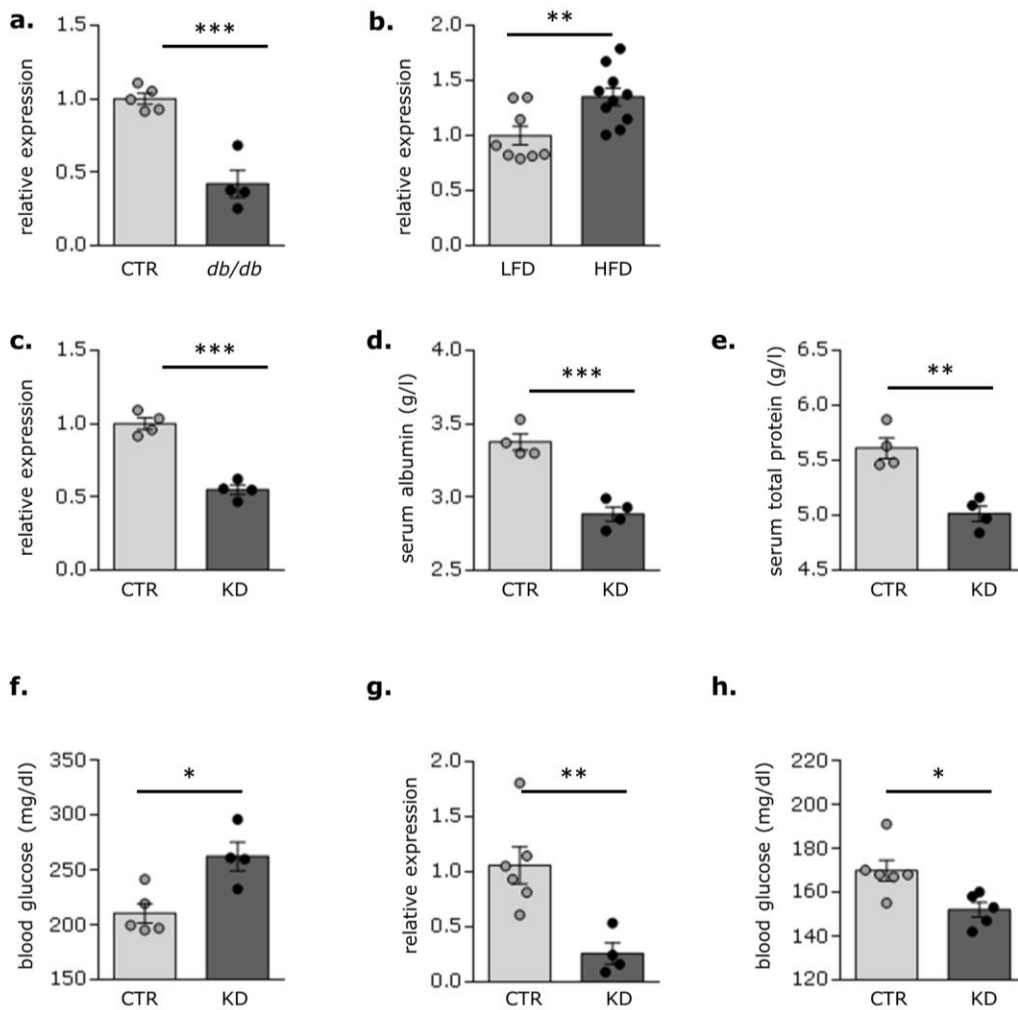


Figure 7: *Rab3ip* was differentially regulated in *db/db* and HFD mice.

Relative expression of *Rab3ip* in *db/db* (a) and HFD (b) mice versus controls. (c & g) Relative expression of *Rab3ip* in the liver after 3 days of RNAi treatment. Serum parameters for albumin (d) and total protein (e). Fasted blood glucose levels (f & h) after 3 days of KD. All treated with control or RAB3IP KD siRNA (0.5 mg/kg) transfected with InvivoFectamin (N=4 animals per condition). (mean +/- SEM). P-value: two-tailed paired Student's t-test.

2.4. *RAB24* expression is highly increased in patients with fatty liver disease

To investigate if *RAB24* is relevant for human metabolic diseases, I studied its expression in two independent human cohorts of patients. In the first cohort, samples and correlation analysis were provided by Matthias Blüher and consisted of obese patients versus healthy controls. I performed a qPCR that showed a striking 3-fold increase of hepatic *RAB24* expression in obesity (**Fig. 8a**). This was accompanied by a positive correlation of *RAB24* with BMI and a negative correlation with the Clamp GIR (**Fig. 8 c, d**). Additionally, positive correlations with liver fat ($r=0.346$, $p=0.03$), visceral fat ($r=0.375$, $p=0.02$), free fatty acids ($r=0.34$, $p=0.03$), HDL-cholesterol levels ($r=0.367$, $p=0.02$) and leptin ($r=0.46$, $p=0.005$) could be observed and highlighted the association of hepatic *RAB24* levels with glucose and lipid homeostasis.

Excess accumulation of lipids in the liver can lead to NAFLD and possibly further to non-alcoholic steatohepatitis (NASH). To determine the importance of *RAB24* in these more severe conditions of the liver, I tested hepatic *RAB24* expression of patients with NAFLD (-/+ steatosis), and NASH in comparison to healthy controls, obtained from Michael Roden. Intriguingly, *RAB24* was upregulated in NAFLD + steatosis patients and NASH patients (**Fig. 8 b**). Sofiya Gancheva furthermore performed a correlation analysis with the samples. The alterations in expression were accompanied by a negative correlation with whole body insulin sensitivity and positively correlated with hepatocellular lipids (**Fig. 8 e, f**). Additionally, positive correlations with IL6 ($r=0.39$, $p=0.039$), a cytokine pathway activator and liver 8-oxo-guanosine ($r=0.16$, $p=0.036$), a marker that corresponds to increased oxidative DNA damage, could be observed. Altogether, these data show the relationship between increased *RAB24* expression levels and metabolic diseases in humans.

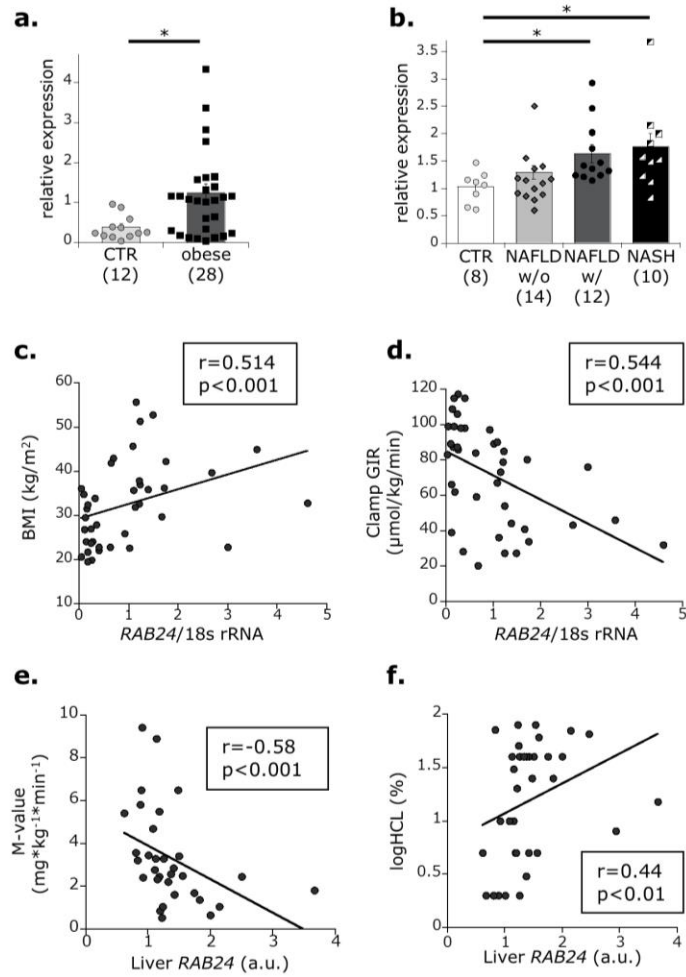


Figure 8: Hepatic *RAB24* expression was upregulated in obese, NAFLD and NASH patients. Relative hepatic expression of *RAB24* of obese patients (a) and patients with NALFD +/- steatosis and NASH (b) compared to healthy controls. (c, d) Spearman's correlation analysis of hepatic *RAB24* in a cohort of obese patients compared to healthy controls for BMI and Clamp glucose infusion rate (GIR). (e, f) Spearman's correlation analysis of hepatic *RAB24* in patients with NALFD +/- steatosis and NASH patients compared to healthy controls for M-value and liver fat (HCL).

2.5. RAB24 KD improves glucose clearance and serum lipids

To investigate the function of RAB24, I performed a liver specific KD with the aid of LNPs. Five days post LNP treatment, hepatic *Rab24* mRNA was 60% (**Fig. 9a**) and RAB24 protein levels 75% reduced (**Fig. 9b, c**). The mice showed no changes in body weight (**Fig. 9d**) but exhibited a decrease in liver to body weight ratio (**Fig. 9e**). In accordance to the oGTT data from the IMPC whole body KO mouse, I observed an improvement of glucose clearance (**Fig. 9f, g**). However, the KD had no effect on serum insulin levels, HOMA-IR (**Fig. 9h, i**) or insulin tolerance (**Fig. 9j**). Interestingly, insulin induced AKT activation was enhanced in skeletal muscle but not in adipose tissue or liver (**Fig. 9k-o**), suggesting a RAB24 dependent inter-organ communication, possibly mediated through a hepatokine. One hepatokine known to increase insulin sensitivity is FGF21^{119,120}. And indeed, mRNA expression as well as secretion of FGF21 was enhanced *in vitro* and *in vivo* (**Fig. 10a-d**). Strikingly, the KD of RAB24 that I performed in homozygous FGF21 KO mice, obtained from Kerstin Stemmer, caused no alterations in glucose clearance or AKT activation in skeletal muscle (**Fig. 10e-j**), indicating that the observed phenotype of RAB24 KD is FGF21 dependent. In contrast to the wildtype mice, heterozygous FGF21 KO mice exhibited increased insulin-induced AKT activation in the liver after RAB24 KD, that was absent in the homozygous controls (**Fig. 10k-r**), pointing towards an additional autocrine function of FGF21 in the RAB24 KD phenotype. I observed no changes in adipose tissue upon the KD of RAB24 in the FGF21 KO mice.

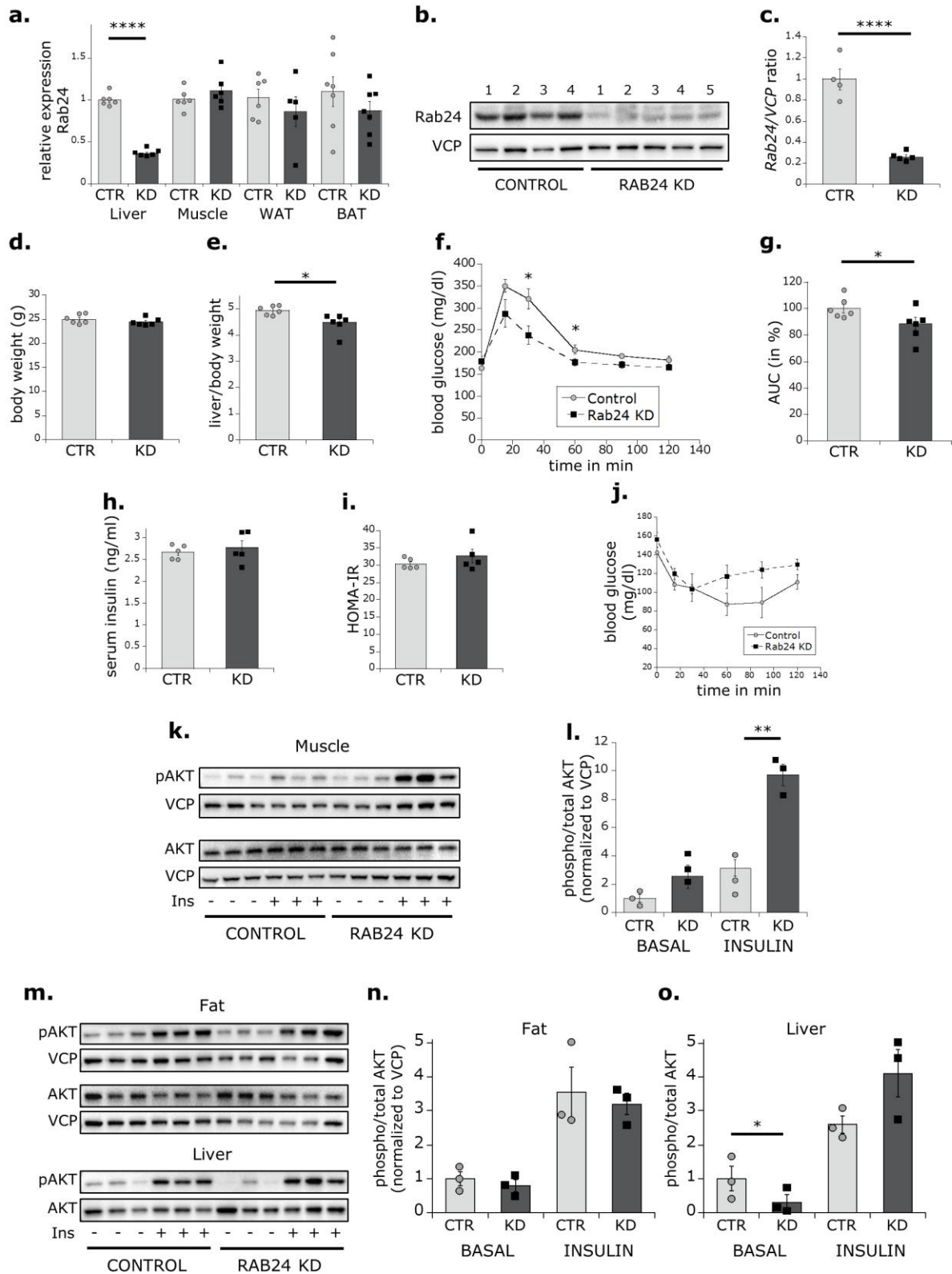


Figure 9: RAB24 KD improved glucose clearance and insulin signaling in mice.

(a) Relative mRNA levels of *Rab24* in liver, muscle, WAT and BAT after RAB24 KD. (b) Western blot of liver lysates after RAB24 KD and (c) quantification of (b). (d) Body weight and (e) liver to body weight ratio 6 days post RAB24 KD. (f) ipGTT (2 g/kg) and area under the curve (AUC) (g) after 6 h starvation on day 5 post RAB24 KD. (h) Serum insulin, (i) HOMA-IR and (j) ipITT (0.75U/kg) 5 days post RAB24 KD after 6h starvation. (k&m) Representative Western blots for AKT in muscle (k), fat and liver (m) of insulin-injected mice (0.75U/kg, 7 min) after 6 h of fasting and quantification thereof in (l, n, o). All animals treated with control and RAB24 KD LNPs (0.5 mg/kg) (N=6 animals per condition). (mean +/- SEM). P-value: two-tailed paired Student's t-test.

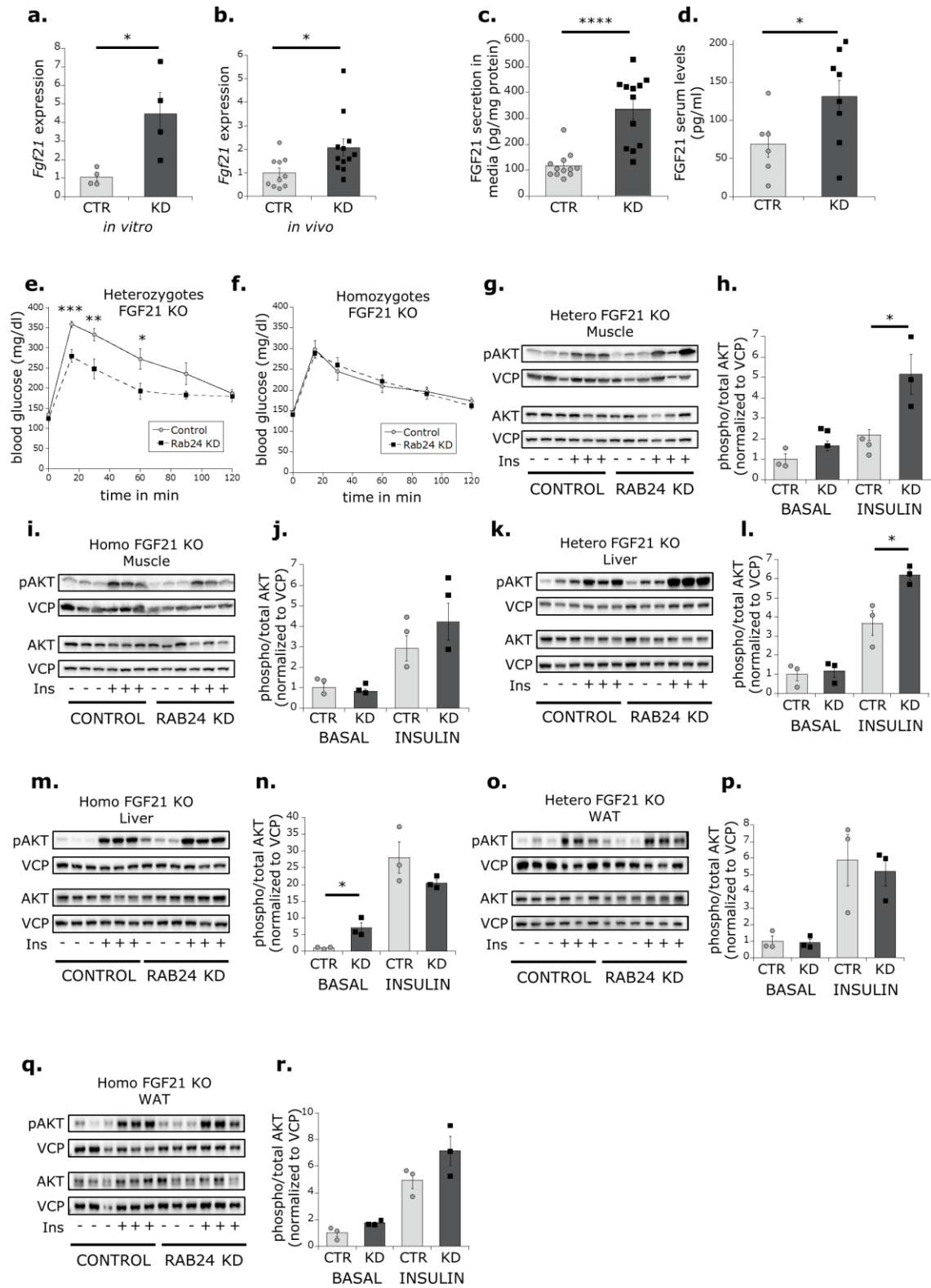


Figure 10: RAB24 effect on insulin activation was abolished in FGF21 KO mice.

(a) FGF21 mRNA levels and secretion (c) in primary hepatocytes after 3 days of KD. Primary hepatocytes treated with control (CTR) or RAB24 (KD) siRNA (40 nM) N=4 wells per condition. (b) FGF21 mRNA expression in liver and serum levels (d) after 6 days of RAB24 KD. ipGTT of heterozygous (e) and homozygous (f) FGF21 KO mice after 5 days of RAB24 KD. Representative Western blot analysis for AKT activation in skeletal muscle of heterozygous (g) and homozygous (i) FGF21 KO mice after insulin injection (0.75U/kg, 7 min) after 6 h fasting and quantification in (h) and (j), respectively. Representative Western blot analysis for AKT activation in liver of heterozygous (k) and homozygous (m) FGF21 KO mice after insulin injection (0.75U/kg, 7 min) after 6 h fasting and quantification in (l) and (n), respectively. Representative Western blot analysis for AKT activation in WAT of heterozygous (o) and homozygous (q) FGF21 KO mice after insulin injection (0.75U/kg, 7 min) after 6 h fasting and quantification in (p) and (r), respectively. All treated with control or RAB24 KD LNPs (0.5 mg/kg) (N=3 animals per condition). (mean+/-SEM) P-value: two-tailed paired Student's t-test.

Additionally to the alterations in glucose metabolism, the KD of RAB24 caused a decrease in total cholesterol, LDL and ApoB serum levels (**Table 1**). This effect could be due to alterations in the uptake or the secretion of LDL, thus, I measured the uptake kinetics of Dil labelled LDL with several time points^{76,121} in primary mouse hepatocytes. Interestingly, the KD of RAB24 (with a KD efficiency of 60% in mRNA and protein (**Fig. 11a-c**)) led to a small increase in LDL uptake (**Fig. 11d, e**), but without alterations in the expression levels of cholesterol transporters (**Fig. 11f**). The liver is not only responsible for the uptake of cholesterol, but is also a major source of secreted LDL¹²². Strikingly, the KD of RAB24 caused a decrease in cholesterol secretion from primary hepatocytes (**Fig. 11g**) and an increase in bile acid levels in liver lysates from 6 h fasted RAB24 KD mice (**Fig. 11h**). Altogether, these data provide evidence for a regulatory role of RAB24 in glucose and lipid metabolism.

Table 1: Serum metabolic parameters

Parameters	Control	Rab24 KD	p-value
Albumin (g/L)	29.98 ± 0.49	28.43 ± 1.68	0.362
ALT	34.25	48.88	0.336

(U/L)	± 4.24	± 13.85	
Apo A (g/L)	0.24 ± 0.003	0.23 ± 0.01	0.112
Apo B (mg/dl)	0.08 ± 0.005	0.07 ± 0.003	0.018
AST (U/L)	223.33 ± 44.40	277.00 ± 46.94	0.426
Cholesterol (mg/dl)	107.83 ± 2.37	89.17 ± 6.44	0.022
HDL (mg/dl)	73.35 ± 1.84	66.03 ± 2.90	0.059
LDH (U/L)	1128.00 ± 221.71	955.33 ± 68.08	0.474
LDL (mg/dl)	21.63 ± 1.1	15.92 ± 0.79	0.002
Total protein (g/dl)	54.26 ± 0.41	51.64 ± 2.52	0.288
Triglycerides (mg/dl)	101.17 ± 4.82	94.17 ± 6.11	0.389

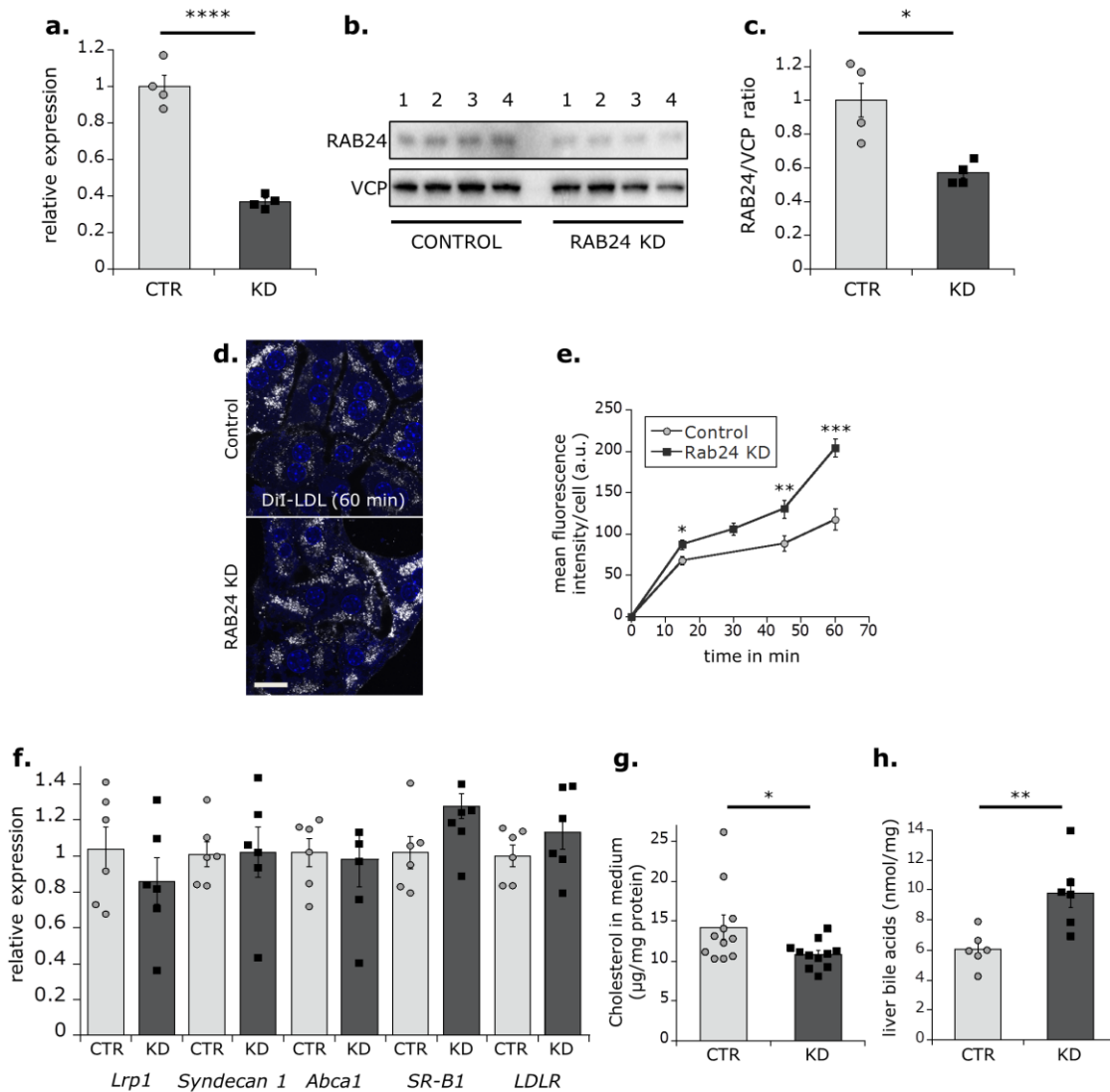


Figure 11: RAB24 KD led to an increase in LDL uptake and a decrease in LDL secretion.

(a) Relative mRNA levels of *Rab24* in primary hepatocytes after 3 days of KD (40 nM). (b) Western blot analysis after KD and quantification in (c). (d) Representative confocal images (maximal projection of 3 slices) DiI-LDL (grey) and Dapi (blue) in primary hepatocytes after 60 min and quantification with Fiji in (e). Scale bar 20 µm. (f) Relative mRNA expression of cholesterol transporters *Lrp1*, *Syndecan1*, *Abca1*, *SR-B1* and *LDLR* in the liver after control and RAB24 KD LNPs (0.5 mg/kg) (N=6 animals per condition). (g) Cholesterol levels secreted by primary hepatocytes after 4 days of KD. (h) Liver bile acids after 6 days of KD. All animals treated with control or RAB24 KD LNPs (0.5 mg/kg) (N=6 animals per condition). (mean±SEM) P-value: two-tailed paired Student's *t*-test.

2.6. RAB24 KD causes an increase in mitochondrial proteins

In order to reveal the underlying mechanisms of the RAB24 KD, I performed a RAB24 KD in mice and send the liver samples to Natalie Krahmer for quantitative proteomics analysis. She subjected the livers to liquid chromatography tandem mass spectrometry (LC MS/MS) and they underwent a combined analysis of the spectra from all samples. This led to the quantification of almost 5000 proteins at a false discovery rate (FDR) of 1% using the label-free quantification algorithm in MaxQuant. Using a rigorously filtered dataset with valid values for 3600 proteins, 622 were differentially expressed proteins (DEP): 287 were up- while 335 were downregulated (**Fig. 12a**). This was followed by a pathway enrichment analysis from Anne Loft, using KEGG and GO annotation (**Fig. 12b, c**). The majority of the upregulated proteins were part of metabolic processes, mainly carbon and pyruvate metabolism, degradation of amino acids and TCA cycle. Interestingly, most of these pathways are located in the mitochondria. Accordingly, the GO annotation showed an upregulation in 101 mitochondrial proteins and 21 proteins from carbon metabolism. This pronounced effect on mitochondria led me to further investigate the mitochondria. So I performed a RAB24 KD *in vivo* and send them to Annette Feuchtinger who performed paraffin sections for mitochondrial visualization. Strikingly, this showed a 20% increase in prohibitin, a protein of the inner mitochondrial membrane (**Fig. 12d, e**). Altogether, these data show a contribution of RAB24 in the regulation of carbon metabolism and mitochondrial proteins.

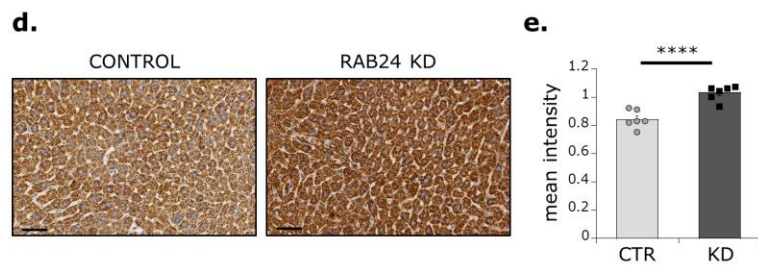
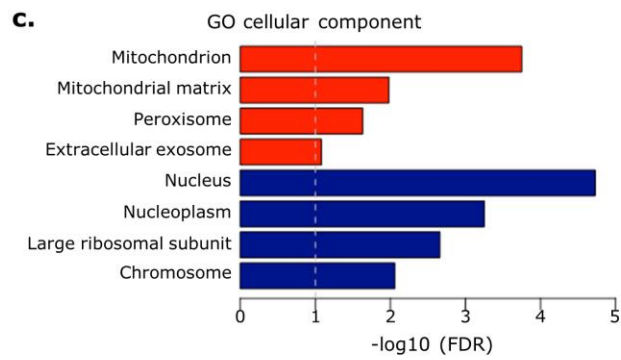
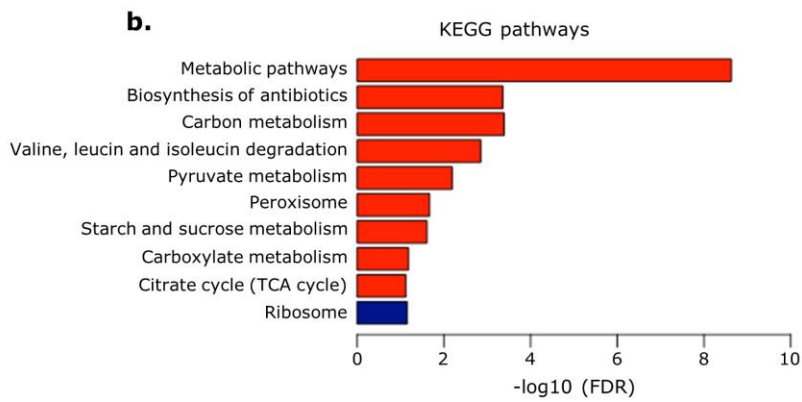
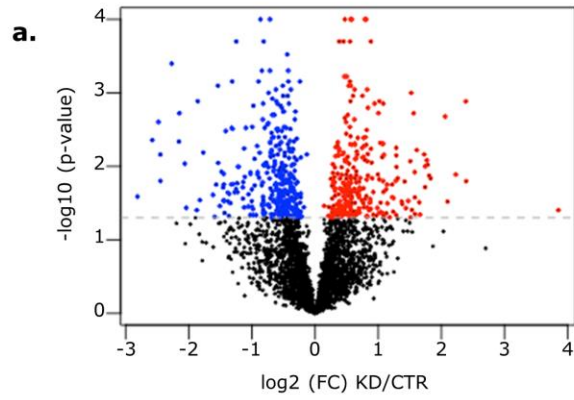


Figure 12: Up-regulation of mitochondrial proteins was induced after liver specific KD of RAB24.

(a) Fold changes (Log₂) of protein abundance after RAB24 KD wild type mice. Differentially expressed proteins (p-value <0.05) after RAB24 KD (red – up and blue – down). (b, c) Functional enrichment analysis of DEP; enriched pathways (FDR<0.1) for KEGG Pathways (b) and GO cellular component ontology (c). (d) Liver sections stained for prohibitin after RAB24 KD and quantification in (e). All measured after 6 days of KD of RAB24 with LNPs (0.5mg/kg) (N=6 animals per condition). (mean +/- SEM) P-value: two-tailed paired Student's *t*-test.

2.7. Reduction of RAB24 leads to an increase in mitochondrial mass and activity

The prominent effect of the RAB24 KD on mitochondrial proteins prompted a deeper analysis of mitochondrial mass and function. In accordance with the prohibitin staining, upon RAB24 KD the mitochondrial import protein TOM20 exhibited enhanced expression via IF staining *in vitro* and *in vivo* (**Fig. 13a-d**). The increase in mitochondrial mass was further confirmed by an increase in MitoTracker Green staining in primary hepatocytes *in vitro* and in isolated hepatocytes from RAB24 KD animals *in vivo* (**Fig. 13e, f**). This increase in mass was associated with the improvement of the oxygen consumption rate (OCR) *in vitro* during basal conditions, ATP production (induced with oligomycin) and maximal respiration capacity (induced with FCCP) (**Fig. 13g, h**). Strikingly, isolated hepatocytes after RAB24 KD *in vivo*, displayed a comparable induction of mitochondrial function (**Fig. 13i, j**), suggesting an increase in mitochondrial respiration also in the liver *in vivo*. The increase in MitoTracker Red staining *in vitro* as well as in isolated hepatocytes after *in vivo* KD further supported a regulatory role of RAB24 in mitochondrial function (**Fig. 13k, l**). The enhanced mitochondrial activity was accompanied by an increase in the production of ATP and reactive oxygen species (ROS) (**Fig. 13m, n**). However, no alteration in the abundance of carbonylated proteins was observed (**Fig. 13o**), indicating that the increased ROS levels caused by the RAB24 KD were not damaging for the cells. Altogether, these data show an increase of mitochondrial mass and function after the KD of RAB24 and highlight a new role for RAB24 in the regulation of energy metabolism.

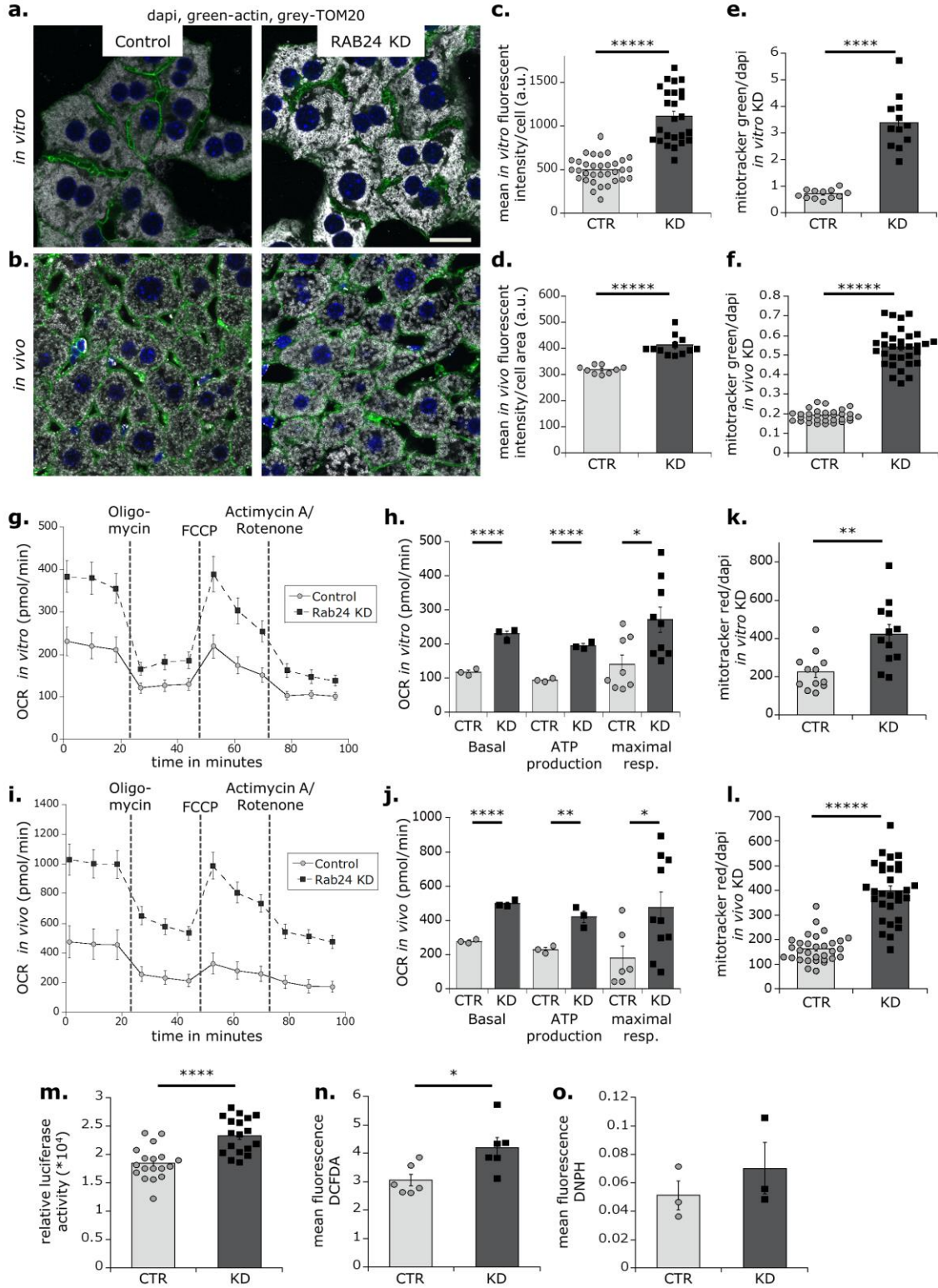


Figure 13: Reduction of RAB24 caused an increase in mitochondrial mass as well as function.

Representative single confocal section of primary hepatocytes (a) and liver sections (b) stained with dapi (blue), phalloidin (green) and TOM20 (grey) and quantification with Fiji in (c) and (d) after 3 or 6 days of RAB24 KD. MitoTracker Green (200 nM for 45 min) in primary hepatocytes after 3 days of RNAi *in vitro* (e) and in hepatocytes isolated after *in vivo* KD of RAB24 for 5 days (f) normalized to dapi. Seahorse measurements of the oxygen consumption rate (OCR) in basal conditions, ATP production and maximal oxygen consumption after 3 days of KD in primary hepatocytes *in vitro* (g, h) and in hepatocytes isolated after *in vivo* KD of RAB24 for 5 days (i, j) (N=10 wells per condition). MitoTracker Red (250 nM for 45 min) in primary hepatocytes after 3 days *in vitro* (k) and in hepatocytes isolated after *in vivo* KD of RAB24 for 5 days (l) normalized to dapi. (m, n, o) levels of ATP, ROS and carbonylation of proteins, respectively (N=6 wells per condition). All animals treated with control and RAB24 KD LNPs (0.5 mg/kg) (N=6 animals per condition). Primary hepatocytes treated with control or RAB24 KD siRNA (40 nM) and measured after 3 days after RNAi (mean +/- SEM). P-value: two-tailed paired Student's *t*-test.

2.8. RAB24 KD leads to increased glycolysis

Mitochondrial respiration and glycolysis are tightly linked, so possibly the KD of RAB24 could also affect glycolytic flux. Interestingly, I observed an increase in the extracellular acidification rate (ECAR) in basal conditions as well as under enhanced glycolytic activity (with oligomycin treatment), indicating enhanced glycolysis (Fig. 14a, b). As this increase was strongly reduced after Antimycin A and Rotenone (AA/Rot) treatment, inhibitors of mitochondrial respiration, this acidification might be dependent on oxidative phosphorylation. However, ECAR was still enhanced after AA/Rot treatment in the RAB24 KD, which was abolished after the injection of the glycolysis inhibitor 2-DG, suggesting an increase of glycolysis in the KD. Accordingly, the proteomics analysis revealed an upregulation of the glycolytic enzymes glucokinase, phosphoglucomutase, pyruvate kinase and pyruvate dehydrogenase complex (Fig. 14c). Furthermore, I observed an accumulation of lactate after the KD of RAB24, confirming the activation of glycolysis (Fig. 14g). Enhanced glycolysis was associated with increased glucose uptake under the same conditions as the glycolysis assay and upon glucose stimulation (Fig. 14d). In agreement, GLUT2 expression was increased *in vitro* and GLUT1 *in vivo* (Fig. 14e, f). Interestingly, RAB24 seems to play a role in the catabolic regulation of glucose, as no effect of glucose production via gluconeogenesis could be detected *in vivo* (Fig. 4h).

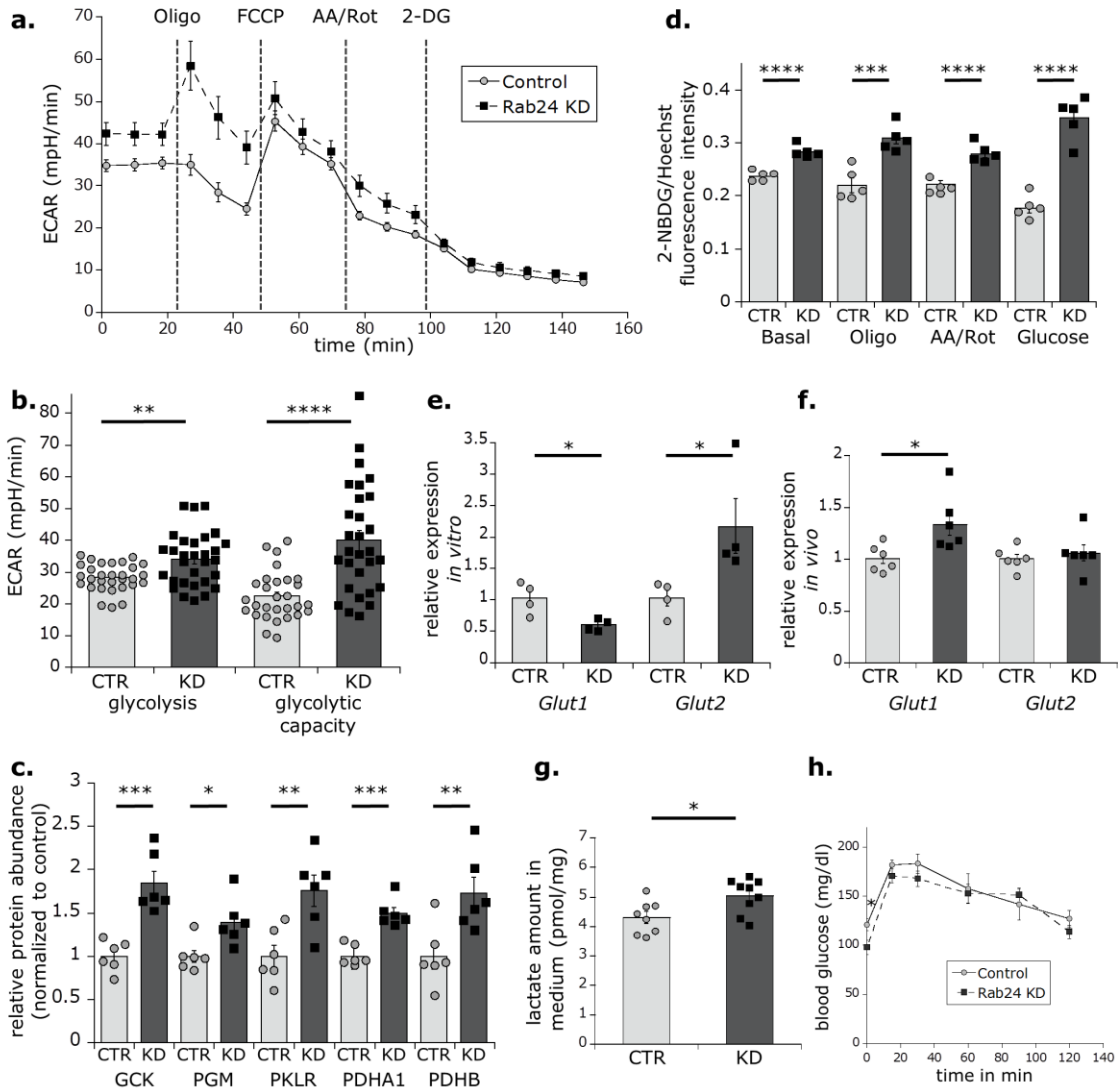


Figure 14: Depletion of RAB24 caused enhanced glycolysis.

(a) Extracellular acidification rate (ECAR) and their corresponding metabolic rates in (b) (N=10 wells per condition). (c) Protein abundance of glucokinase (GCK), phosphoglucomutase (PGM), pyruvate kinase (PKLR) and pyruvate dehydrogenase complex (PDHA1, PDHB) measured by proteomics after *in vivo* KD of RAB24. (d) 2-NBDG under basal, oligomycin (2 μ M), antimycin A (AA 1 μ M) + rotenone (Rot 1 μ M) and Glucose (25 mM) conditions. All measured after 3 days after RAB24 KD (40 nM) in primary hepatocytes. Relative mRNA expression of *Glut1* and *Glut2* *in vitro* (e) and in livers of mice 5 days after RAB24 KD (f). (g) Lactate level in medium secreted by primary hepatocytes after 4 days of RAB24 KD (40 nM). (h) ipPTT (2 g/kg) of control and RAB24 KD mice after 16 h of fasting. All animals treated with control or RAB24 KD LNPs (0.5 mg/kg) (N=6 animals per condition) (mean \pm SEM). P-value: two-tailed paired Student's t-test.

2.9. RAB24 KD causes an increase in autophagic flux and a reduction in mitophagy

An increase in mitochondrial mass can be achieved by activating biogenesis¹²³ or by repressing mitochondria degradation through fission-mediated mitophagy¹²⁴. To test mitochondrial biogenesis, I measured mRNA levels of *Pgc1 α* , *Pgc1 β* , *Nrf1* and *PPAR γ* in primary hepatocytes *in vitro* and in liver *in vivo* (**Fig. 15a, b**) and saw no alterations upon the KD of RAB24, suggesting that RAB24 does not interfere with mitochondrial biogenesis. RAB24 is known to be involved in the regulation of autophagy¹⁰⁹ and in nutrient rich conditions to be required for the interaction of autophagosomes and lysosomes⁶³. Interestingly, the KD of RAB24 resulted in higher protein levels of LC3II/I and a decrease in p62 levels in western blot (**Fig. 15c-e**) and IF staining (**Fig. 15i, j**) after starvation and inhibition of lysosome degradation with chloroquine. The additional increase of LC3II/I levels from fasted levels to chloroquine treatment in the KD indicates an enhancement in autophagy. This is in accordance with decreased p62 levels that suggest an increase in autophagosomal degradation (**Fig. 15c-e, i and j**). In accordance to former publications, the induction of autophagic flux in the KD was associated with an increase in LAMP1 protein levels (**Fig. 15k, l**)¹²⁵. Consistent with the observations *in vitro*, fasting mice for 12 h increased LC3II/I levels and decreased p62 levels in the KD compared to the controls. Chloroquine treatment (100 mg/kg for 3 hours) further enhanced the activation of LC3 (**Fig. 15f-g**), indicating an increase in autophagy also *in vivo*. Interestingly, these results are in discrepancy to former publications, that suggest a reduction of autophagy upon the KD of RAB24¹²⁵. However, this reduction only occurred with full medium but not under amino acid starvation, that initiates autophagy. This could indicate that RAB24 might occupy different functions in primary hepatocytes as in stable-expressing RAB24 cell lines in case of autophagy.

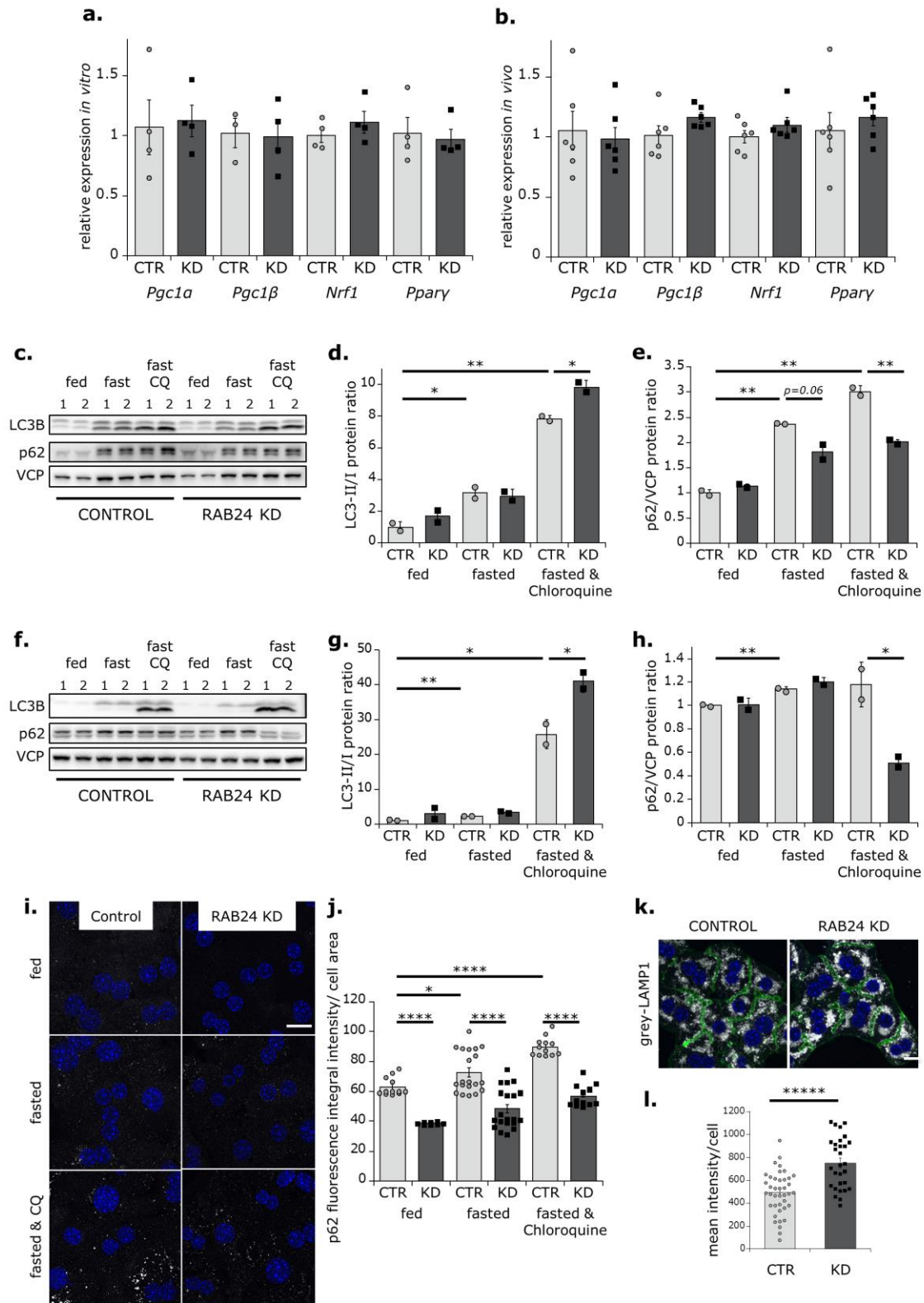


Figure 15: RAB24 KD resulted in an increase in autophagy.

Relative mRNA levels of mitochondria biogenesis markers *in vitro* (a) and *in vivo* (b) upon RAB24 KD. *In vitro* measured after 3 days of RAB24 KD (40 nM) in primary hepatocytes (mean +/- SEM). Mice treated with control or RAB24 KD LNPs (0.5 mg/kg) (N=6 animals per condition). (c) Representative Western blot analysis and quantification for LC3 (d) and p62 (e) in primary hepatocytes (mean +/- SD). Fed: full medium, fasted: serum starved for 12 h, fasted & CQ: 12 h starvation followed by 20 μ M chloroquine treatment for 3 h. (f) Representative Western blot analysis and quantification for LC3 (g) and p62 (h) in liver lysates of control or RAB24 KD mice. Mice were fed ad libitum, were fasted for 12 h, or were fasted for 12 hours followed by injection of 100 mg/kg chloroquine for 3 h (fasted & CQ) (mean +/- SD). Animals treated with control or RAB24 KD LNPs (0.5 mg/kg) (N=3 animals per condition). (i) Representative merged confocal images (three sections) of primary hepatocytes stained with dapi (blue) and p62 (grey) and quantification with Fiji in (j) full medium (fed) or serum starvation for 12 h (fasted), or serum starvation for 12 h followed by 20 μ M chloroquine for 3 h (fasted & CQ). (k) Representative single section confocal images of primary hepatocytes in collagen sandwich stained for dapi (blue), phalloidin (green) and LAMP1 (grey) and quantification in (l). Primary hepatocytes were treated with control or RAB24 KD siRNA (40 nM) and assays were performed 3 days after RNAi treatment (mean +/- SEM). P-value: two-tailed paired Student's *t*-test. P-value: two-tailed paired Student's *t*-test.

Autophagy has been shown to be required for glucose homeostasis *in vivo*. Here, ATG7, a major component of the autophagic family is necessary for proper insulin sensitivity and glucose metabolism in the liver⁶⁹. To further confirm a positive function of RAB24 in autophagy and to exclude similarities with ATG7 KD, I performed a side-by-side experiment, with depletion of RAB24 and ATG7 in the same primary hepatocyte culture plates (**Fig. 16a-k**). In agreement with the autophagic flux data, I observed a significant increase in LC3II/I protein ratio under RAB24 KD, indicating an increase in autophagy, concomitantly with an expected reduction upon ATG7 KD (**Fig. 16a, d**). ATG7 KD only induced a slight increase in TOM20 levels by IF and a marginal induction of OCR compared to RAB24 KD (**Fig. 16e-j**). Importantly, ATG7 depletion had no effect on FGF21 secretion in primary hepatocytes, further indicating separate regulatory mechanisms on energy metabolism and systemic metabolic control (**Fig. 16k**). In agreement with these data, I observed no effect on ATG7 protein levels in the liver after RAB24 KD (**Fig. 16l, m**).

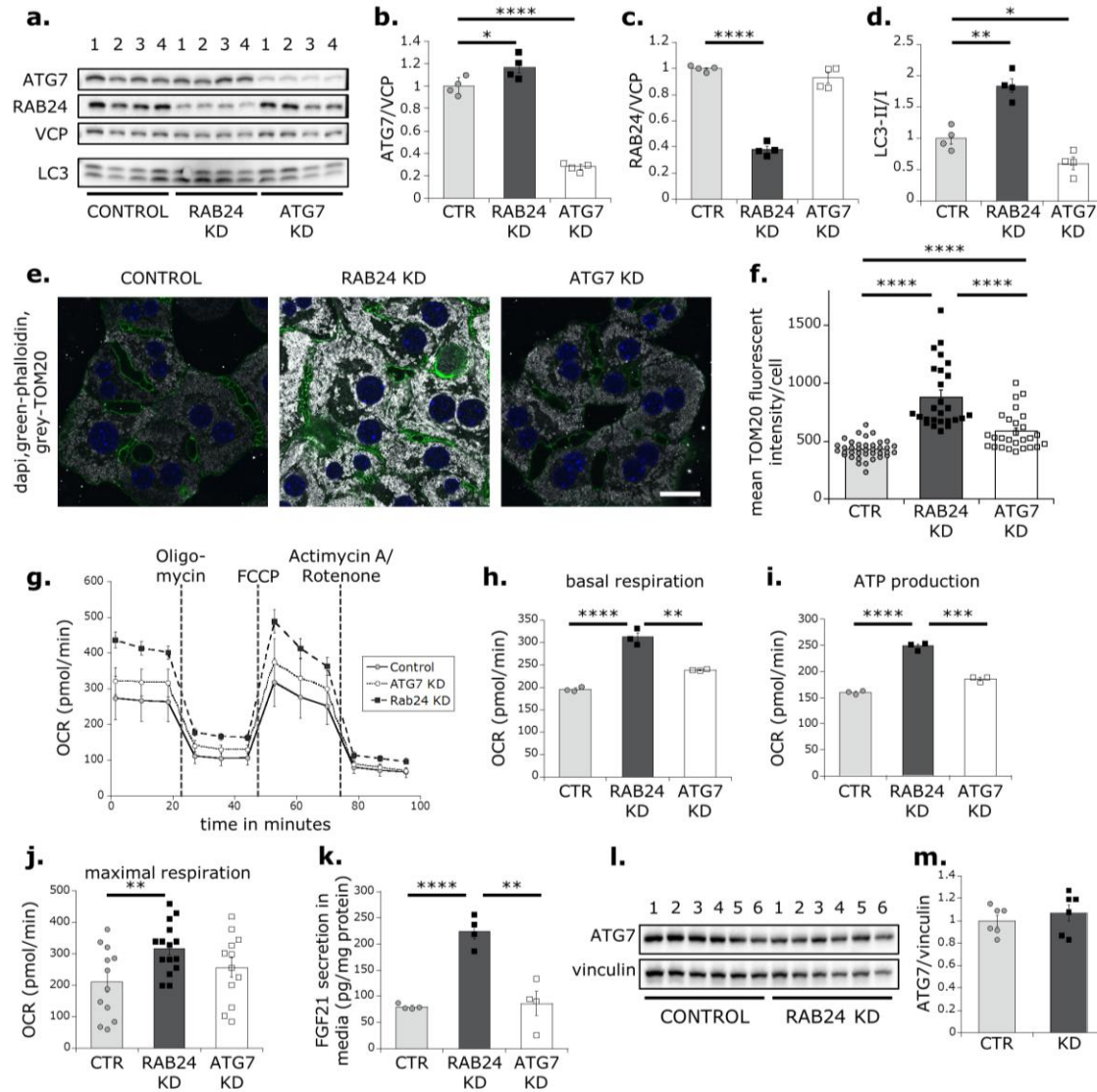


Figure 16: RAB24 KD differed from ATG7 KD.

(a) Western blot analysis for ATG7, Rab24 and LC3 of primary hepatocytes after RNAi treatment for 4 days and quantification thereof in (b-d). (e) Representative confocal images (single middle confocal sections) of primary polarized hepatocytes in collagen sandwich stained for Tom20 (grey), actin (green) and dapi (blue). (f) Quantification of the mean fluorescent intensity per cell from (e) using Fiji. (g) Seahorse measurements of the oxygen consumption rate (OCR) in primary hepatocytes and their corresponding metabolic rates (h-j) after 3 days of KD (N=6 wells per condition). (k) FGF21 secretion in primary hepatocytes. All measured after 3 days of RNAi against Rab24 and ATG7 (40 nM) in primary hepatocytes (mean \pm SEM). Scale bar = 20 μ m. (l) Western blot analysis for ATG7 of liver lysates from control (CTR) and Rab24 KD (KD) mice (0.5 mg/kg) (N=6 animals per condition), and quantification thereof in (m). P-value: two-tailed paired Student's *t*-test.

To investigate, whether the increase in mitochondrial mass upon the RAB24 KD is due to a reduction of mitophagy, I measured mitophagic flux using the nucleoid depletion assay^{126,127}. In control cells, stress induction with FCCP and oligomycin induced a reduction in cytoplasmic mtDNA, indicating the induction of mitophagy. Interestingly, the depletion of mtDNA was reduced by 2-fold upon RAB24 KD after FCCP and oligomycin treatment, suggesting a decrease of mitochondrial degradation (**Fig. 17a, b**). Additionally, fewer accumulation mitophagic vesicles could be detected after FCCP treatment both with and without lysosomal degradation (inhibited with chloroquine treatment) (**Fig 17e**). Jerome Gilleron performed electron microscopy with samples obtained from my KD experiments. The reduction of mitophagy upon RAB24 KD was further supported by fewer mitophagic events in electron microscopy, where mitochondria are counted, which are engulfed by double membranes (**Fig. 17c, d**). Furthermore, the co-localization of TOM20 and LAMP1, a marker for mitochondria and lysosomes respectively, was significantly reduced upon the KD of RAB24 (**Fig 17f, g**). Altogether, these data show a reduction of mitophagy upon RAB24 KD.

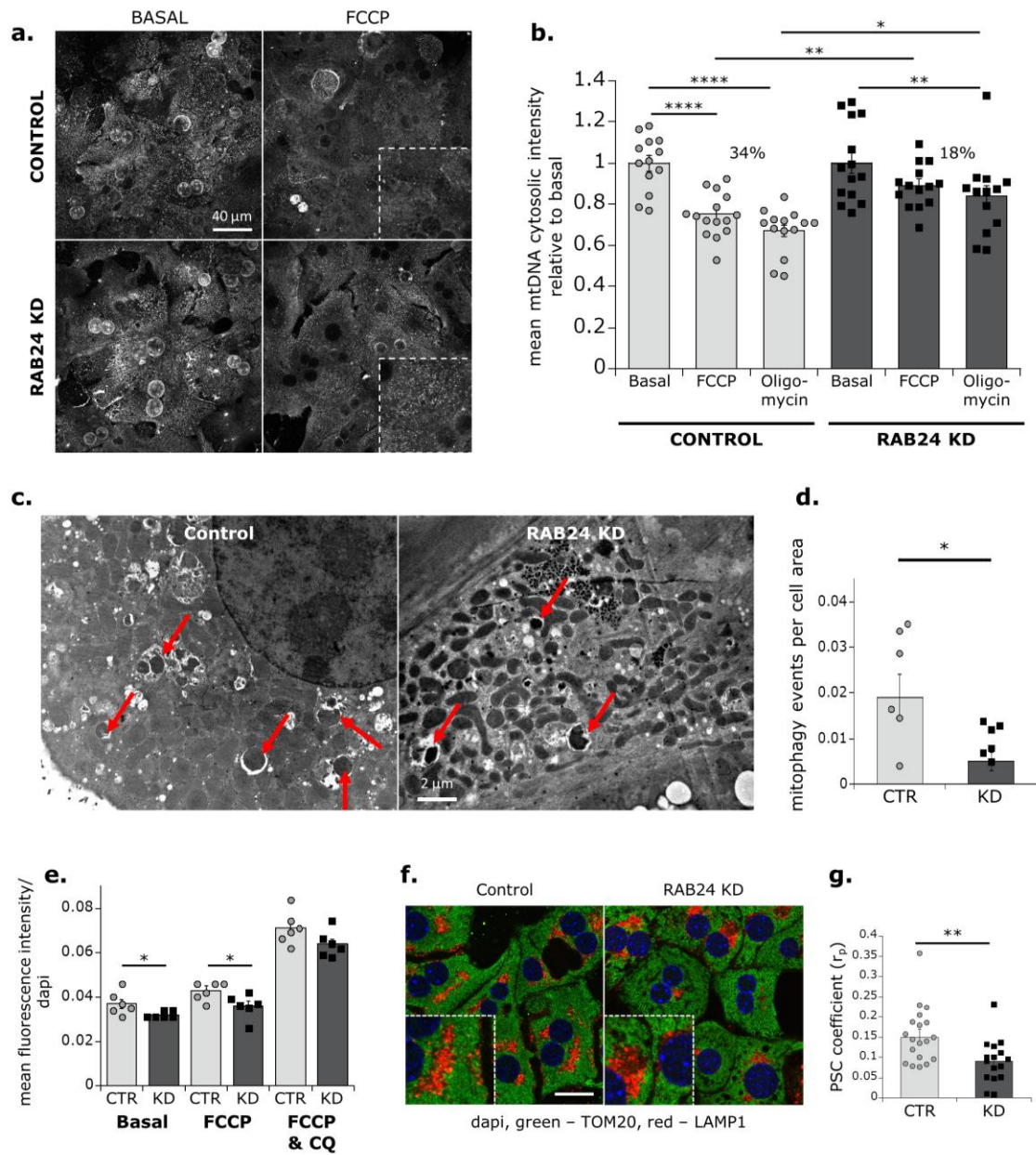


Figure 17: RAB24 KD led to a reduction in mitophagy.

(a) Representative single section confocal images of primary hepatocytes after 1 h of FCCP (20 μ M) treatment, stained for total DNA and dapi and quantification including treatment with oligomycin (10 μ M) with Fiji in (b). Scale bar 40 μ m. (c) Electron microscopy of mitophagic events and quantification in (d). Red arrows show mitophagic events. Scale bar 2 μ m. (e) Mitophagy flux in primary hepatocytes after 2 h treatment with 20 μ M FCCP w/ or w/o 20 μ M chloroquine. (f) Representative single section confocal images of primary hepatocytes in collagen sandwich stained for dapi (blue), TOM20 (green) and LAMP1 (red). Zoom-in indicated as insert. Scale bar 20 μ m. Person's and Spearman's correlation between the overlap in green and red channel analyzed with Fiji (g). Primary hepatocytes treated with control or RAB24 KD siRNA (40 nM) and assays were performed 3 days after RNAi (mean \pm SEM). P-value: two-tailed paired Student's *t*-test.

2.10. RAB24 KD causes an increase in mitochondrial connectivity by reducing mitochondrial fission

Mitophagy is induced by the fission of parts of the mitochondria resulting in smaller organelles designed for degradation^{128,129}. If RAB24 was involved in mitochondrial degradation directly at the level of mitophagy, reducing RAB24 should increase the amount of smaller mitochondria waiting to be degraded through the mitophagy pathway. Surprisingly, electron microscopy done by Jerome Gilleron on my KD samples, showed an increase in mitochondrial density, mitochondrial surface area, perimeter and form factor (complexity and branching) and a decrease in mitochondrial circularity (roundness) upon RAB24 KD that I performed *in vivo* in mouse liver tissue (**Fig. 18a-f**) or *in vitro* in primary hepatocytes (**Fig. 18g-o**), indicating more connected and slightly bigger mitochondria. Importantly, mitochondrial morphology was healthy with normal cristae structures (**Fig. 18i, j**).

Further investigation of mitochondrial connectivity, using IF staining of TOM20 in deconvoluted images that are skeletonized to visualize mitochondrial structures like branches and junctions, exhibited a better connected mitochondrial network *in vivo* (**Fig. 19a, b**), *in vitro* (**Fig. 20a**) and *in vivo* upon HFD (**Fig. 20e**). The number of branches as well as number of branches and their length was increased upon RAB24 KD (**Fig. 19c-e**, **Fig. 20b-d** and **Fig. 20f-h**).

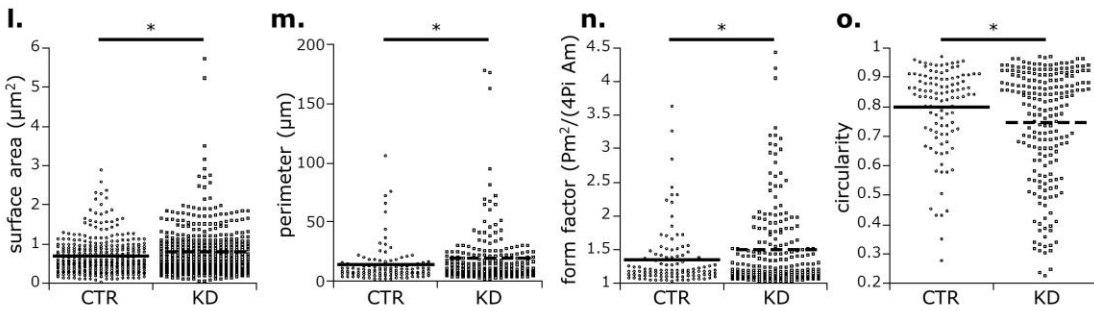
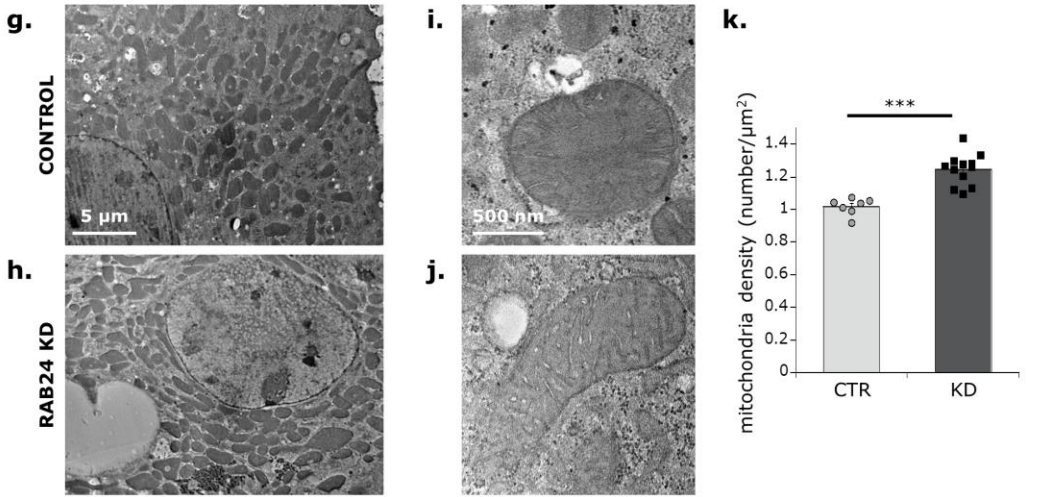
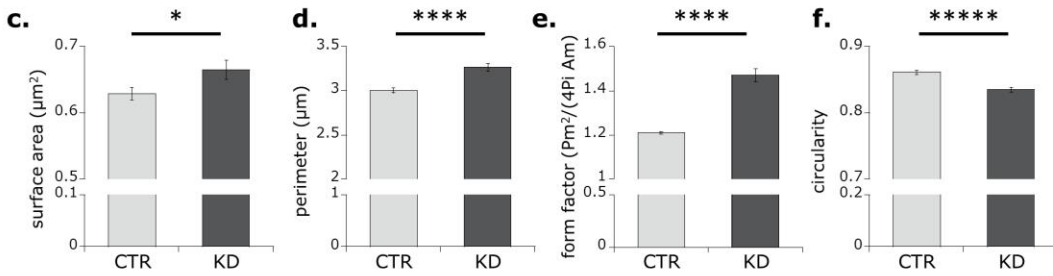
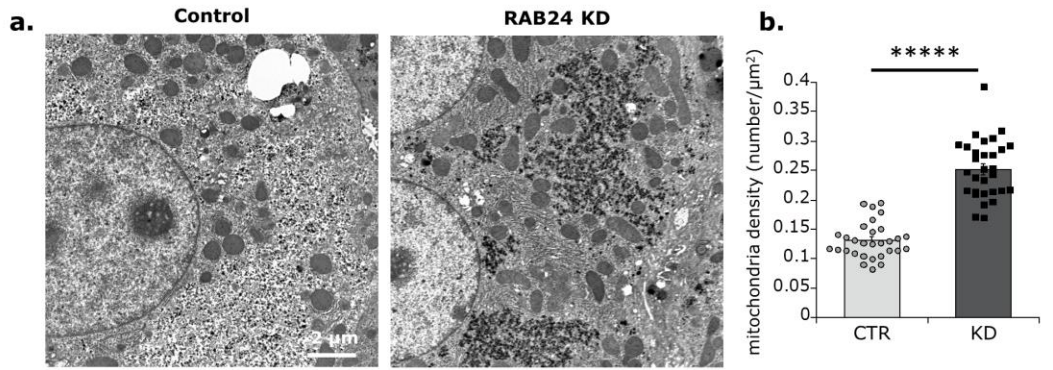


Figure 18: RAB24 KD caused a better connected mitochondrial network.

(a) Electron microscopy of mitochondria and quantification of morphology by morpho-EM for density (b), surface area (c), perimeter (d), form factor (e) and circularity (f) of control or RAB24 KD mouse livers. (N=30 cells for b, N=700-1000 mitochondria for c-f). Scale bar 2 μ m. All animals treated with control or RAB24 KD LNPs (0.5 mg/kg) (N=6 animals per condition). Electron microscopy of mitochondria in primary hepatocytes of control (g, i) and RAB24 KD (h, j); higher magnifications shown in (i) and (j). Quantification of mitochondria morphology of control (n=7) and RAB24 KD (n=12) cells by morpho-EM for mitochondria density (k), surface area (l), perimeter (m), form factor (n) and circularity (o). Scale bar 5 μ m. Zoom scale bar 500 nm. All measured after 3 days of treatment (40 nM) in primary hepatocytes (mean \pm SEM). P-value: two-tailed paired Student's *t*-test.

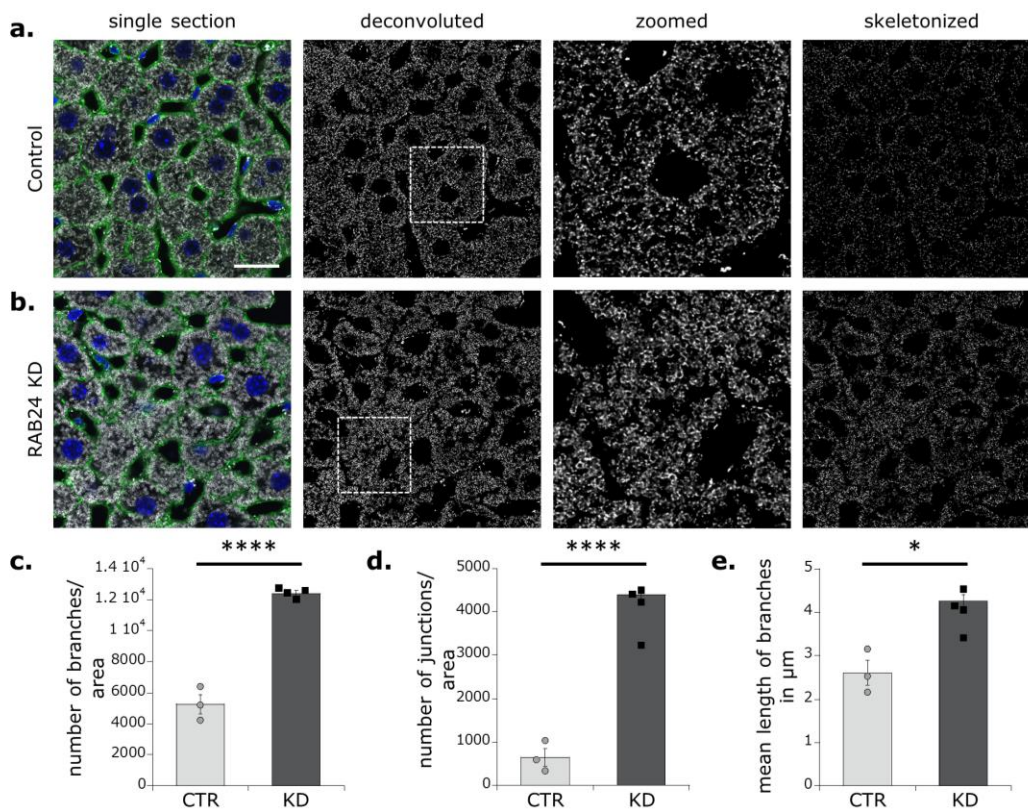


Figure 19: Depletion of RAB24 KD increased mitochondrial connectivity *in vivo*.

Representative single section confocal images of liver sections from control (a) and RAB24 KD (b) stained with dapi (blue), phalloidin (green) and TOM20 (grey) deconvoluted, zoomed and skeletonized. (c-e) quantification of number of branches, numbers of junctions per area and mean length of the branches. Scale bar 20 μ m. All animals treated with control or RAB24 KD LNPs (0.5 mg/kg) (N=6 animals per condition). P-value: two-tailed paired Student's *t*-test.

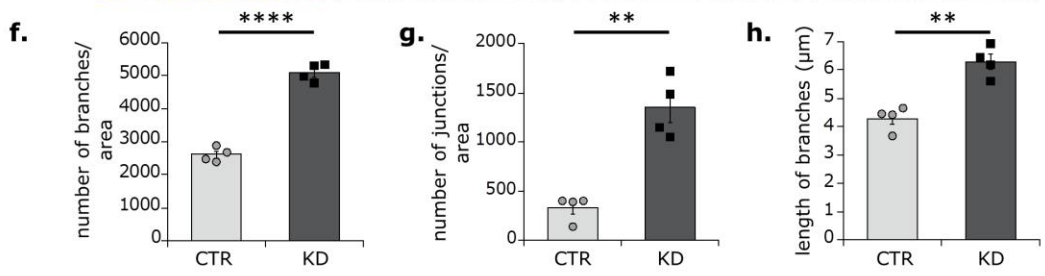
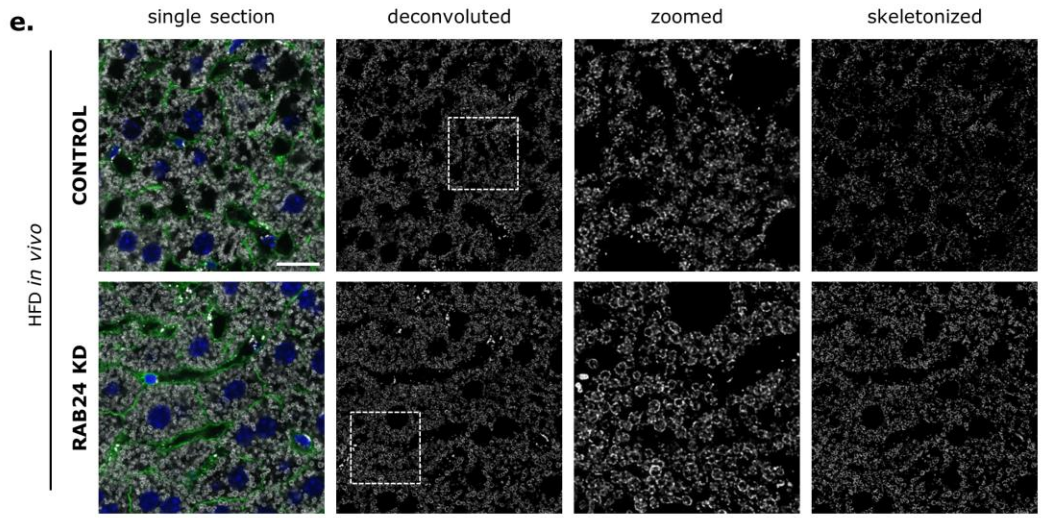
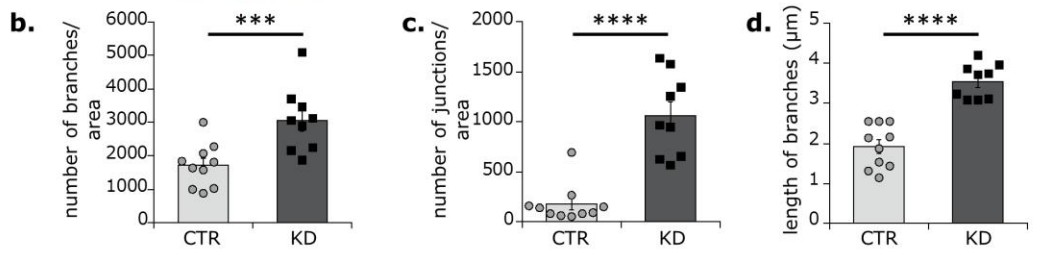
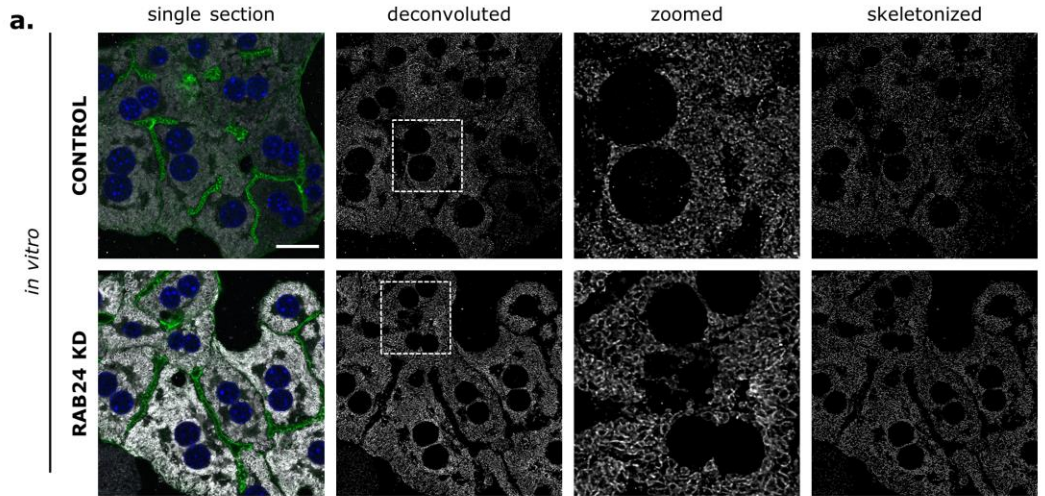


Figure 20: Rab24 KD increased mitochondrial area and connectivity *in vitro* and in HFD mice.

(a) Representative single section confocal images of primary hepatocytes after 3 days of RAB24 KD (40 nM) stained with dapi (blue), phalloidin (green) and TOM20 (grey) deconvolved, zoomed and skeletonized. (b-d) Quantification of number of branches, number of junctions per area and mean length of the branches of (a). (e) Representative single section confocal images of liver sections after HFD stained with dapi (blue), phalloidin (green) and TOM20 (grey), deconvolved, zoomed and skeletonized. (f-h) Quantification of number of branches, number of junctions per area and mean length of the branches of (e). Measured after 14 days of KD with LNPs (weekly injection; 0.5 mg/kg) and 6 h starvation in 15-week HFD mice. Scale bar 20 μ m (mean \pm SEM). P-value: two-tailed paired Student's *t*-test.

The occurrence of a wider connected mitochondrial network, without alterations in mitochondrial biogenesis, indicates a change in the mitochondrial fusion/fission cycle¹³¹. The proteomics analysis exhibited no alterations in the fusion regulators MFN1 and OPA1 (**Fig. 21a**). Likewise, IF staining showed no alterations in protein levels of MFN and MFN2 (**Fig. 22a-c**). However, I observed a reduction in the fission regulators Mitofission regulatory protein 1 (MTFR1) and the solute carrier family 25 member 46 (SLC25A46)¹³²⁻¹³⁴ in the proteomics analysis (**Fig. 21a**).

Mitochondrial fission is enhanced by the interaction of ER and mitochondria on organelle contact sites^{135,136}. Interestingly, a staining with KDEL (ER marker) and TOM20 (mitochondrial marker) showed an increased co-localization upon RAB24 KD (**Fig. 21b-c**), indicating greater contact of the two organelles. Mitochondrial fission is activated by the formation of the fission complex, that consists of the Mitochondrial Fission 1 protein (FIS1), Mitochondrial Fission Factor (MFF) and Mitochondrial Dynamics protein 49/51 (MID49/51). This fission complex initiates the recruitment of dynamin-related protein 1 (DRP1) to the membrane of mitochondria to commence fission^{128,137}. IF staining showed a reduction in DRP1 mean intensity per cell but no changes in FIS1 (**Fig. 21d-f**). Interestingly, the proteomics displayed no alterations in DRP1 protein abundance (**Fig. 21g**), pointing towards an inefficient recruitment of DRP1 to mitochondria. Indeed, the co-localization of DRP1 with TOM20 was decreased upon the KD of RAB24 (**Fig. 21h-i**). Intriguingly, RAB24 has previously been shown to be an interactor with FIS1¹³⁸. To test this hypothesis, I send liver samples to Julia Jülg to perform a pull-down experiment. Strikingly, the pull-down with GST-tagged RAB24 compared to RAB3A as control, confirmed this by showing a specific interaction of RAB24 and FIS1

but not DRP1 (**Fig. 22d**). Altogether, these data suggest that RAB24 directly interacts with FIS1 and thereby regulates mitochondrial fission.

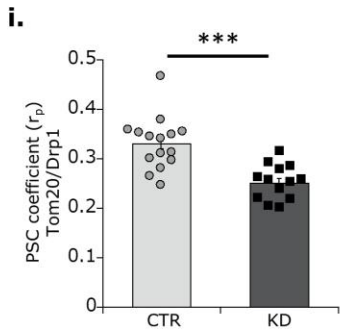
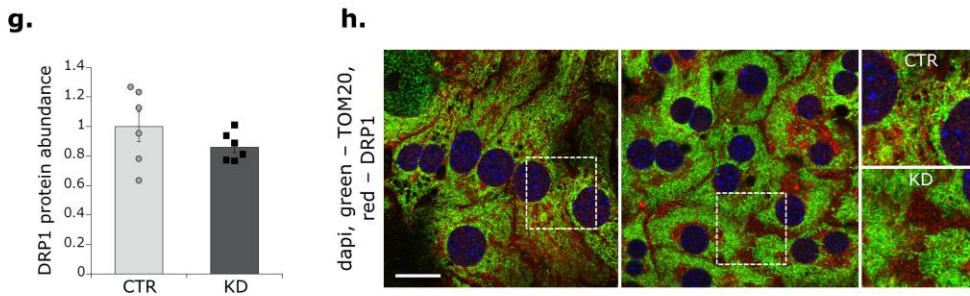
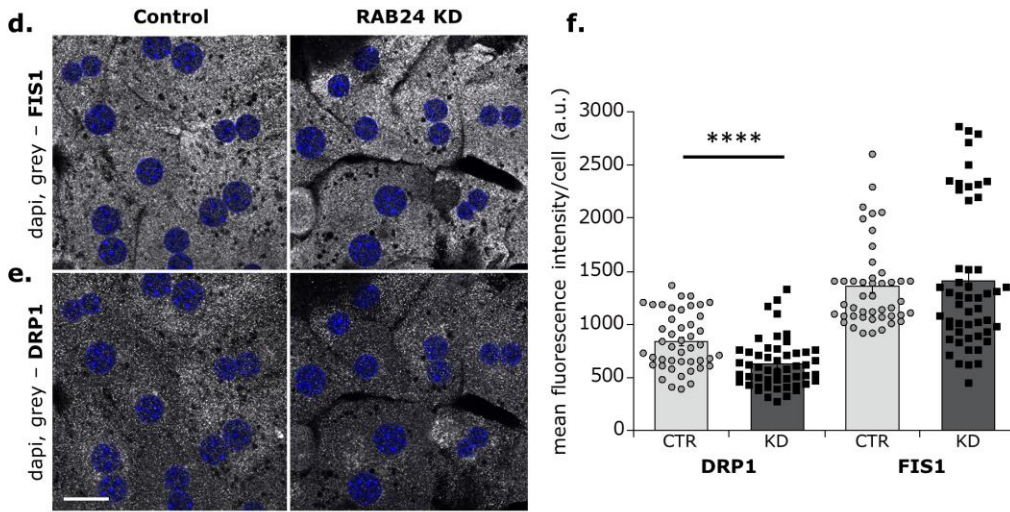
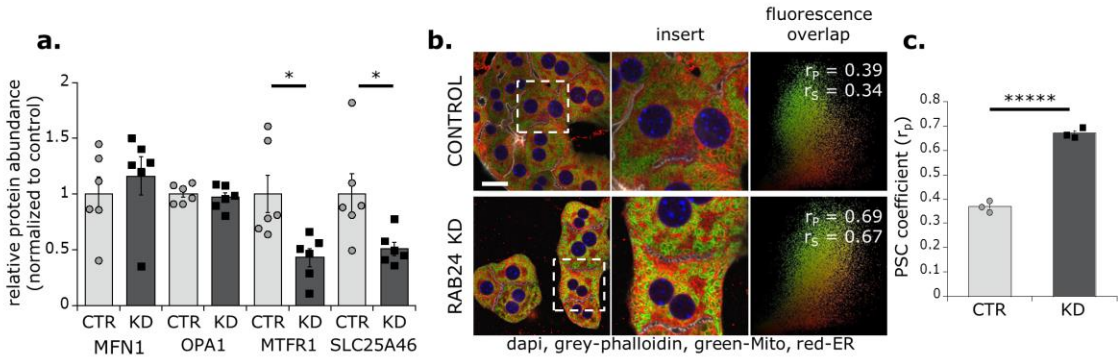


Figure 21: RAB24 KD lead to a decrease in DRP1-TOM20 co-localization.

(a) Protein abundance of fusion and fission regulators from the proteomics analysis. (b) Representative single section confocal images of primary hepatocytes in collagen sandwich stained for dapi (blue), phalloidin (grey), TOM20 (green) and KDEL (red). Higher zoom indicated with white box insert for better visualization. Person's and Spearman's correlation of the overlap between the green and red channel and quantification of thereof in (c). Representative single section confocal images of primary hepatocytes stained with dapi (blue), FIS1 (a) and DRP1 (d) (grey) and quantification in (f). (g) Protein abundance of DRP1 by proteomics in mouse liver. (h) Representative single section confocal images of primary hepatocytes stained with dapi (blue), TOM20 (green) and DRP1 (red). Person's and Spearman's correlation for the overlap between the green and red channel (i). Measured after 3 days of RAB24 KD (40 nM) in primary hepatocytes (mean +/- SEM). Scale bar 20 μ m. Proteomics (a & g) measured after 6 days of KD of RAB24 with LNPs (0.5mg/kg) (N=6 animals per condition). P-value: two-tailed paired Student's *t*-test.

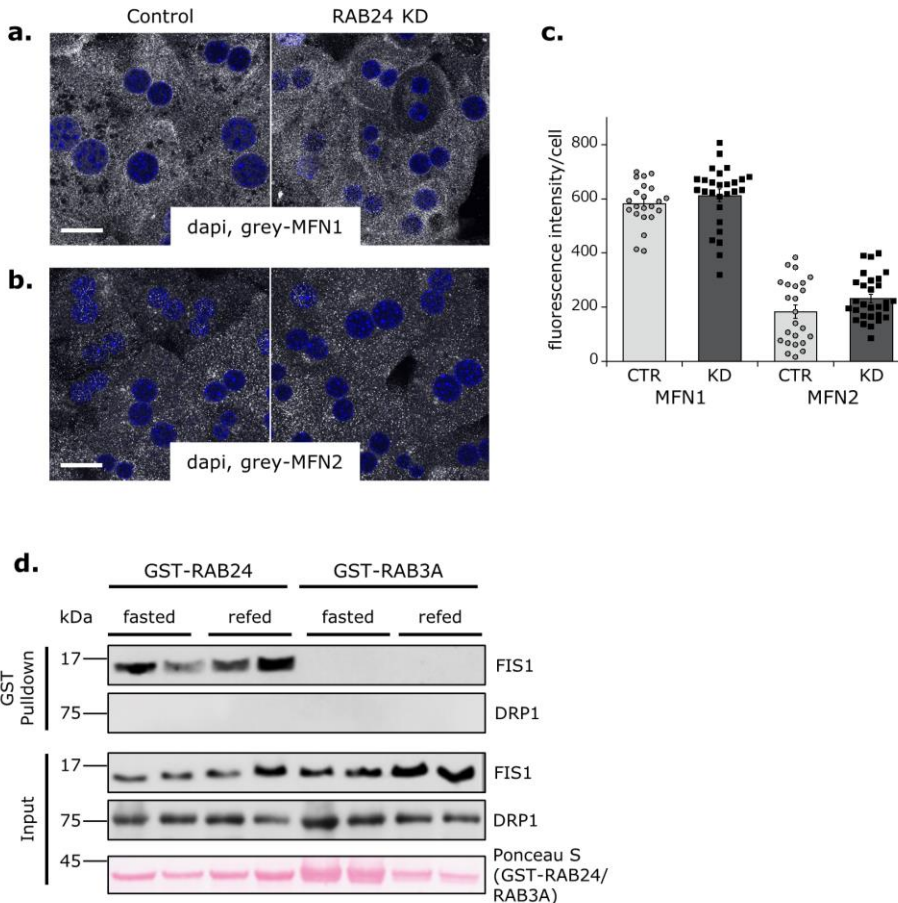


Figure 22: RAB24 KD interacts with the fission machinery.

(a, b) Representative single section confocal images of primary hepatocytes stained for Dapi (blue), MFN1 (a) and MFN2 (b) (grey) and quantification in (c). Scale bar = 20 μ m. Measured after 3 days of RAB24 KD (40 nM) in primary hepatocytes (mean +/- SEM). (d) Pull-down assay for RAB24 and RAB3A as control with FIS1 and DRP1 in mice fasted for 12 h or fasted and refed for 2h. P-value: two-tailed paired Student's *t*-test.

If the interaction of RAB24 and FIS1 was crucial for mitochondrial connectivity and function, a reduction of FIS1 (comparable to the reduction in FIS1 caused by RAB24 KD) should lead to a similar phenotype as observed under RAB24 KD. Decreasing FIS1 expression *in vitro* by 30% (**Fig. 23a**) caused an increase in OCR in basal conditions, ATP production and maximal respiration capacity (**Fig. 23b-e**). In accordance to the RAB24 KD, FIS1 reduction caused an increase in both TOM20 levels and mitochondrial connectivity (**Fig. 23f-j**) underlining the similarities of the phenotypes. Overall, these data indicate that RAB24 directly interacts with FIS1 and therefore initiates mitochondrial fission. Furthermore, hepatic depletion of RAB24 increases mitochondrial connectivity and functions which leads to improvements of whole body metabolic health.

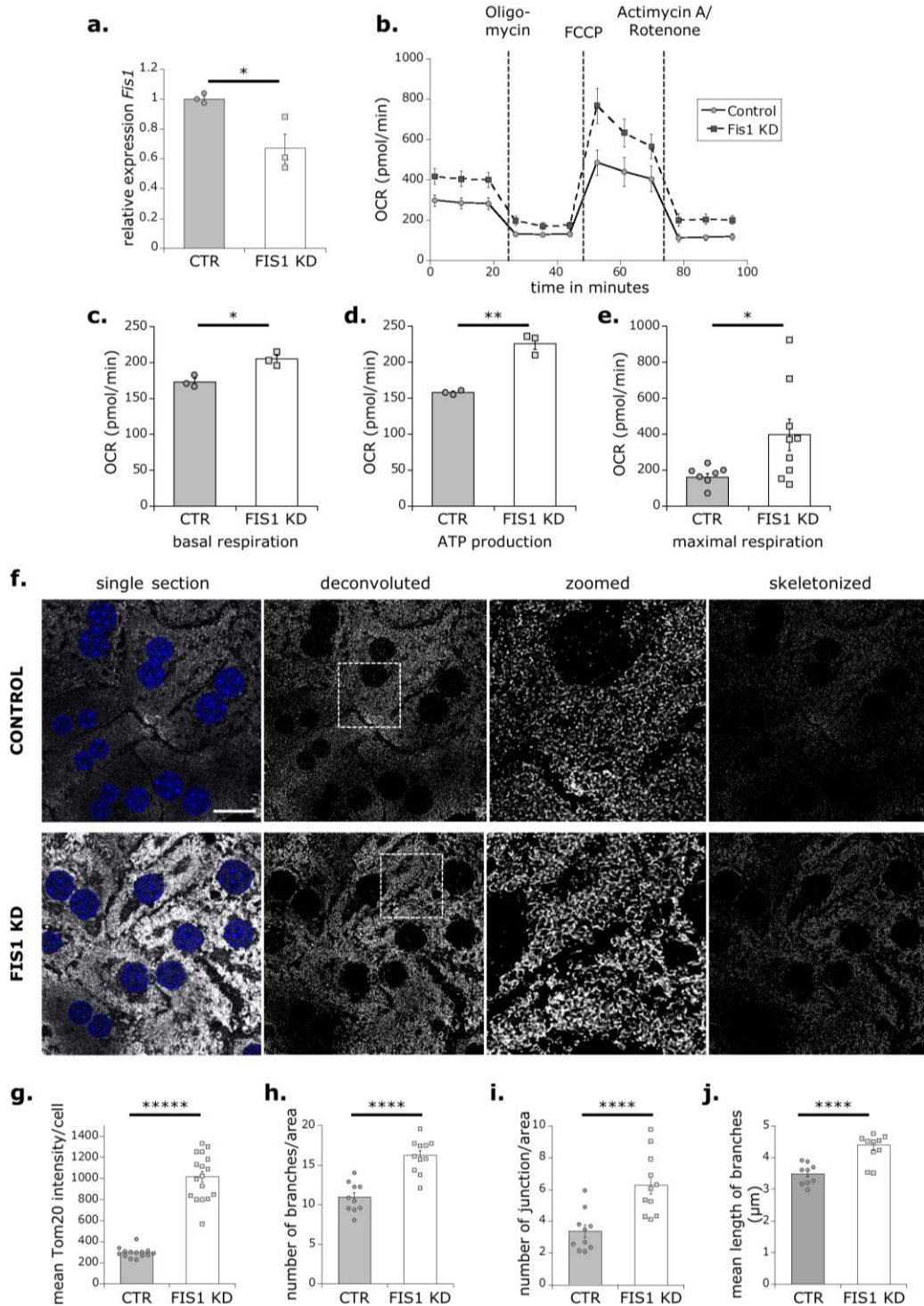


Figure 23: FIS1 KD mimicked the RAB24 KD phenotype.

(a) Relative mRNA expression of *Fis1* in primary hepatocytes after FIS1 KD. (b) Oxygen consumption rate (OCR) in primary hepatocytes and corresponding metabolic rates (c-e) after 3 days of KD (N=10 wells per condition). (f) Representative single section confocal images of primary hepatocytes stained with dapi (blue) and TOM20 (grey) deconvoluted, zoomed and skeletonized with Fiji. (g-j) Quantification of TOM20 (mean intensity per cell, number of branches, number of junctions per area and mean length of

the branches of (f). Scale bar 20 μ m. All measured after 3 days of FIS1 KD (0.1 nM). (mean \pm SEM). P-value: two-tailed paired Student's *t*-test.

2.11. Reduction of RAB24 ameliorate the metabolic phenotype caused by HFD

To investigate a potential therapeutic role for RAB24 in metabolic diseases, I put mice on a high fat diet (HFD). As expected, mice on HFD gained weight and showed an increase in blood glucose levels compared to mice on a low fat diet (LFD) (**Fig. 24a, b**). In agreement with the human patients (**Fig. 8a, b**), the mice on HFD exhibited an induction in *Rab24* mRNA levels (**Fig. 24c**). After 13 weeks of HFD, I performed a liver specific reduction for two weeks while continuing the diet. An 80% reduction in protein levels of RAB24 didn't affect body weight but strikingly, decreased serum triglyceride levels, as well as serum levels of total cholesterol, LDL and ApoB (**Fig. 24d-i**). Strikingly, the decrease in RAB24 levels led to a tremendous improvement of serum ALT levels, a marker for liver damage (**Fig. 24j**), and a great reduction in hepatic lipid content (lipid analysis done by Annette Feuchtinger) (**Fig. 24k-m** and **Fig. 25a-d**). In accordance with the KD in wild type mice (**Fig. 9d**), RAB24 KD mice on HFD showed a decrease in liver/body weight ratio (**Fig. 25e**). In addition to the improved lipid parameters, the KD in HFD mice led to a decrease in fasting blood glucose levels ($p=0.07$) (**Fig. 25f**) and an improvement of glucose clearance after 4 weeks of RAB24 KD (**Fig. 25g, h**), highlighting the beneficial effect of reduced RAB24 levels in the liver for systemic metabolic health.

Intriguingly, the amelioration of the HFD phenotype was associated with an increase in mitochondrial mass and connectivity, as seen in liver sections and IF staining of TOM20 upon KD of RAB24 KD (**Fig. 25i, j** & **Fig. 20e-h**). Moreover, fatty acid treatment (oleate and palmitate) for 3 days, led to lipid droplet formation, visualized with perilipin 2 (PLIN2) staining in primary hepatocytes that was strongly reduced upon RAB24 KD (**Fig. 25l**). Strikingly, primary hepatocytes treated with fatty acids displayed an increase in OCR and its metabolic rates upon RAB24 KD (**Fig. 25k, m**), demonstrating

the beneficial effect of RAB24 reduction upon HFD and fatty acid treatment and emphasizing a potential therapeutic role of RAB24 in the treatment of metabolic diseases.

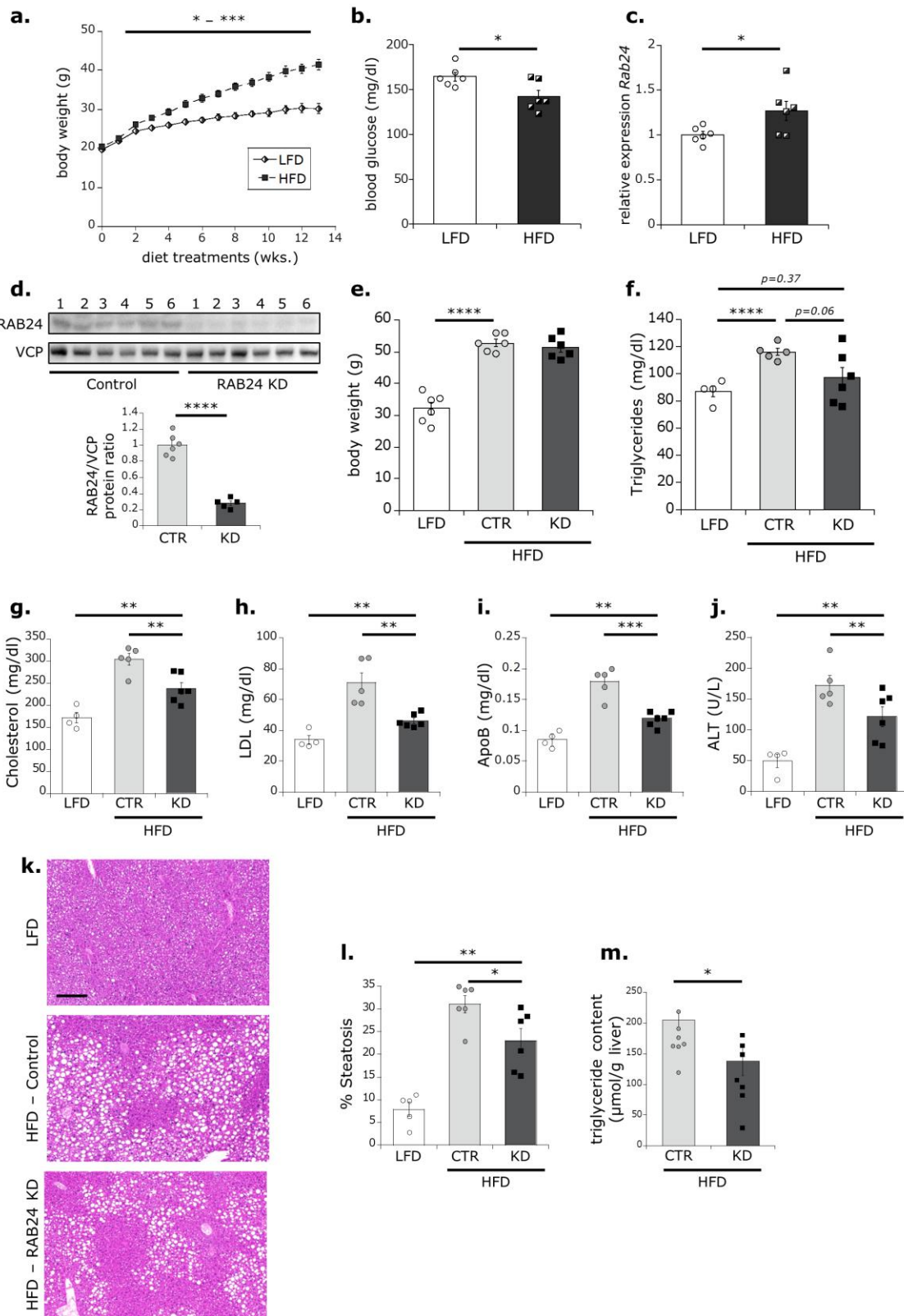


Figure 24: Hepatic RAB24 KD improved serum lipid parameters and liver steatosis in HFD mice.

(a) Body weight change for 13 weeks of HFD treatment. (b) Blood levels (fed) and relative mRNA expression of *Rab24* (c) in the liver after 13 weeks of HFD treatment. (d) Western blot and quantification from liver lysates of mice after control or RAB24 KD. Body weight (e) and serum triglyceride levels (f) after RAB24 KD. Serum levels for total cholesterol (g), LDL (h), ApoB (i) and ALT (j). (k) Hepatic lipid accumulation in liver sections of LFD control, HFD control and HFD RAB24 KD (% steatosis) (l). Scale bar 200 μ m. (m) Liver triglyceride content of HFD control and HFD RAB24 KD mice. P-value: two-tailed paired Student's *t*-test. All animals received 15 weeks of high fat diet (HFD) and were treated with control or RAB24 LNPs for 2 weeks with a weekly injection of LNPs (0.5mg/kg) (mean \pm SEM, N=6 animals per condition)

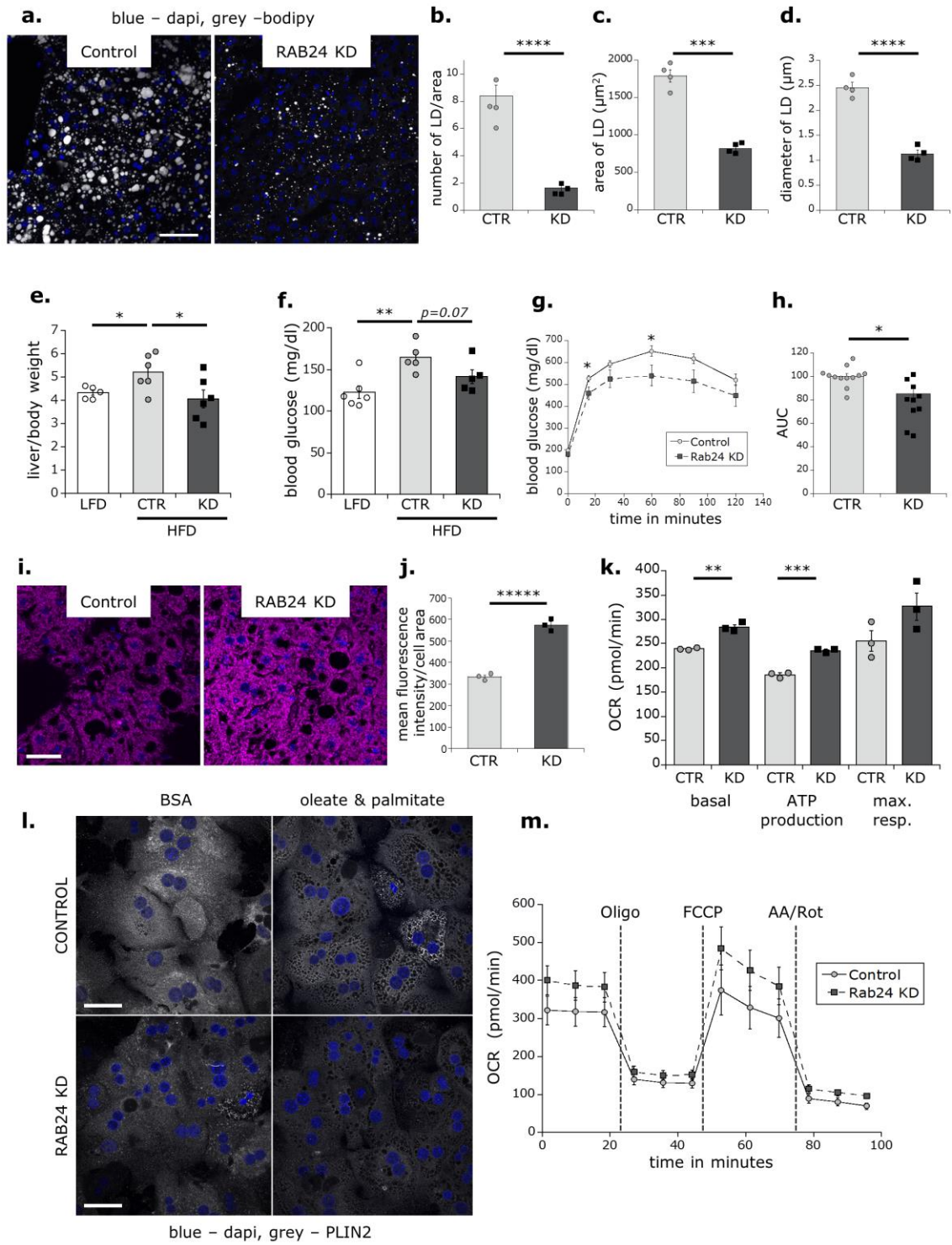


Figure 25: Reduction of RAB24 in the livers of HFD mice improved glucose clearance.

(a) Representative single section confocal images of liver slices of control or RAB24 KD labeled with (3.8 μ M) Bodipy and quantification for number of lipid droplets (b), area of lipid droplets (c) and diameter of lipid droplets (d). Scale bar = 60 μ m. (e) Liver/body weight ratio of LFD control, HFD control and HFD RAB24 KD mice. All measured after 14 days of KD with LNPs (weekly injection; 0.5 mg/kg) and 6 h starvation in 15-week HFD mice (mean \pm -SEM, N=6 animals per condition). Fasted blood glucose levels (f) and ipGTT (2 g/kg) (g) and its AUC (area under the curve) (h) after 4 weeks of RAB24 KD with (weekly injection; 0.5 mg/kg) after 17 weeks of HFD. (mean \pm - SEM, N=6 animals per condition). (i) Representative confocal images (merge of 3 sections, maximal projection) of liver from 15-week HFD mice stained for dapi (blue) and TOM20 (magenta) and quantification in (j). Scale bar 20 μ m. (k) OCR metabolic rates associated with (m) upon RAB24 KD after oleate and palmitate treatment (N=5 wells per condition) after 3 days of KD (40 nM) in primary hepatocytes (mean \pm - SEM). (l) Representative single section confocal images of primary hepatocytes treated oleate and palmitate for 3 days and stained for dapi (blue) and PLIN2 (grey). Scale bar = 20 μ m. (m) OCR upon RAB24 KD after oleate and palmitate treatment (N=5 wells per condition). All measured after 3 days of RAB24 KD (40 nM) in primary hepatocytes (mean \pm - SEM). P-value: two-tailed paired Student's *t*-test.

2.12. KD of RAB24 in a NASH mouse model improves liver steatosis and inflammation

In agreement with the upregulated *RAB24* expression in NASH patients (**Fig. 8b**), *Rab24* expression was also increased in mice under a methionine-reduced, choline-deficient diet (MCD) combined with a HFD (MCD-HFD)¹³⁹ (**Fig. 26a**). Mice fed a MCD-HFD rapidly develop liver steatosis, inflammation and fibrosis accompanied by weight loss¹³⁹. Strikingly a 60% reduction in RAB24 mRNA levels (**Fig. 26a**) extenuated the severe weight loss and blood glucose reduction of the MCD-HFD model (**Fig. 26b, c**) and led to a reduction in the liver/body weight ratio, which is increased in the model (**Fig. 26d**). Intriguingly, the RAB24 KD in MCD-HFD mice decreased liver steatosis (**Fig. 26e-f**)(assay performed by Annette Feuchtinger), triglyceride amount (**Fig. 26g**) and furthermore, improved ALT levels (**Fig. 26f**), illustrating an amelioration of the severe liver damage in the model. Strikingly, *Acta2* (encoding alpha-smooth muscle actin, a marker of activated hepatic stellate cells) and *Adgre1* (encoding F4/80, a marker of murine macrophages), both markers of NASH induction were significantly downregulated after the KD of RAB24 (**Fig. 26i, j**). Altogether, these data display the reduction of hepatic RAB24 as a potential therapeutic method in the treatment of NASH and further highlight the role of RAB24 in the development of metabolic diseases.

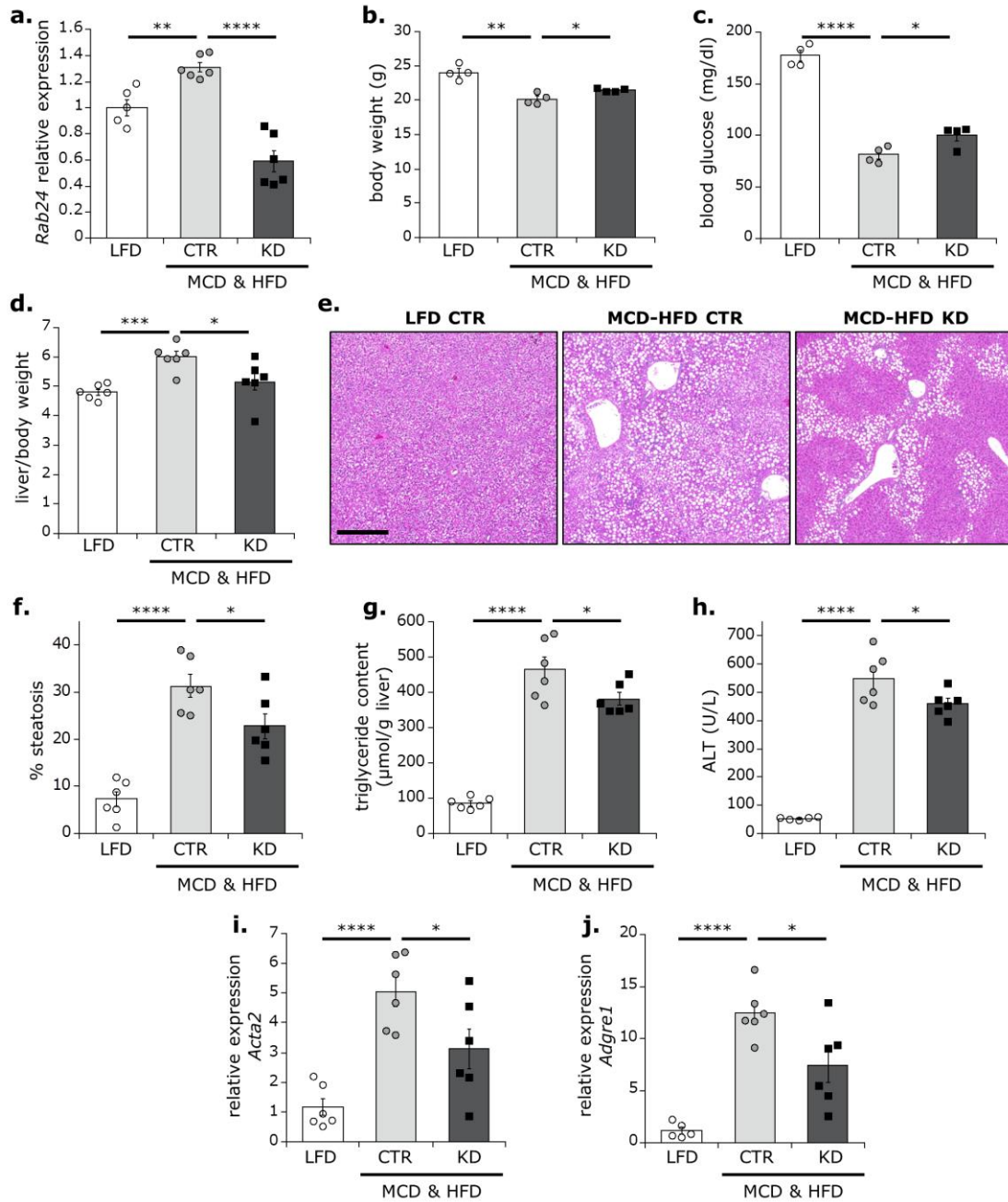


Figure 26: RAB24 KD ameliorated a NASH mouse model.

(a) Relative hepatic mRNA expression of *Rab24* of LFD control, MCD-HFD control and MCD-HFD RAB24 KD mice. (b) Body weight, (c) blood glucose, (d) liver/body weight ratio, H&E staining (e) and quantification of lipid accumulation in the liver (% steatosis) (f) of LFD control, MCD-HFD control and MCD-HFD RAB24 KD livers. Scale bar 500 μ m. (g) Liver triglyceride content, serum ALT levels (h) and relative he-

patic mRNA expression of NASH markers (i, j) of LFD control, MCD-HFD control and MCD-HFD RAB24 KD mice. All measured after 4 weeks of MCD-HFD diet and simultaneous KD (weekly LNP injection; 0.5 mg/kg) and 6 h starvation. (mean +/- SEM, N=4-6 animals per condition). P-value: two-tailed paired Student's *t*-test.

3. Discussion

Although this thesis could show that all of the candidates have a regulatory role in metabolism or are altered in the state of a metabolic disease, for various reasons not all of the candidates were applicable for further studies.

3.1. The elevated *SGIP1* expression might originate from a different cell type other than hepatocytes

A SNP of *SGIP1* was shown to be associated with fat mass in humans and its intracerebroventricular KD was shown to lead to weight loss in rats^{92,141}. Furthermore, *SGIP1* expression was highly upregulated in the livers of NASH patients. However, *Sgip1* expression could not be detected in primary mouse hepatocytes. So the beneficial effect of loss of *SGIP1* is possibly derived from another organ. Previous studies conducted loss of function experiments in the brain where *SGIP1* seems to play an important role for food intake⁹². Nevertheless, an upregulation of *SGIP1* in livers of NASH patients was observed. NASH is characterized by hepatic steatosis and inflammation. Lipotoxicity induces oxidative stress and ER stress that seem to be essential factors for hepatic injury. This leads to the infiltration of macrophages and other components of the immune response system¹⁴². So possibly, the increased *SGIP1* expression in the liver of NASH patients could originate from these immune cells. Further studies would be necessary to identify the origin and the role of *SGIP1* in these cells.

3.2. Diverging effects of *in vitro* and *in vivo* experiments in CHMP4C KD

An increase of *CHMP4C* expression was observed in the livers of NASH patients and *db/db* mice. The potential involvement of CHMP4C in gluconeogenesis was investigated and the *in vitro* KD of CHMP4C lead to an increase in G6PASE expression levels but did not impact glucose output. Moreover, the liver specific *in vivo* KD didn't show any changes in whole body glucose homeostasis. A possible reason for the lacking change in glucose output, despite the increase in G6PASE, could be the normal expression of PCK1. As they are both rate limiting enzymes of the gluconeogenic pathway, one could speculate, that the increase of only one of them might not be sufficient to elevate glucose secretion. Another possibility could be a simultaneous re-uptake of the secreted glucose. There was no increase in glycolysis, so an accumulation of glucose or glycogen in the liver would be measurements to test this hypothesis in further experiments.

Although *CHMP4C* was found to be upregulated in NASH patients and *db/db* mice, the *in vivo* KD didn't affect whole body glucose homeostasis. Possibly the increase in expression is not cause but consequence of the disease. As CHMP4C is part of the ESCRT III complex, the KD of only one component of the complex might not be sufficient to get an effect, as other parts of the complex might substitute for the loss. However, the whole body KO exhibit a deterioration in glucose clearance, showing that the loss of CHMP4C alone, does influence whole body homeostasis but maybe acts on another organ and not the liver.

3.3. Inconsistency of blood glucose levels upon the *in vivo* KD of RAB3IP

The first *in vivo* RAB3IP KD was followed by an increase in fasting blood glucose levels, while the mice in the second KD developed a decrease in fasting blood glucose. This inconsistency might originate from the different levels of KD, as RAB3IP protein was more reduced in the second KD. The effect might be dose dependent so that worse KD efficacy increase and better KD efficacy decrease blood glucose levels. However, the whole body KO showed impaired glucose clearance which would be in accordance with the first KD and also argue against a dose dependent mechanism. Furthermore, RAB3IP acts as activator for RAB3 that is known to play a role in glucose uptake, so upon KD of RAB3IP, glucose uptake could be defective.

3.4. From mitochondria to whole body glucose homeostasis

The major part of my thesis focused on RAB24, where I unraveled RAB24 as a novel regulator of mitochondria turnover by showing its role in assembling the fission machinery. RAB24 directly interacts with FIS1, thereby ensuring proper recruitment of DRP1 to mitochondrial membranes to initiate mitochondrial fission. Loss of RAB24 leads to reduction in mitochondrial fission resulting in decreased mitophagy and a more connected mitochondrial network with higher respiratory capacities. Simultaneously, RAB24 KD caused an induction of autophagic flux, indicating an increase in energy turnover. RAB24 might mimic the fasting state of mitochondria by reprogramming metabolic function of mitochondria towards more connectivity and respiration.

RAB24 KD displayed a robust phenotype of whole body glucose clearance. This might result from the enhanced FGF21 levels secreted by hepatocytes. An increase in oxidative phosphorylation and a subsequent increase in ROS production were observed. ROS has been shown to induce ER stress¹⁴³, which in turn is known to induce FGF21 secretion¹⁴⁴. However, this seems unlikely, as no decrease in FGF21 secretion was observed in combination with the KD of RAB24 with a Ros inhibitor. Moreover,

ATF4, a transcription factor that is induced by ER stress¹⁴⁵ was not changed upon the KD of RAB24, nor was ER stress investigated via IF.

Fgf21 expression can be directly induced by PPAR α , but can also be activated by the activity of mitochondrial 3-hydroxy-3-methylglutaryl-CoA synthase 2 (HMGCS2), that is likewise regulated by PPAR α ¹⁴⁶. HMGCS2 is a rate limiting enzyme in ketone body synthesis¹⁴⁷. Ketone bodies comprise acetoacetate, acetone and d- β -hydroxybutyrate and are mainly produced in mitochondria of the liver which is accompanied by the generation of NAD⁺¹⁴⁸. Sirtuin1 (SIRT1) is a NAD⁺-dependent protein deacetylase is known as a regulator of energy homeostasis¹⁴⁹. SIRT1 has been shown to regulate *Fgf21* expression through *Ppara* induction¹⁵⁰. However, one study shows a PPAR α independent, yet unknown, effect of HMGCS2 on SIRT1 and FGF21¹⁴⁶. They hypothesize that under certain circumstances HMGCS2 activity could modulate cytosolic NAD⁺ generation through acetoacetate production and so regulate SIRT1 activity, leading to induced *Fgf21* expression. No increase in *Ppara* expression was observed, however, HMGCS2 was upregulated in our proteomics analysis. Presumably, the increase in mitochondrial mass, through the inhibition of fission induced mitophagy, could result in increased levels of HMGCS2. This in turn, could lead to the, yet unexplored, SIRT1 dependent, PPAR α independent secretion of FGF21 that causes the improvement of whole body glucose tolerance in the KD of RAB24.

3.5. The role of RAB24 in NASH

Mitochondrial dynamics are associated with the progression of metabolic diseases. In the progression of NAFLD, patients show an increase of mitochondrial respiration, which is thought to serve as a protective function. In contrast, late stages of NASH show a dramatic decrease in mitochondrial function¹¹⁷. *RAB24* was found to be upregulated in obese patients and patients suffering from fatty liver disease and NASH. The progression of the severity of fatty liver disease seems to go hand in hand with the increasing *RAB24* expression in the development of the disease. As depletion of RAB24 seems to

be beneficial for mice on a HFD and MCD, the determination of cause and consequence needs to be addressed.

Interestingly, *Atg7* is found downregulated in *ob/ob* and HFD mice⁶⁹. The progression of obesity is accompanied by the storage of excess lipids and glucose in the liver. Hence, for protection, enhanced autophagy to remove excess lipids and damaged organelles would be expected. But evidence suggests that the dysregulation of autophagy might be the cause, rather than the consequence of metabolic disease⁶⁹. The depletion of ATG7 is sufficient to cause hepatic lipid accumulation⁵⁵, further supporting the theory of disruption of autophagy as cause of metabolic disturbances. Autophagy is inhibited under feeding conditions, therefore, a constant fed state could cause steady downregulation in protein levels of ATG7 and favor the progression of the disease. One could imagine a similar process happening with RAB24. Mitophagy is induced postprandially, hence, a constant upregulation of RAB24 could lead to a block of autophagy^{69,151} and a decrease in mitochondrial connectivity^{152,153}. This could reduce the capacity to utilize the excess nutrients and so exacerbate the progression of obesity and NASH. Interestingly, it has been shown that reduction of DRP1-mediated fission can improve mitochondrial fitness in diabetes-related complications^{154,155}. Mitophagy can also be initiated by oxidative stress¹⁵⁶ that might originate from the accumulation of damaged mitochondria that overproduce ROS during the worsening of the disease^{117,157}.

3.6. RAB24 in hepatocellular carcinoma

NASH can progress to liver cancer¹⁴. In some studies, autophagy has been shown to suppress tumorigenesis, in other cases tumorigenesis is promoted by autophagic action¹⁵⁸. Autophagy has been found to be upregulated in hypoxic regions of tumors and in RAS-transformed cancer cells^{159–162}. Conversely, P62 deficiency has been found to inhibit the development of lung adenocarcinomas¹⁶³. Furthermore, the accumulation of P62 through inhibition of autophagy promotes oxidative stress and tumor growth¹⁶⁴. Moreover, autophagic deficiency has been shown to promote oxidative

stress that can lead to DNA damage and chromosomal instability and therefore the initiation or progression of cancer¹⁶⁵. Additionally, the loss of autophagy can lead to inflammation and cell death, further increasing the risk of cancer development¹⁶⁶. In the liver, suppression of the autophagy component Beclin1 promotes tumors in Beclin1-/- mice^{167,168}, while liver specific loss of ATG7 only leads to the development of benign hepatomas¹⁶⁹. Furthermore, it has been proposed that in the liver autophagy might be important to suppress tumor initiation¹⁵⁸. Increased RAB24 expression in HCC might result in a block of autophagy, causing or worsening the situation.

The role of RAB24s' role in autophagy is not only interesting for HCC, but also its involvement in mitochondrial dynamics. Dysregulated mitophagy has also been suggested to be important for tumorigenesis and has even been suggested to cause the switch of oxidative phosphorylation to glycolysis, called the Warburg effect, although this hypothesis is still a matter of much debate^{170,171,172}. Mitophagy can induce apoptosis in HCC. Damage-regulated autophagy modulator (DRAM) translocate to mitochondria and induce mitophagy which leads to apoptosis¹⁷³. However, enhanced mitophagy leads to the colocalization and degradation of the tumor suppressor p53, while the inhibition of mitophagy leads to phosphorylation of p53 and its translocation to the nucleus¹⁷⁴. Decreasing RAB24 in HCC might thus be beneficial for p53 activity. Recent data show that DRP1-mediated mitochondrial fission correlates with the infiltration of tumor-associated macrophages (TAMs) into HCC tissues, contributing to HCC progression¹⁷⁵. A reduction of RAB24 might interrupt the recruitment of DRP1 to induce fission and so prevent TAM infiltration. So the downregulation of RAB24 specifically in HCC might be a potential target for treating HCC.

3.7. Regulation of endocytosis and metabolism is reciprocal

This study shows that proteins of the endosomal system can have an influence on whole body glucose and lipid metabolism and could be even used as a therapeutic target for treating metabolic diseases. New evidence shows that this regulation is reciprocal. It has been shown that endocytosis is impaired in hepatocytes of diabetic rats¹⁷⁶.

Recent work in form of a proteomics analysis comparing LFD and HFD mice, demonstrates that members of vesicular trafficking re-localize upon HFD feeding¹⁷⁷. This is further supported by the work of Bahar Najafi. In the context of her PhD thesis, she conducted fasting- refeeding experiments, in which she could show the differential localization of several components of the endosomal system. One example is VPS37A, a component of the ESCRTI complex, which is required for the degradation of ubiquitinated cargo^{178,179}. Najafi could show the recruitment of VPS37A to endosomal compartments upon refeeding. Interestingly, the *in vivo* KD of VPS37A led to an increase in hepatic glucose production, further confirming the reciprocal regulation of components of the endosomal pathway and metabolism¹⁸⁰. These studies further link the mostly separated investigated pathways of endocytosis and metabolism and pave the way for the understanding and treatment of metabolic diseases like NASH and diabetes.

3.8. Future perspectives

Future work might include deeper investigation of how RAB24 KD in the liver leads to increase in FGF21 expression and secretion. This would include the investigation of *Sirt1* expression and activity and the implication of PPAR α in this context. As *Rab24* was increased in HFD and MCD mice and its reduction led to an improvement of the conditions, it might be of interest to investigate the role of RAB24 in HCC, as it is also upregulated in several there. Similar to the mice, *RAB24* was also increased in obese and patients with NAFLD and NASH, so in the far future clinical trials might be possible. The relevance for human conditions could be initiated by the use of human hepatocytes, a technique being established in our lab currently. Future projects might also further investigate the function of the other candidates and their involvement in metabolism (**Fig. 11**).

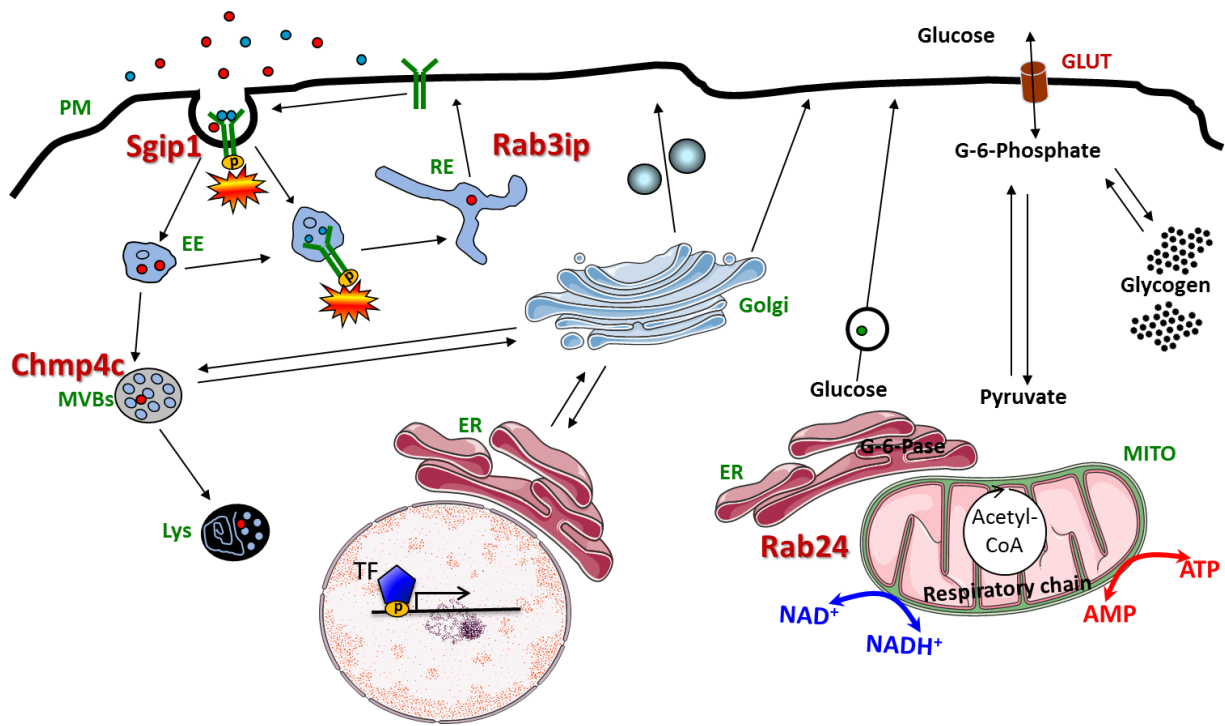


Figure 27: Localization of endosomal candidates in the cell.

SGIP1 is responsible clathrin-dependent endocytosis and found at the PM. CHMP4C is associated with MVB formation. RAB3IP is mediates exocytosis and trans-Golgi network to basolateral membrane trafficking. RAB24 has been linked to mitochondrial dynamics in this study. Adapted from⁷⁶.

4. Material and Methods

4.1. Material

4.1.1. Buffer

EGTA buffer

- 124 ml Glucose solution (9 g/l)
- 20 ml KH-buffer (60 g/l NaCl, 1,75 g/l KCl, 1,6 g/l KH₂PO₄, pH:7,4)
- 20 ml HEPES-buffer (60 g/l HEPES, pH 8,5)
- 30 ml amino acid solution

0,27 g/l L-Alanine, 0,14 g/l L-Aspartic acid, 0,4 g/l Asparagine, 0,27 g/l Citrulline, 0,14 g/l L-Cysteine, 1 g/l L-Histidine, 1 g/l L-Glutamic acid, 1 g/l L-Glycine, 0,4 g/l L-Isoleucine, 0,8 g/l L-Leucine, 1,3 g/l L-Lysine, 0,55 g/l L-Methionine, 0,65 g/l L-Ornithine, 0,55 g/l L-Phenylalanine, 0,55 g/l L-Proline, 0,65 g/l L-Serine, 1,35 g/l L-Threonine, 0,65 g/l L-Tryptophan, 0,55 g/l L-Tyrosine, 0,8 g/l L-Valine; pH 7,6

- 2 ml Glutamine solution (7 g/l)
- 0,8 ml EGTA-LSG. (47,5 g/l in H₂O pH 7,6)

Collagenase buffer

- 155 ml Glucose solution
- 25 ml KH-buffer
- 25 ml HEPES-buffer
- 38 ml amino acid solution
- 10 ml CaCl₂ (19 g/l CaCl₂*2H₂O)

- 2,5 ml Glutamine solution
- 90 g Collagenase

Suspension buffer:

- 124 ml Glucose solution
- 20 ml KH-buffer
- 20 ml HEPES-buffer (pH adjusted to 7,6)
- 30 ml amino acid solution
- 2 ml Glutamine solution
- 1,6 ml CaCl₂- solution
- 0,8 ml MgSO₄- solution (24,6 g/l MgSO₄*7H₂O)
- 400 mg BSA

SDS-Lysisbuffer

- 20 mM Tris pH 7.5
- 150 mM NaCl
- 1 mM EDTA
- 1 mM EGTA
- 1% SDS
- 1% NP40 or 1% Na-deoxycholate

10x SDS running buffer (5 L):

- 150g Tris base
- 720g Glycin
- 50g SDS

10x Blotting buffer (5 L)

- 558.3g Glycin
- 121.6g Tris base

Glucose secretion starvation medium

- 1x DMEM
- 0.5% FBS
- 5mM glucose
- 4 mM glutamine

Glucose secretion stimulation medium

- 1x DMEM
- 4 mM Glutamine
- 2 mM Pyruvate
- 20 mM Lactate
- 100 nM Glucagon
- 100 nM Dexamethasone
- 100 uM Forskolin
- 100 nM Insulin

PBS (1 L):

8 g NaCl, 0,2 g KCl, 1,4 g Na₂HPO₄, 0,24 g KH₂PO₄, pH = 7,4

TNT:

10mM TrisHCl (pH 8,0), 300mM NaCl, 0,1% Tween20, H₂O

PFA Lösung:

40 PFA, 200 µl NaOH (10 M), 10 ml 10x PBS, H₂O

4.1.2. Chemicals and Solutions

PRODUKT	COMPANY
2-dexyglucose	Sigma-Aldrich
Acetic acid	Sigma-Aldrich
Acrylamid mix	Acros organic
Agarose	Biozym
Ammonium persulfate	Applichem
Amplex Red Cholesterol Assay Kit	Invitrogen
Amplex Red Glucose Assay Kit	Invitrogen
Antimycin A	Sigma-Aldrich
Antipain dihydrochloride	Sigma-Aldrich
Amidinophenylmethansulfonylfluorid – Hydrochlorid (APMSF)	Sigma-Aldrich
Aprotinin	Sigma-Aldrich
Asparagine	Sigma-Aldrich
Bovine Serum Albumin (BSA)	Serva
Calcium chloride (CaCl ₂)	Roth
cDNA QuantiTect Reverse Transkription Kit	Qiagen
Chloroform	Roth

Chymostatin	Sigma-Aldrich
Citrulline	Sigma-Aldrich
Collagenase	Sigma-Aldrich
DC Protein Assay Kit	BioRad
Dexametasone	Sigma-Aldrich
Disodium phosphate (Na ₂ HPO ₄)	Roth
DMEM	Biozol
DPBS, phosphatbuffered salin	Life Technologies
ECL	BioRad
EDTA	Roth
EGTA	Sigma-Aldrich
Ethanol	Sigma-Aldrich
Fetal bovine serum (FBS)	Pan Biotech
Forskolin	Sigma-Aldrich
Glucagon	Sigma-Aldrich
Glucose	RL Slaughter
Glutamine	Sigma-Aldrich
Glycine	Sigma-Aldrich
HEPES	Roth
Horse serum	Life Technologies
Interferin	Polyplus Transfection

Invivofectamine	Life Technologies
Isopropanol	Roth
Ketamin	Heinrich Fromme
Lactate	Sigma-Aldrich
Laemmli	Sigma-Aldrich
L-Alanine	Sigma-Aldrich
L-Aspartic acid	Sigma-Aldrich
L-Cysteine	Sigma-Aldrich
Leupeptin	Sigma-Aldrich
L-Glutamic acid	Sigma-Aldrich
L-Glycine	Sigma-Aldrich
L-Histidine	Sigma-Aldrich
L-Isoleucine	Sigma-Aldrich
L-Leucine	Sigma-Aldrich
L-Lysine	Sigma-Aldrich
L-Methionine	Sigma-Aldrich
L-Ornithine	Sigma-Aldrich
L-Phenylalanine	Sigma-Aldrich
L-Proline	Sigma-Aldrich
L-Serine	Sigma-Aldrich
L-Threonine	Sigma-Aldrich

L-Tryptophan	Sigma-Aldrich
L-Tyrosine	Sigma-Aldrich
L-Valine	Sigma-Aldrich
Sigma-Aldrich	PanReac AppliChem
Mowiol	Calbiochem
Nitrocellulose Membrane	GE Healthcare
Nuclease-free Water	Roth
Oligomycin A	Sigma-Aldrich
OptiMEM: Reduced Serum Medium	Life Technologies
Paraformaldehyde (PFA)	Applichem
Penstrep	Life Technologies
Pepstatin A	Sigma-Aldrich
Phosphatase inhibitor cocktail 2& 3	Sigma-Aldrich
Picogreen dsDNA Assay Kit	Life Technologies
Potassium chloride (KCl)	Roth
Potassium phosphate (KH ₂ PO ₄)	Roth
PowerUp SYBR Green Master Mix	Thermo Fisher Scientific
Pyruvate	Sigma-Aldrich
Rat Tail collagen	Roche
RedTaq Ready Mix	Sigma-Aldrich
Rompun	Bela-Pharm

Rotenone	Sigma-Aldrich
Seahorse XF Assay Medium	Seahorse Bioscience
Seahorse XF Calibration Medium	Seahorse Bioscience
siRNA oligos (<i>in vitro</i>)	Dharmacon
siRNA (<i>in vivo</i>)	Ambion
Sodium chloride (NaCl)	Roth
Sodium deoxycholate	Sigma-Aldrich
Sodium hydroxide	Merck
Sodium dodecyl sulfate	Roth
SYBR Safe	Life Technologies
TEMED	Roth
TrisHCl	Roth
Triton X-100	Applichem
TriZol	Life Technologies
Trypan blue	Life Technologies
Tween	Sigma-Aldrich
Whatman paper	Roth
Williams E Medium	Pan Biotech

4.1.3. Machines

Product name	Company
Centrifuge Microfuge 20	Beckman Coulter
HERAcell CO ² 240i incubator	Thermo Fisher Scientific
Icemachine ZBE 110-35	Ziegra
Laser Scanning Confocal Microscope CLSM FluoView FV1200	Olympus
Light Microscope MFA33500	Nikon
NanoDrop 2000	Thermo Fisher Scientific
Plate reader Varioscan Lux	Thermo Fisher Scientific
Real-Time PCR-System QuantStudio™ 6 Flex	Life Technologies
Rotator BV	Labinko
Seahorse analyzer XFe24	Agilent
Shaker WS10	Edmund Bühler
Thermocycler Mastercycler nexus X2e	Eppendorf
Thermoshaker Thermomixer® C	Eppendorf
Ultrasound bath	Sonorex
Ultracentrifuge OPTIMA XPN-80	Beckman Coulter

4.1.4. Programs

BioRad Image Lab

Fiji

Graphpad Prism

Mendeley Citation Program

Microsoft Excel

Microsoft PowerPoint

Microsoft Word

Quantstudio Real-Time PCR Software

4.2. Methods

4.2.1. Human samples

The samples from the following cohort have been obtained by Matthias Blüher. All study protocols have been approved by the Ethics committee of the University of Leipzig (363-10-13122010 and 017-12-230112). All participants gave written informed consent before taking part in the study. In a first cohort, *RAB24* mRNA expression was investigated in liver tissue samples obtained from 40 extensively characterized Caucasian men (n=23) and women (n=17). Patients with a wide range of body mass index (BMI: 22.7-45.6 kg/m²) underwent open abdominal surgery for Roux en Y bypass, sleeve gastrectomy, elective cholecystectomy or explorative laparotomy. Normal glucose tolerance was identified with oral glucose tolerance tests (n=40) Insulin sensitivity

was assessed using the euglycemic-hyperinsulinemic clamp method as described previously¹⁸². Phenotypic characterization has been previously described¹⁸¹. Baseline blood samples were collected after an overnight fast between 8 and 10 am.

The samples from the following cohort have been obtained by Sofiya Gancheva under the supervision of Michael Roden. The second cohort comprised 36 obese individuals (OBE) that underwent bariatric surgery and 8 lean healthy humans (CON) undergoing elective surgery such as herniotomy or cholecystectomy (registered clinical trial NCT01477957), partly previously reported^{50,183}. OBE were further classified into obese without steatosis (NAFL-), with steatosis (NAFL+) and NASH based on liver histology as described in^{50,183}. All participants maintained stable body weight for at least 2 weeks before surgery and were studied using hyperinsulinemic euglycemic clamps for measurement of peripheral and hepatic insulin sensitivity and blood sampling for routine lab parameters⁸¹. Prior to the clamp test participants were asked to refrain from physical activity for 3 days. Volunteers with any history or signs of liver disease other than NAFLD like acute or chronic inflammatory condition, severe renal or heart or lung disease were excluded from participation. During surgery, liver samples for measurement of liver fat content from histology, hepatic mitochondrial function and oxidative stress were obtained as described previously⁸¹. Patients gave written informed consent before being included in the study, which was approved by the Heinrich-Heine-University Düsseldorf Institutional Review Board.

4.2.2. Animals

All animal studies were performed in accordance with German animal welfare legislation and in specific pathogen-free conditions in the animal facility of the Helmholtz Center, Munich, Germany. Protocols were approved by the Institutional Animal Welfare Officer (Tierschutzbeauftragter), and necessary licenses were obtained from the state ethics committee and government of Upper Bavaria (55.2-1-55-2532-49-2017 and 55.2-1-54-2532.0-40-15).

Male C57BL/6N mice purchased from Charles River laboratories were maintained on a 12-h light/12-h dark cycle, in a specific pathogen-free animal facility with a climate-controlled environment, and were fed a regular rodent chow ad libitum. FGF21 mice were obtained from Kerstin Stemmer and Timo Müller^{186,187}. Mice for HFD studies received a HFD starting at the age of 4 weeks. The diet was maintained for 15 or 17 weeks. Diet composition: HFD: 16% Protein, 25% Carbohydrate, 58% Fat in kcal; LFD: 16% Protein, 73% Carbohydrate, 11% Fat in kcal. Mice for studying NASH received a l-amino acid diet with 0.1 % Methionine and no added choline, diet composition: LFD: 18% Protein, 71% Carbohydrate, 10% Fat; MCD 18% Protein, 21% Carbohydrate, 62% Fat in kcal. Diets were purchased from Research diets.

4.2.3. Antibodies and Reagents

Primary antibodies were purchased from the following companies: AKT (9272), pAKT (4060) & Mfn2 (D1E9) (11925) from Cell Signaling Technology (New England Biolabs GmbH Frankfurt/Main, Germany), KDEL (ADI-SPA-827) & Fis1 (ALX-210-1037-0100) from Enzo (Farmingdale, NY), Lamp1 (553792) & Drp1 (611112) from BD Bioscience (San Jose, CA), G6Pase (70R-8595) from Fitzgerald, LC3b (PM036) from MBL (Woburn, MA), Rab24 (ab154824), ATP5A (ab14748), Mfn 1 (ab104274), Opa1 (ab42364) & VCP (ab11433) from Abcam (Cambridge, UK), Tom20 (sc-11415) from Santa Cruz (Dallas, TX). HRP tagged secondary antibodies against mouse or rabbit were purchased from Thermo Fisher Scientific (Waltham, MA) & Sigma-Aldrich Chemie (Munich, Germany). Mito Tracker green and red CM-H2Xros and secondary antibodies labeled with Alexa fluorophores and Alexa-488-phalloidin were obtained from Thermo Fisher Scientific (Waltham, MA) respectively. LDL was purified from human serum and labelled as previously described¹⁸⁴.

4.2.4. Rab24 silencing via lipid nanoparticles (LNP)

LNPs containing siRNA that either target RAB24 or Luciferase as control were manufactured by Axolabs.

Rab24: Sense 5'-gaAuAcGuGGGcAaGAcGAdTsdT-3', Antisense 5'-UCGUCUUGCCcACGuAUUCdTsdt-3';

Luciferase: Sense 5'-cuuAcGcuGAGuAcuucGAdTsdT-3', Antisense 5'-UCGAAGuACUcAGCGuAAGdTsdt-3'.

A, G, U, C: RNA Nucleotide; dA, dG, dT, dC: DNA Nucleotides; a, g, u, c: 2'-O-Methyl-Nucleotide; s: Phosphorothioate

siRNA Design

siRNAs were directed against the full-length Rab24 mRNA and matched to all known mRNA transcript variants available in the NCBI reference sequence database (release 79) and the Ensembl project database (release 85) (NM_009000.3, XM_006517165.3, ENSMUST00000035242). siRNAs were further designed to only match their target mRNA and to have less or equal than 2 mismatches within positions 2–18 of the 19-mer antisense strand sequence to any other genes. siRNA antisense strands lacked a seed region (nucleotides 2–7) identical to a seed region (nucleotides 2–7) of known mouse miRNAs (miRBase, release 21). 12 siRNAs, fulfilling those criteria, were selected for final screening for predicted activity based on analysis with proprietary algorithms.

siRNA synthesis

Using 5'-O-(4,4'-dimethoxytrityl)-3'-O-(2-cyanoethyl-N,N-diisopropyl) phosphoramidite monomers of uridine (U), 4-N-acetylcytidine (CAc), 6-N-benzoyladenine (Abz) and 2-N-isobutylguanosine (GiBu) with 2'-O-t-butyltrimethylsilyl RNA oligonucleotides were synthesized on solid phase made out of controlled pore glass (CPG), protection was according to standard phosphoramidite oligomerization methodology. Employing the corresponding phosphoramidites that carry the same nucleobase protecting

groups as the regular RNA building blocks, 2'-O-methyl-modifications were introduced. The synthesis was executed on K&A DNA/RNA synthesizers.

Phosphoramidites (0.1 M in Acetonitrile) were coupled for 4 min by employing 5-Ethylthio-1H-tetrazole (ETT) as an activator (0.5 M in Acetonitrile). Linkages of phosphorothioate were introduced using 3-((Dimethylamino-methylidene)amino)-3H-1,2,4-dithiazole-3-thione (DDTT). Synthesis of oligonucleotides was "DMT off" and the deprotection was carried out according to previously published procedures¹⁸⁵. If oligonucleotides were crude, they were purified by anion-exchange high-performance liquid chromatography (HPLC) and analyzed via RP HPLC for purity and ESI mass spectrometry for identity.

For the generation of siRNAs from single stranded RNA, equimolar amounts of complementary sense and antisense strands were annealed in a 20 mM NaCl, 4 mM sodium phosphate pH 6.8 buffer (Sigma-Aldrich Taufkirchen, Germany). Further characterization of siRNAs was done by size exclusion HPLC. siRNAs were stored frozen up to usage.

Formulation protocol

DSPC (1,2-distearoyl-3-phosphatidylcholine) was obtained from Avanti Polar Lipids. PEG-c-DOMG (α -[3'-(1,2-dimyristoyl-3-propanoxy)-carboxamide-propyl]- ω -methoxy-polyoxyethylene) was purchased from NOF. Cholesterol was obtained from Sigma-Aldrich. After preparation of 50 mM stock solutions of XL521 lipid, DSPC, cholesterol, and PEG-c-DOMG in ethanol, they were stored at -20°C. Lipids were combined and diluted with ethanol to yield molar ratio of 50:10:38.5:1.5 (XL: DSPC: Cholesterol: PEG-c-DOMG) to a final concentration of 25 mM. The siRNA stocks (10 mg/mL in H₂O) were diluted in 50 mM sodium citrate pH3. By combination of the lipid and the siRNA solution at lipid to siRNA weight ratio of 7:1, the nanoparticle formulations were prepared. To obtain a suspension containing 33% ethanol, the lipid ethanolic solution was rapidly injected into the aqueous siRNA solution with the help of a syringe pump (Harvard Pump 33 Dual Syringe Pump Harvard Apparatus). Using Slide-A-Lyzer cassettes

with a MWCO of 10 kD (RC membrane) the formulations were dialyzed 2 times against phosphate buffered saline (PBS), pH 7.4 at volumes 200-times of the primary product to remove ethanol and achieve buffer exchange. The first dialysis was performed 3h at room temperature, the second one overnight at 4°C. The obtained nanoparticle suspension was filtered with 0.2 µm sterile filter into glass vials that got sealed with a crimp closure.

Formulation characterization

The size and zeta potential of the formulations were tested by using a Zetasizer Nano ZS in 1X PBS and 15 mM PBS, respectively. The concentration of the siRNA in the liposomal formulation was obtained using UV-vis. 100 µL of the diluted formulation (in 1X PBS) was added to 900 µL of a 4:1 (v/v) mixture of methanol and chloroform. With a DU 800 spectrophotometer (Beckman Coulter) the absorbance spectrum of the solution was measured between 230 nm and 330 nm. The difference between the absorbance at 260 nm and the baseline at 330 nm was used to calculate the siRNA concentration in the liposomal formulation, based on the extinction coefficient of the siRNA used in the formulation.

The encapsulation of the siRNA by nanoparticles was calculated with the Quant-iT™ RiboGreen® RNA assay (Invitrogen Corporation). Samples were diluted to 5 µg/mL in TE buffer (10 mM Tris-HCl, 1 mM EDTA, pH 7.5). 50 µL of the diluted sample was mixed with either 50 µL of TE buffer or 50 µL of a 2% Triton X in a polystyrene 96 well plate and incubated for 15 min at 37°C. 100 µL of diluted RiboGreen reagent (1:100 in TE buffer) was added to every well. The fluorescence intensity was measured at the excitation wavelength of ~480 nm and emission wavelength of ~520 nm using a fluorescence plate reader (Wallac Victor 1420 Multilabel Counter; Perkin Elmer). From the sample value, the reagent blank was subtracted and the percentage of siRNA was calculated by dividing the fluorescent intensity of the intact sample (without addition of Triton X-100) by the fluorescent value of the disrupted sample (caused by the addition of Triton X-100).

Transfection

Hepa1-6 cells were provided from ATCC (together with LGC Standards) and then cultured in ATCC-formulated Dulbecco's Modified Eagle's Medium (ATCC together with LGC Standards). The medium was supplemented with 10% fetal calf serum (Ultra-low IgG from Life technologies and 1% Pen/Strep and cells were kept at 37°C with 5% CO₂ in a humidified incubator. Hepa1-6 cells were seeded well in 96-well tissue culture plates at a density of 20000 cells/well and transfected with Lipofectamine2000 (Life technologies) according to manufacturer's instructions. Different doses with final concentrations of 24, 6, 1.5, 0.375, 0.0938, 0.0234, 0.0059, 0.0015, 0.0004, and 0.0001 nM of Rab24 siRNA or controls (with F-Luc, R-Luc or Aha-1) were tested. Four wells per condition were transfected. Cells were lysed 24 h after transfection in 150 µl Lysis Mixture (1 volume lysis mixture, 2 volumes nuclease-free water) and subsequently incubated for 1 h at 53°C. A branched DNA (bDNA) assay was performed according to manufacturer's instructions (Thermo Fisher Scientific) and following 30min incubation in the dark, luminescence was read using 1420 Luminescence Counter (WALLAC VICTOR Light, Perkin Elmer). GAPDH levels were used to normalize each well.

In vivo LNP injections

Mice at the age of eight weeks, 36 weeks old FGF21 KO or mice on HFD for 13 weeks were injected with either PBS or siRNA contained in a LNP formulation (either Rab24 or Luciferase control) in a concentration of 0.5 mg/kg via tail vein injection as described before^{76,86,188,189}. Mice on MCD diet received 4 weekly injections simultaneously to the start of the diet. 5 days post injection metabolic assays were performed. 6 days after the injection mice were killed by cervical dislocation and tissue and serum were harvested and snap frozen in liquid nitrogen. For insulin sensitivity measurements in liver and peripheral tissue, mice were injected with 1 U/kg insulin or PBS after 6 h fasting and were sacrificed 7 min after the injection. Tissues were snap frozen with liquid nitrogen.

4.2.5. Serum Parameters

Serum insulin levels were measured by using the Mouse Insulin ELISA kit (Alpco) according to manufacturer's instructions. For obtaining serum levels of total cholesterol, LDL, Apo-B and ALT, Luciferase control and Rab24 KD injected mice were sacrificed 5 days post siRNA injection with cervical dislocation. Blood was collected and centrifuged 10 min at 10 000 x g. Serum parameters were obtained with the Beckman Coulter (Brea, CA) Serum Analyzer AU480.

4.2.6. Proteomics & Bioinformatics

For proteomics analysis, Luciferase and Rab24 KD mice were sacrificed 5 days post injection after 6 h of starvation and the liver snap frozen in liquid nitrogen. The liver samples were then sent to Natalie Krahmer for proteomics analysis under the supervision of Matthias Mann.

Protein samples (50 µg) were solubilized in lysis buffer (4% sodium deoxycholate (SDC), 100 mM Tris pH 8.5, heated at 95 °C for 5 min then sonicated (Branson probe sonifier output 3-4, 50% duty cycle, 3x 30s). The samples were alkylated and reduced at room temperature for 15 min using 10 mM tris-(2-carboxyethyl)-phosphinehydrochlorid (TCEP) and 40 mM 2-chloroacetamide (CAA) and subsequently digested with LysC and trypsin 1:50 (protein:enzyme) at 37 °C overnight. Previously digested peptides were acidified to 1% TFA (final concentration). The solution was centrifuged and loaded on an activated activated (30% Methanol, 1% TFA) double layer styrenedivinylbenzene–reversed phase sulfonated STAGE tips (SDB-RPS; 3M Empore)¹⁹⁰. STAGE tips got washed with 200 µl 0.2% TFA, then with 200 µl 0.2% TFA and 5% ACN. Elution of the peptides was done with 60 µl SDB-RPS elution buffer (80% ACN, 5% NH₄OH) and used for single shot analysis.

2 µg of peptides were loaded on 50-cm column with a 75 µM inner diameter for MS analysis, packed at 60 °C in-house with 1.9 µM C18 ReproSil particles (Dr. Maisch GmbH). Using a binary buffer system that consists of 0.1% formic acid (buffer A) and 80% ACN in 0.1% formic acid (buffer B), the peptides were separated with reversed-phase chromatography. At a flowrate of 300 nl, peptides were separated on a 120 min gradient (5-30% buffer B over 95 min, 30-60% buffer B over 5 min) on an EASY-nLC 1200 system (Thermo Fisher Scientific). The MS data was obtained by using a data dependent top-15 method consistent of max injection time of 20ms, scan range of 300-1650 TH and an AGC target of 3e6. The Sequencing was done with a higher energy collisional dissociation fragmentation with a target value of 1e5 and a window of 1.4 Th. Survey scans were obtained at 60000 resolution. HCD spectra resolution was 15000 with max ion injection time of 28 ms using an underfill ratio of 20% or 40% and dynamic exclusion on 30 s.

The MS data was processed with the MaxQuant version 1.5.6.4. False-discovery rate (FDR) was set to 0.01 at protein, peptide and modification level. Methionine oxidation (M) and acetylation at the N-terminus were put as variable modifications, while carbamidomethyl (C) was set as fixed modification. For protein analysis, three missed cleavages were allowed, and five for phosphorylation. The functions “Match between runs” and “Label free quantifications (LFQ)” were enabled. Using a target-decoy approach (in revert mode) on the Andromeda search engine that is integrated in the MaxQuant, Proteins and peptides were identified. For the search, the mouse UniProt FASTA database was used, which contained 51210 entries (September 2014). Quantification was done with MaxQuant and bioinformatic analysis was done with Perseus 1.5.4.2. The Annotations were extracted from Gene Ontology (GO), UniProtKB and the Kyoto Encyclopedia of Genes and Genomes (KEGG).

For the proteomics analysis four biological replicates was used for each condition and quantified proteins were filtered for a minimum of three valid values. Values, that were missing, got imputed from a normal distribution with a downshift of 0.3 and a width of 1.8. Statistics were done by performing a Student’s t-test (FDR 0.05) while Fisher’s

exact test, 1D annotation enrichment and hierarchical clustering were done with Perseus. The analysis of the proteomics was performed by Anne Loft.

4.2.7. Pulldown assay

Livers were extracted from mice that were fasted for 12 h or fasted for 12 h and refed for 2 h and sent to Julia Jülg to perform the pulldown assay under the supervision of Christian Behrends. *Escherichia coli* competent cells (Rosetta™(DE)) got transformed using pET-60-DEST™ (Novagen). The expression of GST-Rab3a and GST-Rab24 was induced at an optical density (600 nm) of 0.5 by 1 mM IPTG, afterwards bacteria were incubated at 37°C for 4 h. The bacterial pellets were re-suspended with 20 mM HEPES pH 7.5, 100 mM NaCl, 2 mM MgCl₂, 100 µg/mL lysozyme and incubated at 4°C for 30 min. 0.1 mM PMSF and 1 mM DTT were added and bacteria were lysed by sonicating for 5 min at an amplitude of 50 % with 30 sec sonication and 30 sec break. GST-tagged proteins were batch purified on Glutathione Sepharose 4B (GE Healthcare). Bacterial lysates were incubated with end-over-end rotation at 4°C overnight, on beads (50:1) that were equilibrated with purification buffer (20 mM HEPES pH 7.5, 100 mM NaCl, 2 mM MgCl₂). Loaded beads were washed in purification buffer for five times and the purity of GST-Rab3a and GST-Rab24 was measured using mass spectrometry.

The mouse livers were lysed in RIPA buffer (50 mM Tris/HCl pH 8.0, 150 mM NaCl, 0.1 % SDS, 0.5 % sodium deoxycholate, 1% NP-40) containing protease and phosphatase inhibitors (Roche cOmplete™) using a Omni Bead Ruptor 24 for 20 s at 2 ms speed. Tissue was then filtered through a PDVF membrane (4.5 µm Merck Ultrafree®-CL) and the concentration was set to 5 µg/µL. Nucleotide exchange of GST-Rab3a and GST-Rab24 was performed as described before¹⁹¹. Liver lysates were added to 1 % glycerol and got incubated under rotation on either GST-Rab3a or GST-Rab24 beads at RT for 1 h. beads were washed three times with wash buffer (50 mM Tris/HCl pH 8.0, 150 mM NaCl, 2 mM MgCl₂, 10 µM GMP-PNP or GDP-β-S, containing protease and phosphatase inhibitor). Proteins that were bound to GST-Rab3a or GST-

Rab24 got detected by SDS-PAGE and were afterwards immunoblotted with Fis1 (HPA017430 from Atlas Antibodies) and Drp1 (611112 from BD) antibodies.

4.2.8. Triglyceride concentration

For estimation of triglyceride levels in livers of mice, 5 days post LNP KD, livers were snap frozen in liquid nitrogen and the triglyceride concentration measured with the Triglyceride assay kit from abcam, using the manufacturer's instructions. The triglyceride measurement was performed by Revathi Sekar.

4.2.9. RT-PCR

Human *RAB24* mRNA expression studies

RAB24 expression in humans was estimated by quantitative real-time RT-PCR using Taqman assays in a fluorescent temperature cycler and the detector ABI PRISM 7000 sequence detector (Applied Biosystems). RNA was extracted with TRIzol (Life technologies) and integrity and quantity measured with NanoVue plus Spectrophotometer (GE Healthcare). 1 µg RNA was reverse-transcribed with a reverse transcription kit (Life technologies) and proceeded for qPCR in the QuantStudio 6 Flex Real-Time PCR System (Life Technologies). The following probes were used: *RAB24* (Hs01585710_g1) and 18S rRNA (Hs99999901_s1) as control.

qPCR analysis using SYBRgreen

RNA was extracted from liver tissue or primary hepatocytes with TRIzol and cDNA was reversely transcribed with the SuperScript III reverse transcriptase kit (Life technologies). qPCR was performed in 10 µl of total reaction volume in 1x SYBRgreen (Life technologies), 200 nM of forward and reverse primers (Table 2) and containing 24 ng of total cDNA in the Quantstudio6 (Life Technologies) with the thermal cycling condi-

tions: 50 °C for 2 min; 95 °C for 10 min; 95 °C for 15 s and 60 °C for 1 min (40 Cycles). Quantification was performed using the comparative 2- $\Delta\Delta$ CT Method.

4.2.10. Western blot and Quantification

Samples for western blot analysis were lysed with SDS-lysis buffer (20 mM Tris pH 7.5, 150 mM NaCl, 1 mM EDTA, 1 mM EGTA, 1% SDS, 1% Na-deoxycholate containing Phosstop. 20 μ g of liver lysates or 40 μ g of lysates obtained from cultured primary hepatocytes were run in SDS/PAGE gels (Novex WedgeWell 8-16% Tris-Glycine Mini Gels) (Thermo Fisher Scientific) and were afterwards transferred to nitrocellulose membranes. After blocking for 1 h, membranes were incubated with different antibodies. Using Amersham ECL Prime (Th. Geyer) protein bands were detected with a BioRad Chemidoc MP imaging system and afterwards quantified with either Image Lab (BioRad) or ImageJ.

4.2.11. Histology

Mouse liver pieces were snap frozen in liquid nitrogen 5 days post LNP KD and then were fixed in 4% (w/v) neutrally buffered formalin (Sigma-Aldrich). The prohibitin and H&E staining was performed by Annette Feuchtinger. Liver pieces were then embedded in paraffin (SAV) and got sectioned into 3 μ m slices for immunohistochemistry or H&E staining. Immunohistochemistry was performed with a Discovery XT automated stainer (Ventana Medical Systems) using the primary antibody anti-prohibitin (1:200, Abcam28172) and the secondary antibody Discovery Universal (Ventana Medical Systems). The signal was detected with the Discovery® DAB Map Kit (Ventana Medical Systems) and scanned with AxioScan.Z1 digital slide scanner (Zeiss) equipped with a 20x magnification objective. Using the Definiens Developer XD 2 (Definiens AG) the images were analyzed for mean brown intensity¹⁹².

To perform cryostat sections, liver pieces were thawed in 4% PFA and were then transferred to 30% sucrose for 3 days. Pieces were embedded in OCT and were cut to 5 to 7 μm cryostat sections. The sections were immune stained with antibodies in PBS BSA (3 %) at RT for 2 h with primary antibody and 1 h with secondary antibody. Afterwards, Mowiol was used for mounting on coverslips.

4.2.12. Hepatocyte isolation and transfection

Male C57BL/6N mice in the age of 8-12 weeks were perfused with collagenase to isolate primary hepatocytes¹⁹³. Under anesthesia, mice were cut open and liver was perfused via vena cava first for 10 min with an EGTA-containing buffer, afterwards with a buffer containing collagenase for 10 – 12 min (both buffers on HEPES/KH base). After perfusion, the liver was collected in a buffer containing BSA, filtered through a 100 nm pore size sieve and re-suspended in the buffer after centrifugation. Cells were plated in 24-well plates, pre-coated with collagen, in a density of 200000 cells per well and supplemented with Williams E Medium containing 10% FBS, 5% penicillin/ streptomycin and 100 nM dexamethasone. After 1 h cells were incubated with 40 nM siRNA or 0.1 nM Fis1, Interferin (1.2 μl /well) in Williams E medium for 6 h. After washing with PBS, a second layer of collagen was added to obtain a sandwich culture. Cells were maintained at 5% CO₂ and 37 °C and medium was changed twice a day^{121,194}. HFD studies *in vitro* were performed by conjugating BSA 1:6 with palmitate and oleate and supplementing Williams E medium with 100 μM palmitate and 400 μM oleate.

4.2.13. Electron microscopy

Electron microscopy (EM) was performed by Jerome Gilleron at the CCMA EM Core Facility (Université de Nice Sophia Antipolis, France). Liver pieces or primary hepatocytes were fixed in 2.5% glutaraldehyde (GA) at room temperature overnight. For 1 h livers or cells were post-fixed in potassium ferrocyanide-reduced osmium tetroxide and were then dehydrated with increasing concentrations of ethanol. After incubation

with epon:ethanol (1:2 and 2:1), livers or cells were embedded with epon^{76,118} and sectioned in 70 nm slices with a Leica ultramicrotome. Sections were counter-stained with uranyl acetate and lead citrate and at least 30 images per condition were taken. The number of mitochondria and mitophagic events was counted in every image. Morphological analysis of mitochondria was done with FIJI and contained area, width, height, perimeter and feret's diameter to calculate the aspect ratio (width/ height), form factor ($\text{perimeter}^2/(4\pi\text{Area})$), mitochondria roundness ($4(\text{area}/(\pi\text{width}))$) and mitochondria circularity ($4\pi(\text{area}/\text{perimeter})$)¹⁹⁵.

4.2.14. Immunofluorescence and LDL uptake assay

Cells in sandwich culture were fixed in 4% PFA for 30 min at room temperature, washed twice with PBS, permeabilized for 1 h in 0.1% Triton X-100, blocked in 10% horse serum for 2 h and incubated with primary antibody in 5 % horse serum overnight at 4°C. After washing with TrisHCL (pH 8.0, 10 mM) and NaCl (300 mM) -Tween-Solution (0.1%) (TNT) for 2 h, cells were incubated with secondary antibodies (1:1000) and phalloidin for 5 h at 37 °. Cells were washed with TNT and incubated with for 5 h at 37 °C. Cells were washed twice with PBS, incubated 5 min with DAPI (1:10000) and mounted on glass slides with 0.1 g/ml Mowiol. Monolayer cultured cells were fixed for 15 min in PFA, washed twice with PBS, permeabilized for 10 min in 0.1 % Triton X-100, blocked for 10 min in 10 % horse serum and incubated with primary antibodies in 5 % horse serum for 1 h. After washing 3x with PBS, cells were incubated with secondary antibodies (1:1000) for 1 h. Cells were washed, incubated with DAPI and mounted on glass slides with Mowiol.

To monitor the uptake of LDL, cells were serum starved for 2 h. Dil-LDL (~2.5 µg/ml) was added at several time points to obtain data for a continuous uptake⁷⁶. Cells were washed and fixed in 4% PFA for 30 min⁷⁶. Cells were co-stained with DAPI and mounted with Mowiol.

4.2.15. Confocal microscopy and analysis

IF was analyzed with the Olympus Fluoview 1200 equipped with an Olympus UPlanSApo 60x 1.35 and an UPlanSApo 40x 1.25Sil Oil immersion objective at a resolution of app. 100 $\mu\text{m}/\text{pixel}$ (60x) and 600 nm step size. Individual images were analyzed after background subtraction and a minimum of 30 cells per condition was measured. Particle quantification was performed by including dots with a pixel^2 from 0.1 to 10 and circularity from 0.0 to 1.0. Overall intensity of the particles was divided by the cellular area to obtain the mean dot intensity.

PSC coefficients analysis and statistics

For co-localization studies performed by Yun Kwon, the Pearson and Spearman Correlation coefficients (PSC) were calculated with the PSC co-localization plug-in of ImageJ 1.52e¹⁹⁶. A minimum of three independent images with 10 individual cells and a minimum of 500 signals were used for each analysis. The threshold level for background noise was set to 10 and PSC values were between -1 (negative correlation) and +1 (positive correlation).

Mitochondria 3D Reconstruction and Morphometric Analysis

For 3D reconstruction of the mitochondrial network, designed by Yun Kwon, the images were deconvolved with the point spread function (PSF) generator¹⁹⁷ in FIJI and DeconvolutionLab¹⁹⁸. The PSF algorithm from Born & Wolf 3D Optical model was used for generating the PSF and Z-step was set to 0.6 μm . A 3D deconvolution algorithm from Richardson-Lucy with TV regularization and the generated PSF were applied to the microscope images with DeconvolutionLab. A skeleton of the images was made with the Fiji plugin Skeletonize3D from the deconvolved 2D and 3D binary images (8-bit images) images to determine the mitochondrial network. The network was analyzed with the plugin AnalyzeSkeleton (2D/3D), which tags all pixel/voxels in a skeleton im-

age, counts junctions as well as branches and their length. At least 20 cells per condition were analyzed.

4.2.16. Seahorse assays

Cells were plated in collagen pre-coated plates in a density of 30000 cells per well in a monolayer culture. For *in vitro* assays, siRNA KD was performed after plating and the assay was conducted 2 days after KD, for *in vivo* studies, the assay was performed directly after isolation 5 days post LNP-KD. Oxidative phosphorylation and glycolysis were measured with the Seahorse XFe 24 Analyzer. A mito stress assay was conducted with 2 μ M oligomycin, 1 μ M FCCP and 1 μ M Antimycin A + 1 μ M Rotenone. Glycolysis was measured by injecting 100 mM 2-DG.

4.2.17. Cholesterol, bile acid, lactate and FGF21 Secretion

Primary hepatocytes cultured in a collagen sandwich were serum for 5 h 3 days post siRNA treatment. The amounts of cholesterol, bile acids, lactate and FGF21 were measured using the respective kits Amplex Red Cholesterol Assay Kit from Thermo Fisher, total bile acid kit from Cell Biolabs, Lactate Assay kit from Sigma-Aldrich and the Mouse/Rat FGF-21 Quantikine ELISA Kit from R & D Systems according to manufacturer's instructions. All assays were normalized to total protein levels, obtained with the DC Protein assay kit.

4.2.18. Mitochondrial assays

Primary hepatocytes in sandwich culture were incubated with 200 nM MitoTracker green and 250 nM MitoTracker Red for 45 min 3 days after siRNA treatment *in vitro* or

directly after isolation from KD mice 5 days after LNP KD. MitoTracker fluorescence was normalized to DAPI fluorescence.

Mitophagy was measured by inducing mitochondrial degradation with 20 μ M FCCP or 10 μ M oligomycin for 1 h and staining for total and nuclear DNA (DAPI) to calculate the amount of cytosolic mitochondrial DNA¹²⁶. Accumulation of mitophagic vesicles were measured with the CYTO-ID Autophagy Detection Kit from Enzo after treatment with 20 μ M FCCP with or without 20 μ M Chloroquine for 2 h.

4.2.19. Autophagy flux

Autophagy *in vivo* was determined after 5 days of LNP KD. Mice were either kept at ad libitum feeding, were fasted for 12 h or got a single injection of 100 mg/kg Chloroquine that incubated for 3 h. Livers were snap frozen in liquid nitrogen and western blot analysis was performed for the autophagy markers LC3 and p62. *In vitro* determination of autophagy took place in primary hepatocytes in a sandwich culture 4 days after siRNA KD. Cells received either full medium, were serum and Dex starved for 12 h or were starved and received 20 μ M chloroquine for 3 h. Cells were lysed with SDS buffer for western blots or fixed in 4% PFA for IF.

4.2.20. ATP, Ros & Carbonylation assay

ATP, Ros production and carbonylation of proteins were measured in primary hepatocytes cultured as monolayer in collagen coated 96-well plates 3 days post siRNA treatment according to manufacturer's instructions using the respective kits: CellTiter-Fluor Cell Viability Assay from Promega, DCFDA Cellular ROS Detection Assay Kit and Protein Carbonyl Content Assay Kit from Abcam. All assays were normalized to DAPI fluorescence.

4.2.21. Glucose uptake assay

Glucose uptake was measured in primary hepatocytes cultured as monolayer in collagen coated 96-well plates 3 days post siRNA treatment. Cells were treated with 10 μM 2-NBDG for 1 h in either basal medium or medium supplemented with 2 μM Oligomycin, 1 μM Antimycin + 1 μM Rotenone or 25 mM glucose. 2-NBDG fluorescence was measured and normalized to DAPI fluorescence.

4.2.22. Statistical analyses and data processing

Statistical analysis was done by performing two-tailed, unpaired Student's t-tests. Values for $p < 0.05$ were considered statistically significant. * $p < 0.05$, ** $p < 0.01$, *** $p < 0.001$, **** $p < 0.0001$, ***** $p < 0.00001$. Data are shown as mean \pm SEM.

5. Appendix

Table 2: Primers for RT-PCR

Symbol	Accession number	Name	Forward primer	Reverse primer
Rab24	NM_009000	RAB24, member RAS oncogene family	CATCCAGCAAGA-CAGGCCAAAG	GCTATGATACCGTTCTT-GACCAG
FGF21	NM_020013	fibroblast growth factor 21	GTGTCAAA-GCCTCTAGGTTTCTT	GGTACACATTGTAAC-CGTCCCTC
Fis1	NM_001163243	fission, mitochondrial 1	CAAAGAGGAACAGCGG-GACT	ACAGCCCTCGCACAT-ACTTT
Gck	NM_001287386	glucokinase	TGAGCCG-GATGCAGAAGGA	CTCCCAGGTCTAAGGA-GAGAAA
Pklr	NM_001099779	pyruvate kinase liver and red blood cell	TCAAGGCAGGGATGAACA TTTG	CACGGGTCTG-TAGCTGAGTG
Ppargc1a	NM_008904	Peroxisome proliferative activated receptor, gamma, coactivator 1 alpha	GAAGTGGTGTAGCGAC-CAATC	AATGAGGG-CAATCCGTCTTCA
Ppargc1b	NM_001364996	Peroxisome proliferative activated receptor, gamma, coactivator 1 beta	GGGAAAAGGCCATCGGTG AA	TCACCGAACACCTCAAAGCG
Nrf1	NM_001164226	nuclear respiratory factor 1	ACAAACTCAGGCCAC-CACCA	TGTACCAACCTG-GATGAGCGA
PPAR γ	NM_001127330	peroxisome proliferator activated receptor gamma	TGTGGGGATAAA-GCATCAGGC	CCGGCAGTTAA-GATCACACCTAT
Sdc1	NM_011519	Syndecan 1	GGAGAGGGCTCTGGA-GAACAAG	AATGACACCTCCCAGCAC-TTCC
LRP1	NM_008512	Low density lipoprotein receptor-related protein 1	CGAGAGCCTTTGTGCTG-GATGA	CGGATGTCCTTCTCAATGAGGG
SR-B1	NM_001205082	Scavenger receptor class B type 1	TTTGGAGTGGTAG-TAAAAAGGGC	TGACATCAGGGACTCAGAGTAG
LDLR	NM_010700	low density lipoprotein receptor	CAAGGTGTGCGACTCCGCC	GGTCCACCAACCGGAA-GCCG
Abca1	NM_013454	ATP-binding cassette, subfamily A (ABC1), mem-	AAAACCGCAGA-CATCCTTCAG	CAT-ACCGAAACTCGTTCACCC

		ber 1		
Glut1	NM_011400	solute carrier family 2 (facilitated glucose transporter), member 1	TCAACACGGCCTTCACTG	CACGATGCTCAGATAGGACATC
Glut2	NM_031197	solute carrier family 2 (facilitated glucose transporter), member 2	TGCTGCTGGA-TAAATTCGCCT	TCAGCAACCATGAAC-CAAGGGA
Gapdh	NM_001289726	Glyceraldehyde 3-phosphate dehydrogenase	CACTGAG-CATCTCCCTCACA	GTGGGTG-CAGCGAACTTTAT
Rplp0	NM_007475	ribosomal protein, large, P0	AGATTCGGGA-TATGCTGTTGGC	TCGGGTCTAGACCAG-TGTTC
Sgip1	NM_001285852	SH3-domain GRB2-like (endophilin) interacting protein 1	AAAGACACTGACTC-TACAGGCTCG	GCTCTGAGCCAGAA-GCAAGA
Chmp4c	NM_025519	charged multivesicular body protein 4C	TCATGACAACATGGAC-CTCAACA	AGCCATCGG-CAAACCTGAACC
Rab3ip	NM_001003950	RAB3A interacting protein	AGCCTGTGCGTTTTAC-GAAG	TTGTGAGCTTCCCTCTGAGCTTT
G6Pase	NM_008061	glucose-6-phosphatase	TCGGAGACTGGTTCAAC-CTC	AG-GTGACAGGGAACCTGCTTTAT
h_RAB24	NM_001031677	RAB24, member RAS oncogene family	AGAG-GAGGGCTGCCAAATCT	TGGCCTGTCTTGCTG-GATGT
h_TBP	NM_001172085	TATA-box binding protein	ACGCCAGCTTCGGAGAG-TTC	CAAACCGCTTGGGATTATATTTCG
h_GAPDH	NM_001256799	Glyceraldehyde 3-phosphate dehydrogenase	TGGCAAATTCCATGG-CACCG	ATCTCGCTCCTGGAA-GATGGTG
h_RPLP0	NM_001002	ribosomal protein lateral stalk subunit P0	TGCTGATGGGCAA-GAACACC	CGGATATGAGGCAGCAG-TTTCTC

6. References

1. Kokil, G. R., Veedu, R. N., Ramm, G. A., Prins, J. B. & Parekh, H. S. Type 2 Diabetes Mellitus : Limitations of Conventional Therapies and Intervention with Nucleic Acid-Based Therapeutics. *Chem. Rev.* (2014). doi:10.1021/cr5002832
2. World Health Organization, W. GLOBAL REPORT ON DIABETES. (2016).
3. International Diabetes Federation, I. About Diabetes. (2017). Available at: <https://www.idf.org/aboutdiabetes/what-is-diabetes/facts-figures.html>.
4. American Diabetes Association, A. Diagnosis and classification of diabetes mellitus. *Diabetes Care* **33**, (2010).
5. Pandey, A., Chawla, S. & Guchhait, P. Critical Review Type-2 Diabetes : Current Understanding and Future Perspectives. *IUBMB* 506–513 (2015). doi:10.1002/iub.1396
6. Wu, Y., Ding, Y., Tanaka, Y. & Zhang, W. Risk Factors Contributing to Type 2 Diabetes and Recent Advances in the Treatment and Prevention. *Int. J. Med. Sci.* **11**, (2014).
7. Firneisz, G. Non-alcoholic fatty liver disease and type 2 diabetes mellitus : The liver disease of our age ? *World J. Gastroenterol.* **20**, 9072–9089 (2014).
8. Bogardus, C., Lillioja, S., Howard, B. V, Reaven, G. & Mott, D. Relationships between insulin secretion, insulin action, and fasting plasma glucose concentration in nondiabetic and noninsulin-dependent diabetic subjects. *J. Clin. Invest.* **74**, 1238–1246 (1984).
9. Kim, S. P., Ellmerer, M., Van Citters, G. W. & Bergman, R. N. Primacy of Hepatic Insulin Resistance in the Development of the Metabolic Syndrome Induced by an Isocaloric Moderate-Fat Diet in the Dog. *Diabetes* **52**, 2453–2460 (2003).
10. Anstee, Q. M., McPherson, S. & Day, C. P. How big a problem is non-alcoholic fatty liver disease ? *BMJ* 1–5 (2011). doi:10.1136/bmj.d3897
11. Williams, C. D. *et al.* Prevalence of Nonalcoholic Fatty Liver Disease and Nonalcoholic Steatohepatitis Among a Largely Middle-Aged Population Utilizing Ultrasound and Liver Biopsy : A Prospective Study. *Gastroenterology* **140**, 124–

- 131 (2011).
12. Bertot, L. C. & Adams, L. A. The natural course of non-alcoholic fatty liver disease. *Int. J. Mol. Sci.* **17**, (2016).
 13. Michelotti, G. A., Machado, M. V. & Diehl, A. M. NAFLD, NASH and liver cancer. *Nat. Rev. Gastroenterol. Hepatol.* **10**, 656–665 (2013).
 14. Sinha, R. Is your liver fat? The rising incidence of fatty liver in adults and kids. (2017). Available at: <https://culturalhealthsolutions.com/is-your-liver-fat/>.
 15. Hofmann, A. The Continuing Importance of Bile Acids in Liver and Intestinal Disease. *Arch Intern Med.* **159**, 2647–2658 (1999).
 16. Marieb, E. & Hoehn, K. *Human Anatomy & Physiology.* (2012).
 17. Stenvall, A., Larsson, E., Strand, S. E. & Jönsson, B. A. A small-scale anatomical dosimetry model of the liver. *Phys. Med. Biol.* **59**, 3353–3371 (2014).
 18. Kmiec, Z. *Cooperation of Liver Cells in Health and Disease.* **161**, (2001).
 19. Wilson, P. W. F. Prediction of Incident Diabetes Mellitus in Middle-aged Adults. *Arch. Intern. Med.* **167**, 1068 (2007).
 20. Vergès, B. Lipid modification in type 2 diabetes: The role of LDL and HDL. *Fundam. Clin. Pharmacol.* **23**, 681–685 (2009).
 21. Samols, E., Marri, G. & Marks, V. Interrelationship of Glucagon , Insulin and Glucose The Insulinogenic Effect of Glucagon. *Diabetes* **15**, 855–866 (1966).
 22. Quesada, I., Tuduri, E., Ripoll, C. & Nadal, Á. Physiology of the pancreatic α -cell and glucagon secretion : role in glucose homeostasis and diabetes. *J. Endocrinol.* **199**, 5–19 (2008).
 23. Joseph, P. K. & Subrahmanyam. Evaluation of the rate-limiting steps in the pathway of glucose metabolism in kidney cortex of normal, diabetic, cortisone-treated and growth hormone-treated rats. *Biochem J.* **128**, 1293–1301 (1972).
 24. Basu, R., Chandramouli, V., Dicke, B., Landau, B. & Rizza, R. Obesity and type 2 diabetes impair insulin induced suppression of glycogenolysis as well as gluconeogenesis. *Diabetes* **54**, 1942–1948 (2005).
 25. De Vos, A. *et al.* Human and rat beta cells differ in glucose transporter but not in glucokinase gene expression. *J Clin Invest.* **96**, 2489–95 (1995).
 26. Kennedy, H. J. *et al.* Glucose Generates Sub-plasma Membrane ATP

- Microdomains in Single Islet beta-Cells. **274**, 13281–13291 (1999).
27. Ashcroft, F. M., Harrison, D. E. & Ashcroft, S. J. H. Glucose induces closure of single potassium channels in isolated rat pancreatic beta-cells. *Nature* **312**, 446–448 (1984).
 28. Cook, D. L. & Hales, C. N. Intracellular ATP directly blocks K⁺ channels in pancreatic B-cells. *Nature* **311**, 271–273 (1984).
 29. Meissner, H. P. & Schmelz, H. Membrane Potential of Beta-Cells in Pancreatic Islets. *Eur. J. Physiol.* **351**, 195–206 (1974).
 30. Saltiel, A. R. & Pessin, J. E. Insulin signaling pathways in time and space. *Trends Cell Biol.* **12**, 65–71 (2002).
 31. Leto, D. & Saltiel, A. R. Regulation of glucose transport by insulin : traffic control of GLUT4. *Nat. Rev. Mol. Cell Biol.* **13**, 383–396 (2012).
 32. Taniguchi, C. M., Emanuelli, B. & Kahn, C. R. Critical nodes in signalling pathways : insights into insulin action. *Mol. Cell Biol.* **7**, 85–96 (2006).
 33. Puigserver, P. *et al.* Insulin-regulated hepatic gluconeogenesis through FOXO1 – PGC-1 a interaction. *Nature* **423**, (2003).
 34. Schilling, M. M., Oeser, J. K., Boustead, J. N., Flemming, B. P. & O'Brian, R. Re-evaluating the FOXO1 – PGC-1a connection. *Nature* **443**, 10–11 (2006).
 35. Rhee, J. *et al.* Regulation of hepatic fasting response by PPAR γ coactivator-1a (PGC-1): Requirement for hepatocyte nuclear factor 4a in gluconeogenesis. *PNAS* (2003).
 36. Bouskila, M., Hirshman, M. F., Jensen, J., Goodyear, L. J. & Sakamoto, K. Insulin promotes glycogen synthesis in the absence of GSK3 phosphorylation in skeletal muscle. *Am. J. Physiol. - Endocrinol. Metab.* 28–35 (2008).
doi:10.1152/ajpendo.00481.2007.
 37. Puigserver, P. *et al.* A cold-inducible coactivator of nuclear receptors linked to adaptive thermogenesis. *Cell* **92**, 829–839 (1998).
 38. Jornayvaz, F. R. & Shulman, G. I. G. Regulation of mitochondrial biogenesis. *Essays Biochem* **47**, 69–84 (2010).
 39. Bergeron, R. *et al.* Chronic activation of AMP kinase results in NRF-1 activation and mitochondrial biogenesis. *Am. J. Physiol. Metab.* **281**, 1340–1346 (2001).

40. Sood, A. *et al.* A Mitofusin-2 – dependent inactivating cleavage of Opa1 links changes in mitochondria cristae and ER contacts in the postprandial liver. *PNAS* (2014). doi:10.1073/pnas.1408061111
41. Gomes, L. C. & Scorrano, L. Mitochondrial morphology in mitophagy and macroautophagy. *Biochim Biophys Acta* **1833**, 205–212 (2013).
42. Gomes, L. C., Benedetto, G. Di & Scorrano, L. During autophagy mitochondria elongate , are spared from degradation and sustain cell viability. *Nat. Cell Biol.* **13**, 589–598 (2011).
43. Jin, S. M. *et al.* Mitochondrial membrane potential regulates PINK1 import and proteolytic destabilization by PARL. *J. Cell Biol.* **191**, 933–942 (2010).
44. Sha, D., Chin, L. S. & Li, L. Phosphorylation of parkin by Parkinson disease-linked kinase PINK1 activates parkin E3 ligase function and NF- κ B signaling. *Hum. Mol. Genet.* **19**, 352–363 (2009).
45. Harper, J. W., Ordureau, A. & Heo, J.-M. Building and decoding ubiquitin chains for mitophagy. *Nat. Rev. Mol. Cell Biol.* **19**, 93–108 (2018).
46. Ni, H. M., Williams, J. A. & Ding, W. X. Mitochondrial dynamics and mitochondrial quality control. *Redox Biol.* **4**, 6–13 (2015).
47. Otera, H. *et al.* Mff is an essential factor for mitochondrial recruitment of Drp1 during mitochondrial fission in mammalian cells. *J. Cell Biol.* **191**, (2010).
48. Losón, O. C., Song, Z., Chen, H. & Chan, D. C. Fis1, MFF, MiD49, and MiD51 mediate recruitment in mitochondrial fission. *Mol. Biol. Cell* **24**, 659–667 (2013).
49. Schrepfer, E. & Scorrano, L. Mitofusins , from Mitochondria to Metabolism. *Mol. Cell* **61**, 683–694 (2016).
50. Koliaki, C. *et al.* Adaptation of Hepatic Mitochondrial Function in Humans with Non-Alcoholic Fatty Liver Is Lost in Steatohepatitis. *Cell Metab.* **21**, 739–746 (2015).
51. Kelley, D. E., He, J., Menshikova, E. V. & Ritov, V. B. Dysfunction of mitochondria in human skeletal muscle in type 2 diabetes. *Diabetes* **51**, 2944–2950 (2002).
52. Mogensen, M. *et al.* Mitochondrial respiration is decreased in skeletal muscle of patients with type 2 diabetes. *Diabetes* **56**, 1592–1599 (2007).
53. Ezaki, J. *et al.* Liver autophagy contributes to the maintenance of blood glucose

- and amino acid levels. *Autophagy* 727–736 (2011). doi:10.4161/auto.7.7.15371
54. Raben, N. *et al.* Suppression of autophagy in skeletal muscle uncovers the accumulation of ubiquitinated proteins and their potential role in muscle damage in Pompe disease. *Hum. Mol. Genet.* **17**, 3897–3908 (2008).
 55. Singh, R. *et al.* Autophagy regulates lipid metabolism. *Nature* **458**, 1131–1135 (2009).
 56. Mortimore, G. E., Hutson, N. J. & Surmacz, C. A. Quantitative correlation between proteolysis and macro- and microautophagy in mouse hepatocytes during starvation and refeeding. *Proc Natl Acad Sci USA* **80**, 2179–2183 (1983).
 57. Madrigal-Matute, J. & Cuervo, A. M. Regulation of Liver Metabolism by Autophagy. *Gastroenterology* **150**, 328–339 (2016).
 58. Dice, J. Peptide sequences that target cytosolic proteins for lysosomal proteolysis. *Trends Biochem. Sci.* **15**, 305–309 (1990).
 59. Kaushik, S. & Cuervo, A. M. Chaperone-mediated autophagy : a unique way to enter the lysosome world. *Trends Cell Biol.* **22**, 407–417 (2012).
 60. Moulis, M. & Vindis, C. Methods for Measuring Autophagy in Mice. *Cells* **1**, 1–14 (2017).
 61. Stolz, A., Ernst, A. & Dikic, I. Cargo recognition and trafficking in selective autophagy. *Nat. Cell Biol.* **16**, 495–501 (2014).
 62. Ravikumar, B., Moreau, K., Jahreiss, L., Puri, C. & Rubinsztein, D. C. Plasma membrane contributes to the formation of pre- autophagosomal structures. *Nat. Cell Biol.* **12**, 747–757 (2010).
 63. Amaya, C., Militello, R. D., Calligaris, S. D. & Colombo, M. I. Rab24 interacts with the Rab7 / Rab interacting lysosomal protein complex to regulate endosomal degradation. *Traffic* **17**, 1181–1196 (2016).
 64. Mizushima, N. Autophagy : process and function. *Genes Dev.* 2861–2873 (2007). doi:10.1101/gad.1599207.eralize
 65. Las, G. & Shirihai, O. The role of autophagy in beta-cell lipotoxicity and type 2 diabetes. *Diabetes Obes Metab* **12**, Suppl 2: 15-19 (2010).
 66. Qian, Q. *et al.* S-nitrosoglutathione reductase dysfunction contributes to obesity-associated hepatic insulin resistance via regulating autophagy. *Diabetes* **67**, 193–

- 207 (2018).
67. Bartolome, A., Guillen, C. & Benito, M. Autophagy plays a protective role in endoplasmic reticulum stress-mediated pancreatic β cell death. *Autophagy* 1757–1768 (2012).
 68. Rodriguez, A. *et al.* Mature-onset obesity and insulin resistance in mice deficient in the signaling adapter p62. *Cell Metab.* **3**, 211–222 (2006).
 69. Yang, L., Li, P., Fu, S., Calay, E. S. & Hotamisligil, G. S. Defective Hepatic Autophagy in Obesity Promotes ER Stress and Causes Insulin Resistance. *Cell Metab.* 467–478 (2010). doi:10.1016/j.cmet.2010.04.005
 70. Tooze, S. A., Abada, A. & Elazar, Z. Endocytosis and Autophagy: Exploitation or Cooperation? *Cold Spring Harb. Perspect. Biol.* **6**, (2014).
 71. Ylä-anttila, P. & Eskelinen, E. Roles for RAB24 in autophagy and disease. *Small GTPases* 1–9 (2017). doi:10.1080/21541248.2017.1317699
 72. Stenmark, H. Rab GTPases as coordinators of vesicle traffic. *Nat. Rev. Mol. Cell Biol.* **10**, 513–525 (2009).
 73. Ortiz-sandoval, C. G. *et al.* Interaction with the effector dynamin-related protein 1 (Drp1) is an ancient function of Rab32 subfamily proteins. *Cell. Logist.* **2799**, (2014).
 74. von Mollard, G. F., Stahl, B., Li, C., Südhof, T. C. & Jahn, R. Rab proteins in regulated exocytosis. *Trends Biochem. Sci.* **19**, 164–168 (1994).
 75. Bhui, T. & Kumar, J. Rab proteins : The key regulators of intracellular vesicle transport. *Experime* **8**, 1–19 (2014).
 76. Zeigerer, A. *et al.* Rab5 is necessary for the biogenesis of the endolysosomal system *in vivo*. *Nature* **485**, 465–470 (2012).
 77. Stenmark, H. Rab GTPases as coordinators of vesicle traffic. *Nat. Rev. Mol. Cell Biol.* **10**, 513–525 (2009).
 78. Cooper, G. *The Cell: A Molecular Approach. 2nd edition. Sunderland (MA): Sinauer Associates.* (2000).
 79. Gerst, J. E. SNAREs and SNARE regulators in membrane fusion and exocytosis. *Cell. Mol. Life Sci.* **55**, 707–734 (1999).
 80. Zeigerer, A., Mcbrayer, M. K. & McGraw, T. E. Insulin Stimulation of GLUT4

- Exocytosis, but Not Its Inhibition of Endocytosis, Is Dependent on RabGAP AS160. *Mol. Biol. Cell* **15**, 4406–4415 (2004).
81. Sano, H. *et al.* Insulin-stimulated Phosphorylation of a Rab GTPase-activating Protein Regulates GLUT4 Translocation. *J. Biol. Chem.* **287**, 14599–14602 (2003).
 82. Miinea, C. P. *et al.* AS160 , the Akt substrate regulating GLUT4 translocation , has a functional Rab GTPase-activating protein domain. *Biochem J.* **391**, 87–93 (2005).
 83. Babbey, C. M. *et al.* Rab10 Regulates Membrane Transport through Early Endosomes of Polarized Madin-Darby Canine Kidney Cells. *Mol Biol Cell.* **17**, 3156–3175 (2006).
 84. Vazirani, R. P. *et al.* Disruption of Adipose Rab10-Dependent Insulin Signaling Causes Hepatic Insulin Resistance. **65**, 1577–1589 (2016).
 85. Miura, T. *et al.* Impairment of insulin-stimulated GLUT4 translocation in skeletal muscle and adipose tissue in the Tsumura Suzuki obese diabetic mouse: a new genetic animal model of type 2 diabetes. *Eur J Endocrinol.* **145**, 785–90 (2001).
 86. Zeigerer, A. *et al.* Regulation of Liver Metabolism by the Endosomal GTPase Rab5. *Cell Rep.* 884–892 (2015). doi:10.1016/j.celrep.2015.04.018
 87. McNally, K. E. & Cullen, P. J. Endosomal Retrieval of Cargo : Retromer Is Not Alone. *Trends Cell Biol.* **28**, 807–822 (2018).
 88. Bartuzi, P. *et al.* CCC- and WASH-mediated endosomal sorting of LDLR is required for normal clearance of circulating LDL. *Nat. Commun.* **7**, (2016).
 89. Hobbs, H. H., Brown, M. S. & Goldstein, J. L. Molecular Genetics of the LDL Receptor Gene in Familial Hypercholesterolemia. *Hum. Mutat.* **1**, 445–466 (1992).
 90. Marais, A. D. Familial Hypercholesterolaemia. *Clin Biochem Rev* **25**, (2004).
 91. Uezu, A. *et al.* SGIP1 α is an endocytic protein that directly interacts with phospholipids and Eps15. *J. Biol. Chem.* **282**, 26481–26489 (2007).
 92. Trevaskis, J. *et al.* SH3-domain GRB2-like (endophilin) interacting protein 1 (SGIP1), a novel neuronal protein that regulates energy balance. *Endocrinology* **146**, 3757–3764 (2005).
 93. Cummings, N. *et al.* Genetic variation in SH3-domain GRB2-like (endophilin)-

- interacting protein 1 has a major impact on fat mass. *Int. J. Obes.* **36**, 201–206 (2012).
94. Katoh, K., Shibata, H., Hatta, K. & Maki, M. CHMP4b is a major binding partner of the ALG-2-interacting protein Alix among the three CHMP4 isoforms. *Arch. Biochem. Biophys.* **421**, 159–165 (2004).
 95. Wollert, T., Wunder, C., Lippincott-schwartz, J. & Hurley, J. H. Membrane scission by the ESCRT-III complex. *Nature* **457**, 172–177 (2009).
 96. Petsalaki, E., Dandoulaki, M. & Zachos, G. Chmp4c is required for stable kinetochore-microtubule attachments. *Chromosoma* **1**, 1–13 (2018).
 97. Carlton, J., Caballe, A., Agromayor, M., Kloc, M. & Martin-Serrano, J. ESCRT-III Governs the Aurora B-Mediated Abscission Checkpoint Through CHMP4C. *Science*. **336**, 220–225 (2012).
 98. Bleck, M. *et al.* Temporal and spatial organization of ESCRT protein recruitment during HIV-1 budding. *Proc. Natl. Acad. Sci.* **111**, 12211–12216 (2014).
 99. Paul D. P. Pharoah, Ya-Yu Tsai, Susan J. Ramus, Catherine M. Phelan, Ellen L. Goode, Kate Lawrenson, Melissa Price, Brooke L. Fridley, Jonathan P. Tyrer, Howard Shen, Rachel Weber, Rod Karevan, Melissa C. Larson, Honglin Song, Daniel C. Tessier, François, T. A. S. GWAS meta-analysis and replication identifies three new susceptibility loci for ovarian cancer. *Nat. Genet.* **45**, 362–370e2 (2013).
 100. Hattula, K., Furuholm, J., Arffman, A. & Peränen, J. A Rab8-specific GDP/GTP Exchange Factor Is Involved in Actin Remodeling and Polarized Membrane Transport. *Mol. Biol. Cell* **13**, 3268–3280 (2002).
 101. Brondyk, W. H. *et al.* Interaction Cloning of Rabin3, a Novel Protein That Associates with the Ras-Like GTPase Rab3A. *Mol. Cell. Biol.* **15**, 1137–1143 (1995).
 102. Cherfils, J. & Zeghouf, M. Regulation of Small GTPases by GEFs, GAPs, and GDIs. *Physiol. Rev.* **93**, 269–309 (2013).
 103. Huber, L. A. *et al.* Rab8, a small GTPase involved in vesicular traffic between the TGN and the basolateral plasma membrane. *J. Cell Biol.* **123**, 35–45 (1993).
 104. Sato, T. *et al.* The Rab8 GTPase regulates apical protein localization in intestinal

- cells. *Nature* **448**, 366–369 (2007).
105. Hur, K. *et al.* Hypomethylation of long interspersed nuclear element-1 (LINE-1) leads to activation of protooncogenes in human colorectal cancer metastasis. *Gut* **63**, 635–646 (2014).
 106. Ren, H., Xu, Z., Guo, W., Deng, Z. & Yu, X. Rab3IP interacts with SSX2 and enhances the invasiveness of gastric cancer cells. *Biochem. Biophys. Res. Commun.* 1–6 (2018). doi:10.1016/j.bbrc.2018.07.016
 107. Erdman, R. A., Shellenberger, K. E., Overmeyer, J. H. & Maltese, W. A. Rab24 Is an Atypical Member of the Rab GTPase Family. *J. Biol. Chem.* **275**, 3848–3856 (2000).
 108. Olkkonen, V. M. *et al.* Molecular cloning and subcellular localization of three GTP-binding proteins of the rab subfamily. *J. Cell Sci.* **1261**, 1249–1261 (1993).
 109. Munafo, D. B. Induction of Autophagy Causes Dramatic Changes in the Subcellular Distribution of GFP-Rab24. *Traffic* 472–482 (2002).
 110. Chen, Z. *et al.* KDM4B-mediated epigenetic silencing of miRNA-615-5p augments RAB24 to facilitate malignancy of hepatoma cells. *Oncotarget* **8**, 17712–17725 (2017).
 111. Agler, C. *et al.* Canine Hereditary Ataxia in Old English Sheepdogs and Gordon Setters Is Associated with a Defect in the Autophagy Gene Encoding RAB24. *PLoS Genet.* **10**, (2014).
 112. Jenum, S. *et al.* Approaching a diagnostic point-of-care test for pediatric tuberculosis through evaluation of immune biomarkers across the clinical disease spectrum. *Sci. Rep.* 1–11 (2016). doi:10.1038/srep18520
 113. Cummings, N. *et al.* Genetic variation in SH3-domain GRB2-like (endophilin)-interacting protein 1 has a major impact on fat mass. *Int. J. Obes.* **36**, 201–206 (2012).
 114. Barthel, A. & Schmolli, D. Novel concepts in insulin regulation of hepatic gluconeogenesis. *Am. J. Physiol. - Endocrinol. Metab.* **285**, E685–E692 (2003).
 115. Seitz, S. *et al.* Hepatic Rab24 controls blood glucose homeostasis via mitochondrial metabolic reprogramming. *Nat. Metab.* (2019).
 116. Rozman, J. Identification of genetic elements in metabolism by high-throughput

- mouse phenotyping. *Nat. Commun.* **9**, (2018).
117. Koliaki, C. *et al.* Adaptation of Hepatic Mitochondrial Function in Humans with Non-Alcoholic Fatty Liver Is Lost in Steatohepatitis. *Cell Metab.* **21**, 739–746 (2015).
 118. Gilleron, J. *et al.* Image-based analysis of lipid nanoparticle-mediated siRNA delivery, intracellular trafficking and endosomal escape. *Nat. Biotechnol.* **31**, 638–646 (2013).
 119. Kharitononkov, A. *et al.* FGF-21 as a novel metabolic regulator. **115**, 1627–1635 (2005).
 120. Markan, K. R., Naber, M. C., Ameka, M. K. & Anderegg, M. D. Circulating FGF21 Is Liver Derived and Enhances Glucose Uptake During Refeeding and Overfeeding. **63**, 4057–4063 (2014).
 121. Zeigerer, A. *et al.* Functional properties of hepatocytes *in vitro* are correlated with cell polarity maintenance. *Exp. Cell Res.* **350**, 242–252 (2017).
 122. Niopek, K. *et al.* A Hepatic GAbp-AMPK Axis Links Inflammatory Signaling to Systemic Vascular Damage. *Cell Rep.* 1422–1434 (2017).
doi:10.1016/j.celrep.2017.07.023
 123. Gomes, L. C. & Scorrano, L. Mitochondrial elongation during autophagy. *Autophagy* 1251–1253 (2011).
 124. Jin, S. M. & Youle, R. J. PINK1- and Parkin- mediated mitophagy at a glance. *J. Cell Sci.* **125**, 795–799 (2012).
 125. Ylä-Anttila, P. *et al.* RAB24 facilitates clearance of autophagic compartments during basal conditions. *Autophagy* **11**, 1833–1848 (2015).
 126. Lazarou, M. *et al.* The ubiquitin kinase PINK1 recruits autophagy receptors to induce mitophagy. *Nature* (2015). doi:10.1038/nature14893
 127. Sun, N. *et al.* Measuring *in vivo* mitophagy. *Mol. Cell* **60**, 685–696 (2015).
 128. Gomes, L. C. & Scorrano, L. High levels of Fis1 , a pro- fission mitochondrial protein , trigger autophagy. *Biochim. Biophys. Acta* **1777**, 860–866 (2008).
 129. Twig, G. *et al.* Fission and selective fusion govern mitochondrial segregation and elimination by autophagy. *EMBO J.* **27**, 433–446 (2008).
 130. Picard, M., White, K. & Turnbull, D. M. Mitochondrial morphology, topology, and

- membrane interactions in skeletal muscle: a quantitative three-dimensional electron microscopy study. *J Appl Physiol* **114**, 161–171 (2013).
131. Pernas, L. & Scorrano, L. Mito-Morphosis : Mitochondrial Fusion , Fission , and Cristae Remodeling as Key Mediators of Cellular Function. *Annu. Rev. Physiol.* (2016). doi:10.1146/annurev-physiol-021115-105011
 132. Tonachini, L. *et al.* Chondrocyte Protein With a Poly-Proline Region (CHPPR) Is a Novel Mitochondrial Protein and Promotes Mitochondrial Fission. *J. Cell. Physiol.* **482**, 470–482 (2004).
 133. Monticone, M. *et al.* The Nuclear Genes Mtf1 and Duf1 Regulate Mitochondrial Dynamic and Cellular Respiration. *J Cell Physiol* 767–776 (2010). doi:10.1002/jcp.22279
 134. Abrams, A. J. *et al.* Mutations in SLC25A46, encoding a UGO1-like protein, cause an optic atrophy spectrum disorder. *Nat. Genet.* **47**, 926–932 (2015).
 135. Friedman, J. R. *et al.* ER tubules mark sites of mitochondrial division. *Science.* **334**, 358–362 (2011).
 136. Korobova, F., Ramabhadran, V. & Higgs, H. N. An actin-dependent step in mitochondrial fission mediated by the ER-associated formin INF2. *Science.* **339**, 1–9 (2013).
 137. Smirnova, E., Griparic, L., Shurland, D. & Blik, A. M. Van Der. Dynamin-related Protein Drp1 Is Required for Mitochondrial Division in Mammalian Cells. *Mol. Biol. Cell* **12**, 2245–2256 (2001).
 138. BioGRID. Available at: <https://thebiogrid.org/119817/summary/homo-sapiens/rab24.html>.
 139. Matsumoto, M. *et al.* An improved mouse model that rapidly develops fibrosis in non-alcoholic steatohepatitis. *Int J Exp Pathol* **94**, 93–103 (2013).
 140. Itagaki, H., Shimizu, K., Morikawa, S., Ogawa, K. & Ezaki, T. Morphological and functional characterization of non-alcoholic fatty liver disease induced by a methionine-choline-deficient diet in C57BL/6 mice. *Int J Clin Exp Pathol* **6**, 2683–2696 (2013).
 141. Yako, Y. Y. *et al.* Genetic association studies of obesity in Africa: A systematic review. *Obes. Rev.* **16**, 259–272 (2015).

142. Magee, N., Zou, A. & Zhang, Y. Pathogenesis of Nonalcoholic Steatohepatitis : Interactions between Liver Parenchymal and Nonparenchymal Cells. *Biomed Res Int.* **2016**, (2016).
143. Gu, S., Chen, C., Jiang, X. & Zhang, Z. Chemico-Biological Interactions ROS-mediated endoplasmic reticulum stress and mitochondrial dysfunction underlie apoptosis induced by resveratrol and arsenic trioxide in A549 cells. *Chem. Biol. Interact.* **245**, 100–109 (2016).
144. Kim, S. H. *et al.* Fibroblast growth factor 21 participates in adaptation to endoplasmic reticulum stress and attenuates obesity-induced hepatic metabolic stress. *Diabetologia* 809–818 (2015). doi:10.1007/s00125-014-3475-6
145. Schaap, F. G., Kremer, A. E., Lamers, W. H., Jansen, P. L. M. & Gaemers, I. C. Fibroblast growth factor 21 is induced by endoplasmic reticulum stress. *Biochimie* **95**, 692–699 (2013).
146. Vilá-Brau, A., De Sousa-coelho, A. L., Mayordomo, C., Haro, D. & Marrero, P. F. Human HMGCS2 Regulates Mitochondrial Fatty Acid Oxidation and FGF21 Expression in HepG2 Cell Line *. *J. Biol. Chem.* **286**, 20423–20430 (2011).
147. Hegardt, F. G. Mitochondrial 3-hydroxy-3-methylglutaryl-CoA synthase: a control enzyme in ketogenesis. *Biochem. J.* **338**, 569–582 (1999).
148. Jebb, D. & Hiller, M. Recurrent loss of HMGCS2 shows that ketogenesis is not essential for the evolution of large mammalian brains. *Elife* **7**, (2018).
149. Nemoto, S., Fergusson, M. & Finkel, T. Nutrient Availability Regulates SIRT1 Through a Forkhead-Dependent Pathway. *Science.* **306**, 2105–2108 (2004).
150. Purushotham, A. *et al.* Hepatocyte-specific Deletion of SIRT1 Alters Fatty Acid Metabolism and Results in Hepatic Steatosis and Inflammation. *Cell Metab.* **9**, 327–338 (2009).
151. Gonzales-Rodriguez, A. *et al.* Impaired autophagic flux is associated with increased endoplasmic reticulum stress during the development of NAFLD. *Cell Death Dis.* **5**, (2014).
152. Zorzano, A., Liesa, M. & Palacin, M. Role of mitochondrial dynamics proteins in the pathophysiology of obesity and type 2 diabetes. *Int J Biochem Cell Biol* **41**, 1846–1854 (2009).

153. Duraisamy, A. J., Mohammad, G. & Kowluru, R. A. Mitochondrial fusion and maintenance of mitochondrial homeostasis in diabetic retinopathy. *Biochim Biophys Acta Mol Basis Dis* (2019). doi:doi:10.1016/j.bbadis.2019.03.013
154. Ayanga, B. A. *et al.* Dynamin-Related Protein 1 Deficiency Improves Mitochondrial Fitness and Protects against Progression of Diabetic Nephropathy. *J Am Soc Nephrol* 2733–2747 (2016). doi:doi:10.1681/ASN.2015101096
155. Wang, Q. *et al.* Metformin Suppresses Diabetes-Accelerated Atherosclerosis via the Inhibition of Drp1-Mediated Mitochondrial Fission. *Diabetes* **66**, 193–205 (2017).
156. Frank, M. *et al.* Mitophagy is triggered by mild oxidative stress in a mitochondrial fission dependent manner. *Biochim. Biophys. Acta* **1823**, 2297–2310 (2012).
157. Begriche, K., Igoudjil, A., Pessayre, D. & Fromenty, B. Mitochondrial dysfunction in NASH : Causes , consequences and possible means to prevent it. *Mitochondrion* **6**, 1–28 (2006).
158. White, E. The role for autophagy in cancer. *J. Clin. Invest.* **125**, 42–46 (2015).
159. Yang, S. *et al.* Pancreatic cancers require autophagy for tumor growth. *Genes Dev.* 717–729 (2011). doi:10.1101/gad.2016111.pathways
160. Guo, J. Y. *et al.* Activated Ras requires autophagy to maintain oxidative metabolism and tumorigenesis. *Genes Dev.* 460–470 (2011). doi:10.1101/gad.2016311.2007a
161. Lock, R., Roy, S., Kenifi, C. M., Su, J. S. & Salas, E. Autophagy facilitates glycolysis during Ras-mediated oncogenic transformation. *Mol. Cell. Biol.* **22**, (2011).
162. Degenhardt, K. *et al.* Autophagy promotes tumor cell survival and restricts necrosis, inflammation, and tumorigenesis. *Cancer Cell* **10**, 51–64 (2010).
163. Duran, A. *et al.* The Signaling Adaptor p62 Is an Important NF-kB Mediator in Tumorigenesis. *Cancer Cell* **13**, 343–354 (2008).
164. Mathew, R. *et al.* Autophagy suppresses tumorigenesis through elimination of p62. *Cell* **137**, 1062–1075 (2009).
165. Karantza-Wadsworth, V. *et al.* Autophagy mitigates metabolic stress and genome damage in mammary tumorigenesis. *Gen. Comp. Endocrinol.* 1621–1635 (2007).

doi:10.1101/gad.1565707.facts

166. Sun, B. & Karin, M. Inflammation and liver tumorigenesis. *Front. Med.* **7**, 242–254 (2013).
167. Yue, Z., Jin, S., Yang, C., Levine, A. J. & Heintz, N. Beclin 1, an autophagy gene essential for early embryonic development, is a haploinsufficient tumor suppressor. *PNAS* **100**, (2003).
168. Qu, X. *et al.* Promotion of tumorigenesis by heterozygous disruption of the beclin 1 autophagy gene. *J. Clin. Invest.* **112**, 1809–1820 (2003).
169. Takamura, A. *et al.* Autophagy-deficient mice develop multiple liver tumors. *Genes Dev.* **5**, 795–800 (2011).
170. Peiris-Pagès, M., Bonuccelli, G., Sotgia, F. & Lisanti, M. P. Mitochondrial fission as a driver of stemness in tumor cells : mDIV1 inhibits mitochondrial function , cell migration and cancer stem cell (CSC) signalling. *Oncotarget* **9**, 13254–13275 (2018).
171. Young, J., Yi, H., Kim, H. & Shong, M. Dysregulation of mitophagy in carcinogenesis and tumor progression. *BBA - Bioenerg.* **1858**, 633–640 (2017).
172. Senyilmaz, D. & Teleman, A. A. Chicken or the egg : Warburg effect and mitochondrial dysfunction. *F1000Prime Rep.* **13**, 1–13 (2015).
173. Liu, K. *et al.* Phosphorylated AKT inhibits the apoptosis induced by DRAM-mediated mitophagy in hepatocellular carcinoma by preventing the translocation of DRAM to mitochondria. *Cell Death Dis.* (2014). doi:10.1038/cddis.2014.51
174. Liu, K. *et al.* Mitophagy Controls the Activities of Tumor Suppressor p53 to Regulate Hepatic Cancer Stem Cells. *Mol. Biol. Cell* **68**, 281–292 (2017).
175. Bao, D. *et al.* Mitochondrial fission-induced mtDNA stress promotes tumor-associated macrophage infiltration and HCC progression. *Oncogene* (2019). doi:10.1038/s41388-019-0772-z
176. Krischer, J., Gilbert, A., Gorden, P. & Carpentier, J. Endocytosis is inhibited in hepatocytes from diabetic rats. *Diabetes* **42**, 1303–9 (1993).
177. Krahmer, N. *et al.* Organellar Proteomics and Phospho-Proteomics Reveal Subcellular Reorganization in Diet-Induced Hepatic Steatosis. *Dev. Cell* **47**, 205–221 (2018).

178. Chu, T., Sun, J., Saksena, S. & Emr, S. D. New component of ESCRT-I regulates endosomal sorting complex assembly. *J. Cell Biol.* **175**, 815–823 (2006).
179. Katzmann, D. J., Stefan, C. J., Babst, M. & Emr, S. D. Vps27 recruits ESCRT machinery to endosomes during MVB sorting. *J. Cell Biol.* **160**, 413–423 (2003).
180. Najafi, B. Novel functions of the ESCRTI protein VPS37a in liver metabolism. (2019).
181. Klötting, N. *et al.* Insulin-sensitive obesity. *Am. J. Physiol. Metab.* **1**, 506–515 (2018).
182. Bluher, M., Unger, R., Rassoul, F., Richter, V. & Paschke, R. Relation between glycaemic control, hyperinsulinaemia and plasma concentrations of soluble adhesion molecules in patients with impaired glucose tolerance or Type II diabetes. *Diabetologia* **45**, 210–216 (2002).
183. Apostolopoulou, M. *et al.* Specific Hepatic Sphingolipids Relate to Insulin Resistance, Oxidative Stress, and Inflammation in Nonalcoholic Steatohepatitis. *Diabetes Care* **41**, 1235–1243 (2018).
184. Rink, J., Ghigo, E., Kalaidzidis, Y., Zerial, M. & Médecine, F. De. Rab Conversion as a Mechanism of Progression from Early to Late Endosomes. *Cell* **122**, 735–749 (2005).
185. Wincott, F. *et al.* Synthesis, deprotection, analysis and purification of RNA and ribosomes. *Nucleic Acids Res.* **23**, 2677–2684 (1995).
186. Nishimura, T., Nakatake, Y., Konishi, M. & Itoh, N. Identification of a novel FGF, FGF-21, preferentially expressed in the liver. *Biochim Biophys Acta* **1492**, 203–206 (2000).
187. Hotta, Y. *et al.* Fibroblast growth factor 21 regulates lipolysis in white adipose tissue but is not required for ketogenesis and triglyceride clearance in liver. *Endocrinology* **150**, 4625–4633 (2009).
188. Raptis, D. A. *et al.* GPR120 on Kupffer cells mediates hepatoprotective effects of omega3-fatty acids. *J Hepatol* **60**, 625–632 (2014).
189. Brachs, S. *et al.* Inhibition of citrate cotransporter Slc13a5 / mINDY by RNAi improves hepatic insulin sensitivity and prevents diet-induced non-alcoholic fatty liver disease in mice. *Mol. Metab.* **5**, 1072–1082 (2016).

190. Kulak, N. A., Pichler, G., Paron, I., Nagaraj, N. & Mann, M. Minimal, encapsulated proteomic-sample processing applied to copy-number estimation in eukaryotic cells. *Nat. Methods* **11**, 319–324 (2014).
191. Vitale, G. *et al.* Distinct Rab-binding domains mediate the interaction of Rabaptin-5 with GTP-bound Rab4 and Rab5. *EMBO J* **17**, 1941–1951 (1998).
192. Feuchtinger, A. *et al.* Image analysis of immunohistochemistry is superior to visual scoring as shown for patient outcome of esophageal adenocarcinoma. *Histochem. Cell Biol.* **143**, 1–9 (2014).
193. Zellmer, S. *et al.* Transcription Factors ETF, E2F, and SP-1 Are Involved in Cytokine-Independent Proliferation of Murine Hepatocytes. *Hepatology* 2127–2136 (2010). doi:10.1002/hep.23930
194. Zeigerer, A. *et al.* Regulation of Liver Metabolism by the Endosomal GTPase Rab5. *Cell Rep.* **11**, 884–892 (2015).
195. Mollica, M. P. *et al.* Butyrate regulates liver mitochondrial function, efficiency, and dynamics in insulin-resistant obese mice. *Diabetes* **66**, 1405–1418 (2017).
196. French, A. P., Mills, S., Swarup, R., Bennett, M. J. & Pridmore, T. P. Colocalization of fluorescent markers in confocal microscope images of plant cells. *Nat. Protoc.* **3**, 619–628 (2008).
197. Kirshner, H., Aguet, F., Sage, D. & Unser, M. 3-D PSF fitting for fluorescence microscopy: implementation and localization application. *J Microsc* **249**, 13–25 (2013).
198. Sage, D. DeconvolutionLab2: An open-source software for deconvolution microscopy. *Methods* **115**, 28–41 (2017).

III. Tables and Figures

Figure 1: Global prevalence of diabetes.....	3
Figure 2: Progression of liver disease..	5
Figure 3: Liver morphology.....	6
Figure 4: Mitochondrial network in metabolic over- and undersupply.....	10
Figure 5: Localization and function of different Rabs	14
Figure 6: <i>SGIP1</i> and <i>CHMP4C</i> expression in patients with hepatic steatosis.....	22
Figure 7: <i>Rab3ip</i> was differentially regulated in <i>db/db</i> and HFD mice.....	24
Figure 8: Hepatic <i>RAB24</i> expression was upregulated in obese, NAFLD and NASH patients.....	26
Figure 9: RAB24 KD improved glucose clearance and insulin signaling in mice	28
Figure 10: RAB24 effect on insulin activation was abolished in FGF21 KO mice.....	30
Figure 11: RAB24 KD led to an increase in LDL uptake and a decrease in LDL secretion.....	33
Figure 12: Up-regulation of mitochondrial proteins was induced after liver specific KD of RAB24.....	35
Figure 13: Reduction of RAB24 caused an increase in mitochondrial mass as well as function.....	37
Figure 14: Depletion of RAB24 caused enhanced glycolysis..	39
Figure 15: RAB24 KD resulted in an increase in autophagy.....	41
Figure 16: RAB24 KD differed from ATG7 KD.....	43
Figure 17: RAB24 KD led to a reduction in mitophagy.....	45
Figure 18: RAB24 KD caused a better connected mitochondrial network.....	47
Figure 19: Depletion of RAB24 KD increased mitochondrial connectivity <i>in vivo</i>	48

Figure 20: Rab24 KD increased mitochondrial area and connectivity <i>in vitro</i> and in HFD mice.....	49
Figure 21: RAB24 KD lead to a decrease in DRP1-TOM20 co-localization..	52
Figure 22: RAB24 KD interacts with the fission machinery	53
Figure 23: FIS1 KD mimicked the RAB24 KD phenotype.....	55
Figure 24: Hepatic RAB24 KD improved serum lipid parameters and liver steatosis in HFD mice.....	58
Figure 25: Reduction of RAB24 in the livers of HFD mice improved glucose clearance.	60
Figure 26: RAB24 KD ameliorated a NASH mouse model.....	62
Figure 27: Localization of endosomal candidates in the cell.....	71
Table 1: Serum metabolic parameters....	31
Table 2: Primers for RT-PCR.....	99

IV. Abbreviations

°C	Degree Celsius
ADP	Adenosine diphosphate
AKT	Protein kinase B (PKB)
ALT	Alanine aminotransferase
APS	Ammonium persulfate
ATG7	Autophagy-related protein 7
ATP	Adenosine triphosphate
BMI	Body mass index
BSA	Bovine albumin serum
Ca ²⁺	Calcium
cAMP	Cyclic adenosine monophosphate
cDNA	Complementary DNA
CHMP4C	Charged Multivesicular Body Protein 4C
Cl	Chlorine
CO ₂	Carbon dioxide
DEP	Differentially expressed proteins
DIO	Diet-induced obesity
DMSO	Dimethyl sulfoxide
DNA	Desoxyribonuclein acid
dNTPs	Desoxynucleotides
DRP1	Dynamain-related protein 1
ECAR	Extracellular acidification rate
EDTA	Ethylenediaminetetraacetic acid
EM	Elektron microscopy
ER	Endoplasmatic reticulum
ESCRT III	Endosomal Sorting Complexes Required for Transport
FA	Fatty acids
FAD	Flavin adenine dinucleotide
FGF21	Fibroblast growth factor 21

FIS1	FISsion 1 protein
G6PASE	Glucose-6-phosphatase
GA	Glutaraldehyde
GAP	GTPase activating proteins
GDI	Guanosine nucleotide dissociation inhibitors
GEF	Guanine exchange factors
Glut	Glucose transporter
GMC	German Mouse Clinic
GSK3	Glycogen synthase kinase 3
GTT	Glucose tolerance tests
GWAS	Genome wide association study
H ₂ O	Water
HCC	Hepatocellular carcinoma
HDL	High density lipoprotein
HFD	High fat diet
HRP	Horseradish peroxidase
IF	Immunofluorescence analysis
INSR	Insulin receptor
K	Kalium
KD	Knock down
kDa	Kilo Dalton
kg	Killo gram
KO	Knock out
L	Litre
LDL	Low density lipoprotein
LFD	Low fat diet
LNP	Lipid nanoparticles
MID	Mitochondrial dynamics protein
MFF	Mitochondria fission factor
MFN	Mitofusin
mL	Milliliter

mM	Millimolar
Na	Sodium
NAD	Nicotinamide adenine dinucleotide
NAFLD	Non-alcoholic fatty liver disease
NASH	Non-alcoholic steatohepatitis
nM	Nanomolar
NRF	Nuclear respiratory factor
OCR	Oxidative phosphorylation rate
OPA1	Optic Atrophy 1
PBS	Phosphate buffered saline
PCK1	Phosphoenolpyruvate carboxykinase
PFA	Paraformaldehyde
PGC	Peroxisome proliferator-activated receptor γ coactivator
pH	Minus the decimal logarithm of the hydrogen ion activity in a solution
PI3K	Phosphatidylinositol 3-kinase
PINK1	PTEN-induced kinase 1
PKA	Protein kinase A
PLIN2	Perilipin 2
PM	Plasma membrane
Rab	Ras-related in brain
RAB3IP	Rab3a interacting protein
RNA	Ribonucleic acid
ROS	Reactive oxygen species
rpm	Rounds per minute
RT	Room temperature
RT-PCR	Quantitative real-time polymerase chain reaction
SDS	Sodium dodecyl Sulfate
SEM	Standard error of the mean
SGIP1	Src homology 3-domain growth factor receptor-bound 2-like (endophilin) interacting protein 1
siRNA	Small interfering RNA

SNPs	Single-nucleotide polymorphisms
SNARE	Soluble N-ethylmaleimide-sensitive-factor attachment receptor
TCA	Tricarboxylic acid cycle
Tris	2-amino-2-hydroxymethyl-propane-1,3-diol
TSC22D4	Transforming growth factor β -like stimulated clone (TSC) 22 D4
α	Alpha
β	Beta
μL	Microliter
μM	Micromolar

V. Acknowledgements

I thank Prof. Dr. Stephan Herzig and Dr. Anja Zeigerer for giving me the opportunity to work on this amazing project in this great institute; special thanks to Stephan for creating this inspiring environment and Anja for her great support and commitment. Further I want to thank Prof. Dr. Johannes Beckers for being on my thesis committee and Prof. Dr. Hans Hauner for supervising my defense. Special thanks to Prof. Dr. Ilona Grunwald Kadow and Prof. Dr. Matthias Blüher for examining my thesis and my defense.

Thanks to all of the IDC members for this vibrant environment, you made work feel like a place to meet friends. Especially Christina, my work twin who supported me through my whole thesis, scientifically and mentally! Thanks to Nirav, who became a close friend during my PhD and always had great scientific and life advice. Adam, Lea and Miri who always made time to listen to a friend. My Division Endocytosis and Metabolism, that always supported me, especially during the revision. Special thanks to Bahar and Basti that spend hours and hours with me in the DMF or doing tons of WB. Also Yun and Revathi, who stepped up during the revision to support me. Great thanks to the technicians, especially Quirin, Christoph, Andrea, Jeanette and Elena, without your help I couldn't have done it. I'm also thankful for my amazing family that supported me throughout my life. I'm also grateful to all the members of Munich MMA, you helped me keeping my sanity (whatever there was before) and my figure. Thanks to Dave for "emergency calls", Jens, Konnye, Sanny, Angela and the Wendy group for still being friends with me.

Und Ari, für alles.